

A COMPARISON OF NEUTRAL TO CHARGED CURRENT,
NEUTRINO-NUCLEON INTERACTIONS IN A WIDE BAND
NEUTRINO BEAM AT FERMILAB

By

John Allen Slate

A DISSERTATION

Submitted to
Michigan State University
in partial fulfillment of the requirements
for the degree of

DOCTOR OF PHILOSOPHY

Department of Physics and Astronomy

1985

ABSTRACT

A COMPARISON OF NEUTRAL TO CHARGED CURRENT,
NEUTRINO-NUCLEON INTERACTIONS IN A WIDE BAND
NEUTRINO BEAM AT FERMILAB

By

John Allen Slate

Results of measuring Neutral and Charged Current, neutrino-nucleon interactions, using a Wide Band neutrino beam at Fermilab are presented. The Neutral Current structure functions are measured (relative to the Charged Current structure functions) to determine if sufficient evidence exists for neutrally charged constituents within the nucleon, which are unobserved in Charged Current interactions. The structure function comparison does not utilize the usual Bjorken scaling variables, but rather, the quantity $E\theta^2$, calculated from measurement of the recoil hadronic system. Data indicate no difference between the Neutral and Charged Current structure functions. Based upon a corrected data sample of 2850 Neutral and 8832 Charged Current events, we measure an integrated ratio; $R_\nu = 0.323 \pm 0.007$ (stat.) ± 0.025 (sys.), which is consistent with a value of $\sin^2\theta_w = 0.217 \pm 0.032$ (stat.) ± 0.021 (sys.).

A COMPARISON OF NEUTRAL TO CHARGED CURRENT,
NEUTRINO-NUCLEON INTERACTIONS IN A WIDE BAND
NEUTRINO BEAM AT FERMILAB

By

John Allen Slate

A DISSERTATION

Submitted to
Michigan State University
in partial fulfillment of the requirements
for the degree of

DOCTOR OF PHILOSOPHY

Department of Physics and Astronomy

1985

to the Lord God,
who makes all things
possible.

ACKNOWLEDGMENTS

First and foremost, I wish to thank my thesis advisor, Maris Abolins, for his guidance, advice, instruction and encouragement for the duration of this work. I have learned much about being a good experimentalist through his example and teaching, and will carry his influence throughout the rest of my endeavors.

Two individuals, Raymond Brock and Jorge Morfin, have taken special interest in my work. They encouraged me to investigate physics topics not entirely related to this work and provided me with literature, ideas and many interesting discussions. My thanks to them both.

I thank the members of the E594 collaboration. Each of you has had a direct, positive influence upon me and upon my understanding of Physics. I especially want to thank my fellow graduate students: Andy Cohen, Mike Tartaglia, Juan Bofill, Tom Mattison, Gong Ping Yeh, Terry Eldridge, Aseet Mukherjee, and Rich Magahiz. We shared common interests, insights, knowledge and income levels. Thanks go to Ron Olsen, Super-Technician, a man who knows everything and can fix anything, and to the summer students, Sue, Carrie, Anna, and Joe, who will always be honorary "594'ers".

I wish to thank the Fermilab Neutrino Department Staff for their expertise and assistance, the Neutrino Beam Line Technicians, who answered our frantic calls anytime day or night, and the Accelerator Staff, who kept the protons flying in their predetermined paths.

Thanks are in order for Pam, Cheryl and Linda of the Fermilab Housing Office, and to Phyllis, Sherry and Joy of the Fermilab Users' Office, for providing a human side to Fermilab. Special thanks to Phyllis Hale, for her role as surrogate mother to me and many other lonely graduate students.

To the MSU High Energy Group, its faculty, staff and students, I offer my thanks for providing a fun atmosphere for learning and work. Special thanks to Steve Cooper, Lisa Dillingham, and Ron Richards for friendship above and beyond the call of duty.

I thank my father, Alfred, whose interest in Astronomy sparked and sustained my own interests in science, my mother, Clara, for selfless love and encouragement, and my brother, Jim, a man of excellence in his own right, for enhancing my understanding of the world of fine art.

I thank my two "extended" families at Blanchard Road Alliance Church, in Wheaton and at East Lansing Trinity Church here in East Lansing.

Special thanks to Mark Johnson and Dave Rinard, for life-long friendship.

I thank the National Science Foundation for its support of my education.

To all my family, friends and educators: Yes, I know my name is on the title page, but you have all had a share in it.

TABLE OF CONTENTS

List of Tablespage	ix
List of Figures.		x
Chapter 1. Introduction		1
1.1. Weak Interactions		1
1.2. Kinematics.		2
1.3. Neutrino Beams and Detectors.		5
1.4. Review of Experiments		7
1.4.1. Gargamelle.		7
1.4.2. HPWF/HPWFRO		7
1.4.3. CITF/CITFR/CFRR/CCFRR		8
1.4.4. CRS-BNL/CR-BNL.		9
1.4.5. CDHS.		9
1.4.6. CHARM		10
1.5. The E594-FMMN Experiment.		11
Chapter 2. Neutrino-Nucleon Interactions.		13
2.1. The Parton Model.		13
2.1.1. Assumptions		13
2.1.2. Lepton-Parton and Lepton-Nucleon Scattering		15
2.2. Charged Current Neutrino-Nucleon Scattering		17
2.2.1. Structure Functions		17
2.2.2. The Parton Model, Quarks, and Structure Functions		21
2.3. The Standard Model.		26

2.3.1.	The Weinberg-Salam Model for Leptons.	page 26
2.3.2.	Weinberg-Salam Extension to Hadrons	29
2.4.	Neutral Current Neutrino-Nucleon Scattering	31
Chapter 3.	The E594 Detector.	33
3.1.	General Overview.	33
3.2.	The Flash Chambers.	36
3.2.1.	Construction.	36
3.2.2.	Performance	41
3.3.	The Gas Cart.	48
3.3.1.	Gas Flow.	48
3.3.2.	Gas Purification.	49
3.3.3.	Gas Monitoring.	51
3.4.	The High Voltage System.	52
3.4.1.	Overview.	52
3.4.2.	The High Voltage Regulator.	55
3.4.3.	High Voltage Pulse Monitoring System.	58
3.5.	Proportional Tube Planes.	61
3.5.1.	Construction.	61
3.5.2.	Trigger Electronics	61
3.5.3.	Trigger Logic	63
3.6.	Toroids	64
3.7.	Online Computer	65
Chapter 4.	Surveying and Alignment.	66
4.1.	Overview.	66
4.2.	Surveying	66
4.3.	Alignment	68
Chapter 5.	Calibration.	73

5.1.	Beam Line	page 73
5.2.	The Trigger	73
5.3.	Angle Resolutions	75
5.4.	Energy Resolutions	76
Chapter 6.	The Experiment	85
6.1.	Beam Line	85
6.2.	Monitoring.	87
6.3.	WBB Flux.	91
6.3.1.	Monte Carlo Simulation.	91
6.3.2.	Comparison With Data.	92
6.4.	Event Triggers.	95
6.5.	Gating.	98
Chapter 7.	Data Analysis.	103
7.1.	Purpose	103
7.2.	Data Analysis Software.	104
7.3.	Data Cuts	113
7.4.	NC/CC Ratio	114
7.4.1.	Monte Carlo	118
7.4.2.	Antineutrino Distributions.	120
7.4.3.	Correction of Data.	126
7.5.	Determination of NC Structure Function Parameters	130
7.5.1.	Parameterization.	130
7.5.2.	Analysis Approach	131
7.5.3.	Systematic Error Approximation.	132
7.5.4.	Results	141
7.6.	Comparison With Other Experiments	141
Chapter 8.	Conclusions.	146

Appendix A. The E594 Monte Carlo Program.	page 149
A.1. Electromagnetic Showers	149
A.2. Hadronic Showers.	150
A.3. Non-Catastrophic Processes.	152
A.4. Flash Chamber Data.	152
A.5. Proportional Tube Data.	153
A.6. Comparison With Calibration Data.	153
Appendix B. Derivation of E_0^2	166
List of References	170

LIST OF TABLES

Table 2.1.	Quark Quantum Numbers.	page	24
Table 5.1.	Hit Cell Enhancement for 10 Cell Regions		81
Table 6.1.	Run Type Triggers and Gate Scheme.		101
Table 6.2.	Total Triggers by Trigger Type.		102
Table 7.1.	Variation of $\Delta\beta$ to β_{cc}		139
Table 7.2.	Fitted Values of β_{nc} for Simulated Data.		140
Table 7.3.	Results of Two-Parameter Fits.		142
Table 7.4.	Summary of NBB Analysis.		143
Table 7.5.	Summary of CHARM Analysis.		145
Table A.1.	Angular Profile Comparison		165
Table B.1.	Magnitude of $(W/E_h)^2$		169

LIST OF FIGURES

Figure 1.1. Deep Inelastic Neutrino-Nucleon Scattering.	3
Figure 2.1. Parton Scattering (Breit Frame)	14
Figure 2.2. Lepton-Parton Scattering.	16
Figure 2.3. Neutrino-Nucleon Scattering (CC and NC Case).	18
Figure 3.1. The E594 Detector	34
Figure 3.2. Construction of Flash Chamber Readout	39
Figure 3.3. Voltage Output from Magnetostrictive Amplifier.	40
Figure 3.4. Flash Chamber Efficiency and Hit Cell Multiplicity.	43
Figure 3.5. Efficiency Stability During WBB Run	45
Figure 3.6. Efficiency and Delay Measurements - June 1981	47
Figure 3.7. Schematic of Gas Recirculator	50
Figure 3.8. PFN Circuit and High Voltage Pulse.	53
Figure 3.9. Schematic of High Voltage System.	54
Figure 3.10. Schematic of Regulator Circuit.	56
Figure 3.11. High Voltage Pulse Monitoring system (PQD).	59
Figure 4.1. Flash Chamber Coordinate System	67
Figure 4.2. Single View Deviations (in clock counts).	70
Figure 4.3. Three View Deviations (in clock counts)	71
Figure 5.1. Calibration Beam Line	74
Figure 5.2. Muon Angle Resolution	77
Figure 5.3. Electron Angle Resolution	78
Figure 5.4. Hadron Angle Resolution	79

Figure 5.5.	Electron Energy Calibration and Resolution.	page 82
Figure 5.6.	Hadron Energy Calibration	83
Figure 5.7.	Hadron Energy Resolution.	84
Figure 6.1.	NØ Wide Band Beam Line.	86
Figure 6.2.	POT Distribution for HORN ON/OFF.	89
Figure 6.3.	Muon Counter Distribution for HORN ON/OFF	90
Figure 6.4.	Energy Spectrum from Quasi Elastic Data	93
Figure 6.5.	Energy Spectra from Charged Current Data.	94
Figure 6.6.	Schematic of WBB Gating	99
Figure 7.1.	Data Analysis Flow Diagram.	105
Figure 7.2.	Typical CC Event.	107
Figure 7.3.	Typical NC Event.	108
Figure 7.4.	Blow-up of CC Event	109
Figure 7.5.	NC/CC Ratio - Data.	115
Figure 7.6.	Contours of Constant $E\theta^2$	117
Figure 7.7.	NC/CC Ratio - Data and Monte Carlo.	121
Figure 7.8.	CC Misclassification as Function of $E\theta^2$	122
Figure 7.9.	$\overline{\text{CC}}$ Misclassification as Function of $E\theta^2$	123
Figure 7.10.	$f_{\text{cc}}(E\theta^2)$	124
Figure 7.11.	$f_{\text{nc}}(E\theta^2)$	125
Figure 7.12.	Corrected NC/CC Ratio - Data.	127
Figure 7.13.	Corrected NC/CC Ratio - Monte Carlo	128
Figure 7.14.	Stability of β_{nc} to $E\theta^2$ Range	133
Figure 7.15.	Effect upon β_{nc} to Variations in α and β	134
Figure 7.16.	Effect upon β_{nc} to Variations in $\bar{\alpha}$ and γ	135
Figure 7.17.	Effect of Hadronic Energy Resolution and Offset	137
Figure 7.18.	Effect of Hadronic Angle Resolution	138

Figure A.1.	Energy Comparison - 10 GeV.	page 154
Figure A.2.	Energy Comparison - 35 GeV.	155
Figure A.3.	Energy Comparison - 100 GeV	156
Figure A.4.	Monte Carlo Energy Difference	157
Figure A.5.	Density Comparison - 10 GeV	159
Figure A.6.	Density Comparison - 35 GeV	160
Figure A.7.	Density Comparison - 100 GeV.	161
Figure A.8.	Shower Length Comparison - 10 GeV	162
Figure A.9.	Shower Length Comparison - 35 GeV	163
Figure A.10.	Shower Length Comparison - 100 GeV.	164

CHAPTER 1. INTRODUCTION

1.1. WEAK INTERACTIONS

Weak interactions were first studied via nuclear β -decay experiments. The β -particle was known to be an electron. What puzzled experimenters of the 1920's was that the electron's spectrum was continuous rather than discrete. In 1930 Pauli suggested that there was a very light, uncharged, penetrating particle call a neutrino which shared the decay energy with the emitted electron. The existence of this electron-type neutrino (actually antineutrino) was confirmed by Reines and Cowan¹ in 1959 using the antineutrino flux from a nuclear reactor.

Fermi took Pauli's idea and began the first steps towards placing the Weak interaction on a firm theoretical basis. Fermi² described the interaction in terms of a four-fermion point interaction, whose strength was given by a single constant. It is also possible to describe the Weak interaction as the interaction between two currents, mediated by a weak-interaction quantum. Since the Weak interaction in the β -decay interactions changes charge, the quantum must be charged (W^\pm). Thus the β -decay interactions are described as a Charged Current (CC) interaction.

Experimentally, during the late 1950's it was discovered that the Weak interaction does not conserve parity,³ the neutrino's helicity was measured,⁴ and the space-time nature of the Weak interaction was

determined.⁵ The experiment which determined the space-time structure did so by analyzing the decay branching ratios of pions and muons. Muons, which are like electrons only more massive, were found to have an associated neutrino.⁶

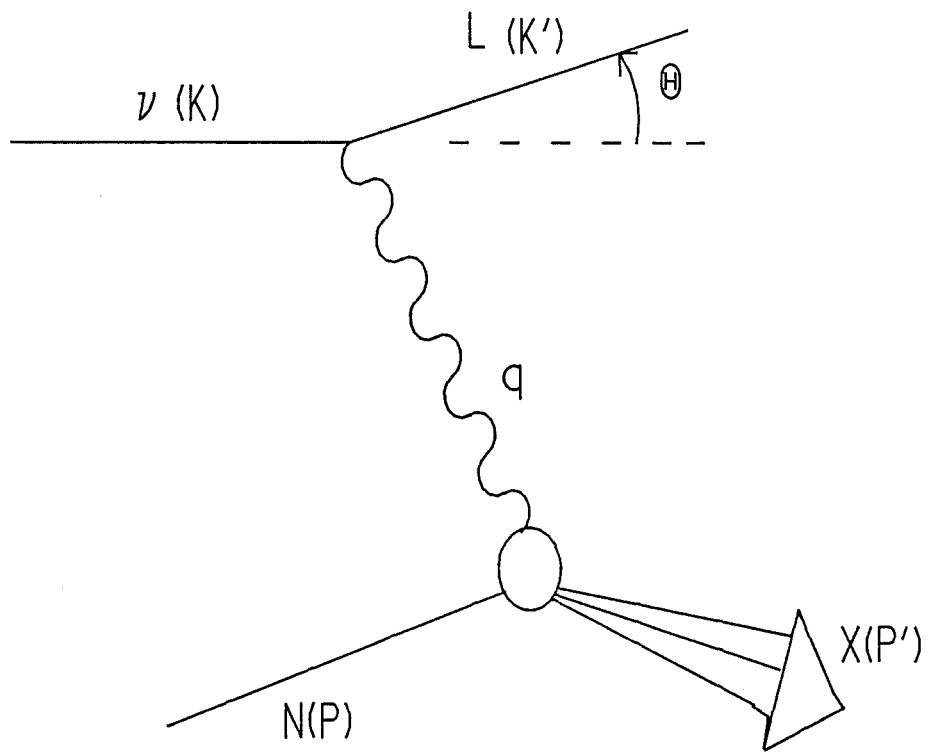
With the advent of large accelerators in the 1960's and 70's, it was possible to perform experiments utilizing intense beams of muon-type neutrinos (and antineutrinos). One of the biggest surprises was the discovery of weak-neutral current (NC) interactions in a bubble chamber in Europe.⁷ Since then, over the last ten years, many experiments have probed the nature of the Weak interaction in neutrino-nucleon and neutrino-electron interactions.

Theoretically, the original description by Fermi was shown to cause problems beyond the leading order in perturbation theory. In 1967, Weinberg⁸ and Salam⁹ proposed a model for the Electro-Weak interactions of leptons. This so called "Standard" Model was extended to hadrons (quarks).¹⁰ The data are consistent with a single value for the only parameter of the model, $\sin^2\theta_W = 0.23 \pm 0.01$.¹¹

The Standard Model has had many successes, including the prediction of the existence of neutral-current interactions. Recent discoveries of the W^\pm and Z^0 bosons^{12,13} add credence to the Standard Model. Despite its successes, some of the basic assumptions remain untested or poorly constrained. The limits of the Standard Model are being tested in some of the current European experiments.¹⁴

1.2. KINEMATICS

A schematic of deep inelastic neutrino-nucleon scattering is shown in Figure 1.1. K and P are the four-vectors (E, \vec{P}) of the incoming



DEEP INELASTIC NEUTRINO SCATTERING

Figure 1.1. Deep Inelastic Neutrino-Nucleon Scattering

lepton and target nucleon. K' and P' are the four-vectors of the outgoing lepton and hadronic system X . The momentum transfer via the intermediate boson is q (ν, \vec{q}). The interaction can be defined in terms of Lorentz-invariant variables:

$$Q^2 = -q^2 = -(K - K')^2 = -(P' - P)^2$$

$$\nu = \frac{P \cdot q}{M}$$

$$W^2 = (P')^2 = (P + q)^2.$$

In the laboratory frame, neglecting lepton masses, we can write the variables as:

$$Q^2 = 2E_\ell E_{\ell'} (1 - \cos \theta_{\ell\ell'})$$

$$\nu = E_\ell - E_{\ell'} = E_X - M$$

$$W^2 = M^2 + 2M\nu - Q^2$$

where M is the nucleon mass. Alternatively, one can use the dimensionless Bjorken scaling variables x and y , defined as:

$$x = \frac{Q^2}{2M\nu}, \quad 0 \leq x \leq 1$$

$$y = \frac{M\nu}{K \cdot P}, \quad 0 \leq y \leq 1.$$

In the laboratory frame, $y = (E_\ell - E_{\ell'})/E_\ell \approx E_X/E_\ell$ and is the fraction of the incident lepton energy transferred to the hadronic system.

The scaling variables are useful, and in particular, it is common to write the cross section in terms of x and y . For (anti)neutrino-nucleon scattering:

$$\frac{d\sigma(\nu, \bar{\nu})}{dx dy} = \frac{G^2 M E}{\pi} \left[\left(1 - y + \frac{1}{2} y^2\right) F_2(\nu, \bar{\nu})(x) \pm \left(1 - \frac{1}{2} y\right) y x F_3(\nu, \bar{\nu})(x) \right].$$

F_2 and $x F_3$ are known as the weak-nucleon structure functions and (to first order) are functions only of the scaling variable x . (At higher orders, they depend upon both x and Q^2 .) These structure functions are a result of the nucleon being an extended system of quarks, exhibiting

complex structure to the Weak interactions. In general, the structure functions will differ for Charged and Neutral Current interactions.

1.3. NEUTRINO BEAMS AND DETECTORS

In order to perform an experiment using neutrinos, it is necessary to have both an intense beam of high energy neutrinos and a detector. Since neutrino cross sections are very small, ($\approx 10^{-38}$ cm² at a neutrino energy of 1 GeV) the neutrino beam must have a high intensity in order that the interaction rate in the detector be reasonable. Ideally, a good detector should be able to measure the energy and angle of all particles in an interaction. Also, because of the small cross section, neutrino detectors must be massive, usually anywhere from a few tons to several hundred tons.

High energy neutrino beams are made using a standard technique. A proton beam from a large accelerator is extracted and is directed toward a target. The target material is usually a low atomic number metal such as Aluminum or Beryllium. Secondary particles, mostly pions and kaons, are formed from interactions between the protons and the target. The secondaries travel through an evacuated region, allowing time for decay, with decays dominated by two-particle decays of a muon and a muon-type neutrino. Following the decay region is a large amount of absorber material to filter out all other particles except the neutrinos. Most high energy neutrino experiments are done at one of two laboratories: the Fermi National Accelerator Laboratory (FNAL, Fermilab) in Batavia, Illinois, and the European Organization for Nuclear Research (CERN) in Geneva, Switzerland.

There are two main types of neutrino beams, Wide Band (WBB) and Narrow Band (NBB). In a Wide Band Beam, the secondary mesons are sign selected before the decay region. The sign selection is done by using a magnet element. Mesons of a given sign are focused and collimated toward the decay region, opposite sign mesons are defocused. Upon decay, the neutrinos are predominately muon-type neutrinos (or muon-antineutrinos). This provides an intense beam of neutrinos over a wide spectrum of energies. If the secondary mesons are both sign and momentum selected, then a Narrow Band Beam is the result. Neutrino intensity is decreased, but since the neutrinos come from the two-body decay of a parent of known momentum, the incident neutrino's energy is approximately known. The neutrino spectra vary, in a calculable manner, as a function of the transverse distance from the beam axis. Both FNAL and CERN can produce either Wide or Narrow Band Beams.

Neutrino detectors can be classified into two main types: bubble chambers and electronic calorimeters. There are other detector types, such as photographic emulsions, large tanks filled with cleaning fluid, etc. Bubble chambers, filled with a heavy, cold liquid, offer good particle identification and small background, but because of their low mass ($\approx 3-5$ tons) suffer from low event rates. Electronic calorimeters offer excellent event rates due to their high fiducial mass ($\approx 100-300$ tons, and up to 1000 tons) but have decreased particle resolution and minimal particle identification. In general, most electronic calorimeters are designed to offer a compromise between pattern recognition capability and measurement resolution in return for target mass.

1.4. REVIEW OF EXPERIMENTS

This section will serve to give a brief overview of neutrino-nucleon experiments which have taken place over the last decade. This will not be a comprehensive review (there have been roughly 20 experiments in the last 10 years) but will focus upon the experiments which have contributed significantly to the measurement of Neutral Current interactions and to the measurement of Charged and Neutral Current structure functions.

1.4.1. GARGAMELLE. In the beginning, there was Gargamelle. This was a bubble chamber, cylindrical in shape, filled with either Freon (CF_3Br) or a propane-Freon mixture. The chamber was 4.5 meters long, with a diameter of 1.85 meters.

In 1973, a collaboration discovered the existence of neutrino-nucleon neutral current events¹⁵ and neutrino-electron elastic scattering.¹⁶ The experiment used a WBB at the CERN Proton Synchrotron (PS) for both neutrinos and antineutrinos, with neutrino energies in the range of 0.5 to 15 GeV. The experiment measured the total cross sections for both ν and $\bar{\nu}$ CC interactions,¹⁷ thus establishing the linear dependence of the cross section upon the incident energy. The NC to CC ratio was determined,¹⁵ placing limits upon the value of $\sin^2\theta_w$.

1.4.2. HPWF/HPWFRO. A collaboration of Harvard, Pennsylvania, Wisconsin and Fermilab first detected neutrino-nucleon Neutral Current events¹⁸ in a large, electronic calorimeter. The detector consisted of a target-detector calorimeter followed by a muon spectrometer. The calorimeter used liquid scintillation counters for the target material and calorimetry, and wide gap spark chambers for muon tracking. The muon spectrometer consisted of 4-12' diameter Iron toroid magnets,

interspersed with spark chambers. The experiment used several types of WB Beams at FNAL. The total cross section¹⁹ (for CC), x and y distributions for CC interactions²⁰ and NC/CC ratios¹⁸ were measured for both neutrino and antineutrino beams with energies up to 160 GeV. The experiment also detected opposite sign di-muon events,²¹ which provided the first evidence of charm production and decay via neutrinos, same sign di-muon events,²¹ and tri-muon events.²²

In 1977, the detector was upgraded to include an Iron target, liquid scintillator and an Iron calorimeter. The muon spectrometer was also upgraded to include 3-24' diameter toroids. Rutgers and Ohio State joined the collaboration (HPWFRO). This group measured the x and y distributions, $F_2(x)$, $xF_3(x)$, and quark fractions within the nucleon, using the CC events.²³ Di-muon events were also measured.²⁴

1.4.3. CITF/CITFR/CFRR/CCFRR. The CIT-Fermilab and the CIT-Fermilab-Rockefeller groups used a new NBB at Fermilab. Various momenta of the secondary mesons were used for both neutrino and antineutrino beams. This group used a detector consisting of a Iron calorimeter and a muon spectrometer. The calorimeter consisted of 140 tons of steel plates (3 m by 3 m cross section) with spark chambers every 20 cm and scintillation counters every 10 cm. The experiment measured total cross sections for the CC interaction,²⁵ NC/CC ratios²⁶ (as well as $\sin^2\theta_w$), and integrated values of the CC structure functions,²⁵ for neutrino energies from 45 to 205 GeV. The space-time structure²⁷ of the Weak interaction was determined.

The calorimeter size was increased to 690 tons, with a 420 ton spectrometer. Rochester joined the collaboration (CFRR). Continuing to use a NBB for both ν and $\bar{\nu}$, the experiment measured total cross

sections,^{28,29} y distributions²⁸ for CC events as well as NC cross sections²⁹ to determine $\sin^2\theta_w$. The x and Q^2 dependence of F_2 and xF_3 were measured for CC events.³⁰ With the inclusion of Columbia (CCFRR) the group measured total CC cross sections and searched for evidence of neutrino oscillations.³¹

1.4.4. CRS-BNL/CR-BNL. Two bubble chamber experiments are worthy of mention for measuring the x distributions of neutrino NC interactions. The Columbia-Rutgers-Stevens-BNL group measured x and y distributions for ν NC and ν CC interactions using a NBB at Brookhaven National Laboratory (BNL).³² Neutrino energy ranged from 3-9 GeV. The seven foot bubble chamber was filled with a Ne-H₂ mixture, providing a fiducial mass of 3 tons. This group measured x and y distributions, as well as the quantity $\langle xy \rangle$ for both NC and CC interactions. They determined (with 23 NC and 73 CC events) that the the NC y distribution was consistent with the space-time nature of the CC interaction, as well as concluding that $\langle xy \rangle_{nc} \approx \langle xy \rangle_{cc}$.

The Columbia-Rutgers-BNL group used the 15' FNAL bubble chamber, in a NB neutrino beam.³³ This group measured x and y distributions for both ν NC and ν CC interactions, measured NC/CC ratios and NC structure functions. The collaboration obtained 151 NC and 683 CC events.

1.4.5. CDHS. The CERN-Dortmund-Heidelberg-Saclay collaboration probably is the preeminent neutrino experiment to date. Primarily using the NBB at the CERN Super Proton Synchrotron (SPS), the group has also taken data using the CERN WBB. With an event sample of 35,700 ν (8074 NC and 27603 CC) interactions and 8600 $\bar{\nu}$ (2203 NC and 6367 CC) interactions, CDHS has made precise measurements of many of the quantities already discussed.

The detector consists of a magnetized Iron calorimeter. The detector is constructed out of 3.75 meter diameter Iron plates, each plate either 5 cm or 15 cm thick. Between each plate are scintillator planes. The plates are grouped into modules, with each module weighing about 65 tons, for a total weight of 1235 tons. Triple plane drift chambers are sandwiched between modules, with wires at 0° , $\pm 60^\circ$ to the horizontal.

Given the νCC and $\bar{\nu}\text{CC}$ data, with neutrino energy from 30 to 200 GeV, CDHS has measured the total cross section, x and y distributions, F_2 and xF_3 as functions of x and Q^2 , as well as individual quark distributions and momentum fractions.³⁴ When neutrino and antineutrino NC events are included, the group can measure NC/CC ratios, $\sin^2\theta_w$, the space-time nature of the NC, as well as a comparison of Charged and Neutral Current hadronic energy distributions.³⁵ The group has also measured opposite and like sign di-muon events.³⁶

1.4.6. CHARM. The detector of the Amsterdam-CERN-Hamburg-Moscow-Rome collaboration sits just downstream of the CDHS detector. The two detectors were used together to measure the polarization of the muon.³⁷ The detector consists of a "sandwich" of scintillator plane-marble (CaCO_2) target-proportional wire drift-chamber. There are 78 "sandwiches" in the detector for a total of 180 tons with a 3 m by 3 m cross section. Surrounding the marble is a "window frame" of magnetized Iron and scintillator. CHARM took ν and $\bar{\nu}$ data in both Narrow and Wide Band Beams. With NBB neutrino energies in the range of 30 to 200 GeV, they obtained 8553 ν (6271 CC and 2282 NC events) and 3578 $\bar{\nu}$ (2536 CC and 1042 NC events) interactions. They measured total CC cross sections, NC/CC ratios, $\sin^2\theta_w$, CC structure functions, antiquark

distributions, gluon distributions and x and y distributions for CC interactions.³⁸ Most importantly, they measured the NC x distributions and fitted the NC structure functions to a parameterized functional form.³⁹ With larger numbers of NC events, they can achieve a better measurement than either the CRS-BNL or CR-BNL groups.

1.5. THE E594-FMMN EXPERIMENT

A collaboration of Fermilab, MIT, MSU, and Northern Illinois built a large, fine-grained calorimeter and muon spectrometer in the LAB C building at FNAL. The collaboration took data using a WBB (first half of 1981) and a NBB (first half of 1982) for both neutrinos and antineutrinos.

The detector calorimeter consists of acrylic sheets filled with either steel shot or sand as target material, plastic flash chambers, sandwiched between the target planes, and proportional wire chambers every 16 target planes. The muon spectrometer consists of 3-24' diameter and 4-12' diameter magnetic toroids (inherited from the HPWFRO group). Proportional chambers were inserted in two of the four 12' toroid gaps for the WBB. During the WBB running, the calorimeter had a fiducial mass of 240 tons with a 3 m by 3 m cross section. For the NBB, the detector length was increased by 50% (≈ 100 tons), and the muon spectrometer was upgraded.

Significant physics from the WBB consists of neutrino-electron elastic scattering, deep-inelastic NC and CC interactions and analysis of the quasi-elastic interaction: $\nu(\bar{\nu}) + N \rightarrow \mu^-(\mu^+) + N'$. The NBB analysis will include: x and y distributions and structure function measurement for both NC and CC interactions, total cross section

measurement, measurement of $\sin^2\theta_w$, analysis of neutrino-electron scattering and a search for neutrino oscillations.

The scope of this thesis is to present the NC and CC analysis, from data taken in the WBB, and in particular, to determine the NC structure functions relative to the CC structure functions given an explicit parameterization for the CC functions. A Wide Band neutrino beam is not ideal for this analysis. Since the incident neutrino energy is unknown, it is not possible to explicitly determine either x or y for Neutral Current interactions. We will show, however, that it is possible to calculate a quantity, say u , which is a function of both x and y . Using both NC and CC distributions of the quantity " u ", and given certain assumptions about the CC structure functions, it will be possible to make certain statements about the NC structure functions. Given the higher event rate (factor of 10) of the WBB over the NBB, a larger data sample should compensate, in part, for the inability to directly compare x distributions.

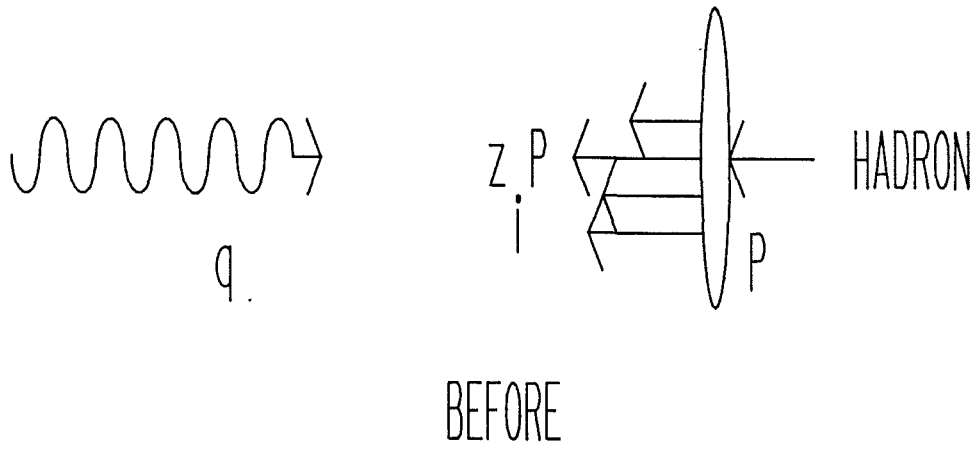
The theoretical background for neutrino-nucleon interactions is discussed in Chapter 2. Chapters 3-5 will discuss the E594 detector: its construction, operation, alignment and calibration. Information concerning the neutrino beam, as well as experimental gating and triggering is presented in Chapter 6. Data analysis and conclusions will be found in Chapters 7 and 8.

CHAPTER 2. NEUTRINO-NUCLEON INTERACTIONS

2.1. THE PARTON MODEL

The parton model was developed as a result of ep scattering experiments at SLAC in 1968.⁴⁰ The data showed electrons scattering from protons at large energy and momentum transfers with significant probability. The data suggested that the proton's charge was localized on a few, small scattering centers. Energy and angle distributions of the scattered electrons suggested that the scattering centers were structureless, spin-one-half Dirac particles. Because the scattering centers (partons) seemed to be structureless, the energy and angle correlations exhibit "scaling" as described by Bjorken,⁴¹ Feynman,⁴² and Bjorken and Paschos.⁴³ Scaling refers to an interaction which is independent of any mass or energy scale.

2.1.1. Assumptions. Scaling suggests that the current-target interaction is governed by incoherent (free) scattering. The Parton Model contains implicit assumptions which must be satisfied for the incoherent impulse approximation to be valid: (1) the current-parton interaction time is small, so that interactions between partons can be neglected and (2) final state interactions can be ignored. Intuitively, the parton is struck so violently that it is removed from the nucleon, independent of the other partons. Figure 2.1 shows a diagram which illustrates the scattering. In the Breit frame, before interactions, partons have essentially all longitudinal momenta, each parton carrying



AFTER

Figure 2.1. Parton Scattering (Breit Frame)

some fraction z_i of the parent's momentum. After interaction, the current momentum has removed one of the partons kinematically from the target with the non-interacting partons continuing on undisturbed. Kinematically, the Parton Model is satisfied if interaction energies (e.g. $2Mv$, Q^2 , W^2) are very much greater than the square of the parton state's effective mass, M_{eff}^2 .

2.1.2. Lepton-Parton and Lepton-Nucleon Scattering. In order to make the connection between lepton-parton and lepton-nucleon scattering, it is necessary to calculate the diagram(s), illustrated by Figure 2.2, for an N parton configuration, summing incoherently over all N partons, and summing incoherently over all final state hadrons which result from the non-interacting partons. The four-momenta of the states shown in Figure 2.2 are as follows:

$$p^\mu = (P + \frac{M^2}{2P}, 0, P) \quad p_{\rightarrow\infty}^\mu = (P, 0, P) \quad (2a)$$

$$p_i^\mu = (z_i P + \frac{p_{iT}^2 + \mu_i^2}{2z_i P}, p_{iT}, z_i P) \quad p_{\rightarrow\infty}^\mu = (z_i P, 0, z_i P) = z_i P \quad (2b)$$

$$p_i'^\mu = p_i^\mu \quad (2c)$$

$$p_i'^\mu = (\sqrt{(\vec{p}_i + \vec{q})^2 + \mu_i^2}, p_{iT} + q_T, z_i P + q_L) \quad (2d)$$

where $\sum_i z_i = 1$, and μ_i is the mass of the i^{th} parton.

Let

$$f_i^N(z) dz \quad (3)$$

represent the probability distribution that parton i out of N has longitudinal momentum fraction z between z and z+dz. Since the parton must have some momentum, then

$$\int_0^1 f_i^N(z) dz = 1, \quad (4)$$

and let P_N be the probability of finding N partons within the nucleon

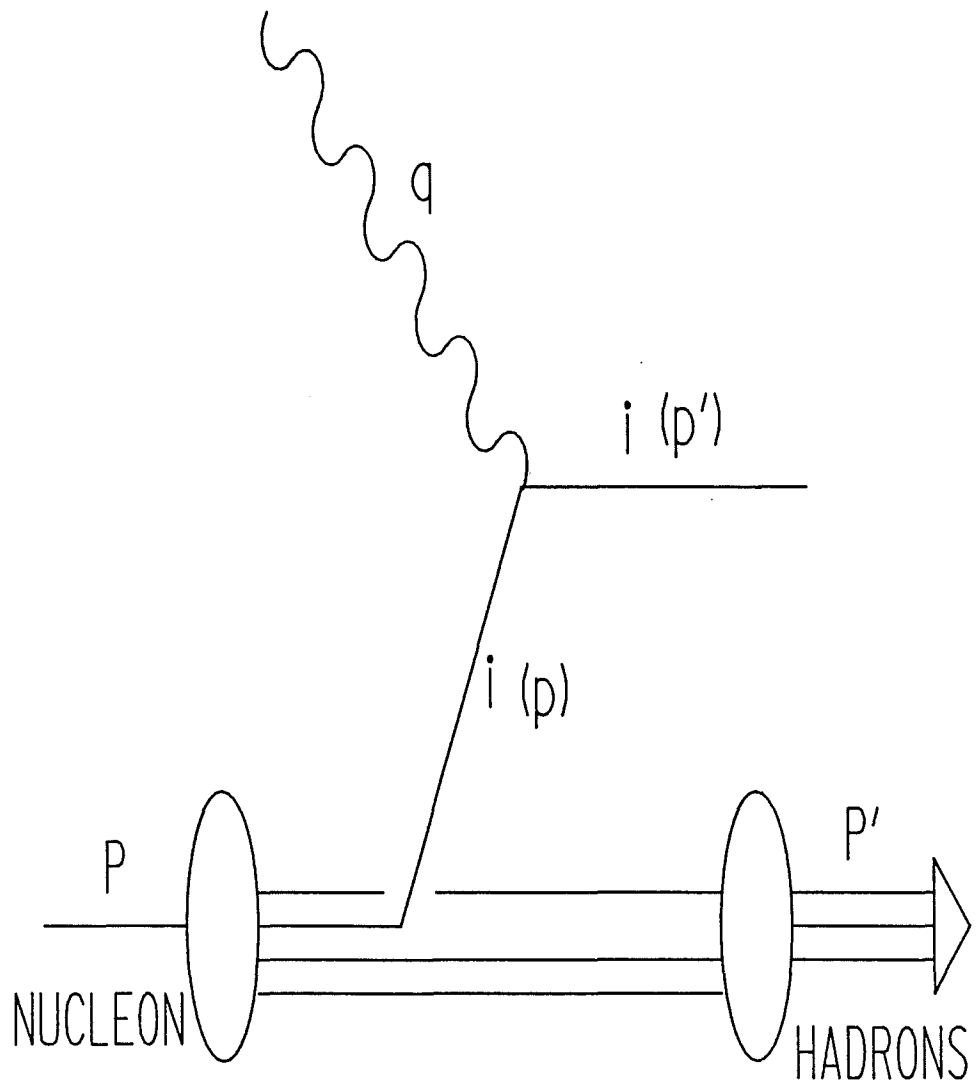


Figure 2.2. Lepton - Parton Scattering

with

$$\sum_N P_N = 1. \quad (5)$$

The hadronic tensor for the interaction becomes:

$$W_{\mu\nu}(P, q) = \sum_N P_N \sum_{i=1}^N \int f_i^N(z_i) dz W_{\mu\nu}(p_i, q) \quad (6)$$

where $W_{\mu\nu}(p_i, q)$ is the interaction tensor for the i^{th} parton.

Equation 6 can be written in expanded form:

$$W_{\mu\nu}(P, q) = \frac{1}{2\pi} \cdot \frac{1}{2M} \sum_{\text{spins}} \sum_{p_i} \int \frac{d^3 p'}{(2\pi)^3 2p'_0} \sum_N P_N \sum_{i=1}^N \int dz f_i^N(z) \quad (7)$$

$$* \langle p_i | J_\mu(0) | p'_i \rangle \langle p'_i | J_\nu(0) | p_i \rangle \left(\frac{P'_0}{p'_i} \right) (2\pi)^4 \delta^4(p_i + q - p'_i)$$

by following standard procedures given in texts.⁴⁴ Note that Equation 7 contains no cross terms, implying incoherent scattering.

In order to proceed further, it is necessary to define the matrix element:

$$\langle p'_i | J_\nu(0) | p_i \rangle. \quad (8)$$

We will come back to this point later within the context of neutrino-nucleon scattering.

2.2. CHARGED CURRENT NEUTRINO-NUCLEON SCATTERING

2.2.1. Structure Functions. A diagram for deep inelastic CC neutrino scattering is shown in Figure 2.3a. The four-momenta K and K' refer to the incoming and outgoing leptons, P and P' to the target nucleon (we will assume proton) and outgoing hadronic system.

The space-time properties of the current could, in general, contain terms which transform as Scalar (S), Pseudoscalar (P), Vector (V), Axial vector (A), and Tensor (T). Early β -decay experiments determined the current as $V - A$ for neutrinos and $V + A$ for antineutrinos.

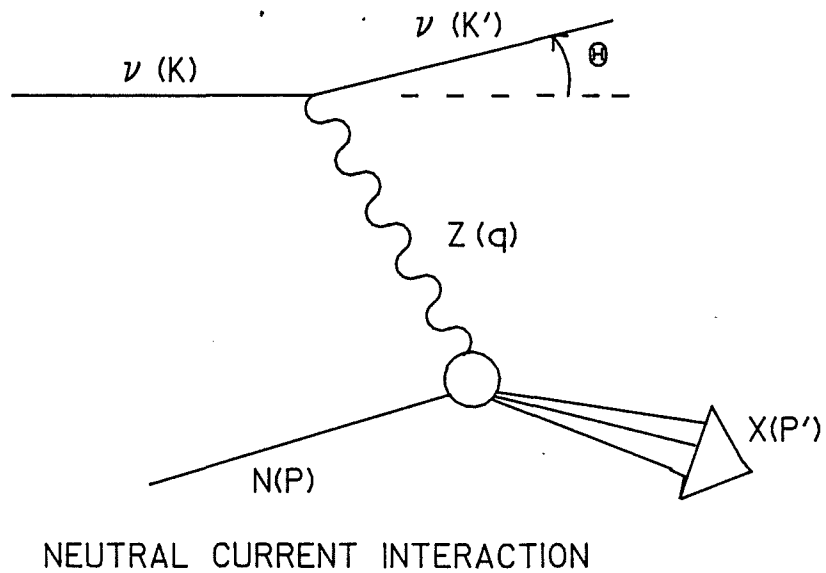
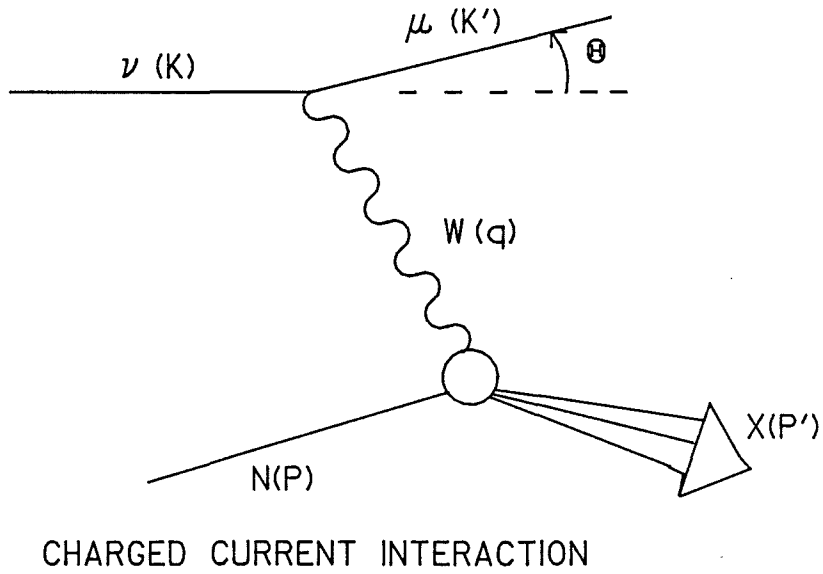


Figure 2.3. Neutrino-Nucleon Scattering (CC and NC Case)

Given V - A coupling, one can write the differential cross section for νp CC interactions as:

$$d\sigma = \sum_{K'} \sum_K \frac{1}{2E} \cdot \frac{d^3 K'}{(2\pi)^3 2E'} \cdot \frac{1}{2} \sum_P \sum_{P'} \frac{1}{2M} \int \Pi_n (2\pi)^4 \delta^4(P+K-P'-K') \quad (9)$$

$$* |M|^2 \frac{d^3 p'_n}{(2\pi)^3 2p'_{0n}}$$

where

$$M = \frac{G}{\sqrt{2}} \bar{u}(K') \gamma_\mu (1-\gamma_5) u(K) \langle P' | J_W^\mu | P \rangle \quad (10)$$

(Muon masses and W propagator terms have been ignored.). In Equation

10, G is the Fermi coupling constant, $G \approx 10^{-5}/M_p^2$, the $\sqrt{2}$ is a historical

artifact and J_W^μ is the weak current operator. We can write $|M|^2$ in

terms of a leptonic and a hadronic tensor. The leptonic tensor is:

$$L_{\mu\nu} = \sum_{K'} \sum_K \left[\frac{G}{\sqrt{2}} \bar{u}(K') \gamma_\nu (1-\gamma_5) u(K) \right]^\dagger \left[\frac{G}{\sqrt{2}} \bar{u}(K') \gamma_\mu (1-\gamma_5) u(K) \right] \quad (11)$$

and the hadronic tensor is:

$$W^{\mu\nu} = \frac{1}{8\pi M} \sum_P \sum_{P'} \int \Pi_n (2\pi)^4 \delta^4(P+K-P'-K') \langle P | J_W^{\mu\dagger}(0) | P' \rangle \langle P' | J_W^\nu(0) | P \rangle \quad (12)$$

$$* \frac{d^3 p'_n}{(2\pi)^3 2p'_{0n}}$$

The leptonic tensor can be evaluated using standard techniques and is

$$L_{\mu\nu} = 4G^2 \left[K_\mu K'_\nu - g_{\mu\nu} K \cdot K' + K_\nu K'_\mu - i \epsilon_{\alpha\mu\beta\nu} K^\alpha K'^\beta \right] \quad (13)$$

where $g^{\mu\nu}$ is defined in terms of the γ matrices, $2g^{\mu\nu} = \{\gamma^\mu, \gamma^\nu\}$ and $\epsilon^{\alpha\beta\gamma\delta}$

is a totally antisymmetric, fourth-rank tensor with

$$\epsilon^{0123} = -\epsilon_{0123} = 1.$$

The hadronic tensor cannot be evaluated directly because of the unknown weak-hadronic matrix element. What is known, is that $W^{\mu\nu}$ is a

second rank tensor and must be comprised of P and q (or P') which are

the only two independent variables. In general:

$$W^{\mu\nu} = -g^{\mu\nu} W_1 + \frac{P^\mu P^\nu}{M^2} W_2 - \frac{i \epsilon^{\mu\nu\alpha\beta}}{2M^2} P_\alpha q_\beta W_3 + \frac{q^\mu q^\nu}{M^2} W_4 \quad (14)$$

$$+ \frac{(P^\mu q^\nu + q^\mu P^\nu)}{M^2} W_5 + \frac{i(P^\mu q^\nu - P^\nu q^\mu)}{M^2} W_6$$

where the W_i 's are, in general, functions of ν and q^2 (or Q^2). Current conservation, $q_\mu W^{\mu\nu} = 0$, requires W_4 , W_5 , and W_6 be zero. This leaves:

$$W^{\mu\nu} = -g^{\mu\nu}W_1 + \frac{P^\mu P^\nu}{M^2} W_2 - \frac{i\epsilon^{\mu\nu\alpha\beta}}{2M^2} P_\alpha q_\beta W_3. \quad (15)$$

Contracting the lepton and hadron tensors (Equations 13 and 15), and writing the differential cross section in terms of the scattered muon energy and angle (in the laboratory frame) yields:

$$\frac{d\sigma^\nu}{dE' d\Omega'} = \frac{G^2 E'^2}{2\pi^2} \left[(\cos^2 \frac{\theta'}{2}) W_2^\nu + (2\sin^2 \frac{\theta'}{2}) W_1^\nu + \sin^2 \frac{\theta'}{2} (\frac{E+E'}{2}) W_3^\nu \right] \quad (16)$$

for the neutrino case. Similar calculations for the antineutrino CC case yield the same equation for the cross section except for a sign change on the W_3 term.

Under the assumption of Bjorken scaling:

$$M W_1(\nu, q^2) \xrightarrow{q^2, \nu \rightarrow \infty} F_1(x) \quad (17a)$$

$$\nu W_2(\nu, q^2) \xrightarrow{q^2, \nu \rightarrow \infty} F_2(x) \quad (17b)$$

$$\nu W_3(\nu, q^2) \xrightarrow{q^2, \nu \rightarrow \infty} F_3(x) \quad (17c)$$

where ν and q^2 approach infinity in such a way, that their ratio remains finite. We can define x ($x=Q^2/2M\nu$) and y ($y=\nu/E_\nu$) and perform a change of variables in Equation 16 from (E', Ω') to (x, y) . Under the assumption of scaling, the cross sections are given in their familiar form:

$$\frac{d\sigma(\nu, \bar{\nu})}{dx dy} = \frac{G^2 M E}{\pi} \left[(1-y) F_2(\nu, \bar{\nu})(x) + xy^2 F_1(\nu, \bar{\nu})(x) \pm (1-\frac{y}{2}) y x F_3(\nu, \bar{\nu})(x) \right]. \quad (18)$$

Notice that $d\sigma$ has the form:

$$d\sigma \approx E \cdot \sum_i [f(x)]_i \cdot [g(y)]_i,$$

which is factorized into equations of x and y , a consequence of scaling. The F_i (Equation 18) are known as the neutrino-nucleon structure functions. Over the last decade, much experimental work has been done to determine the nature of their x dependence.

2.2.2. The Parton Model, Quarks, and Structure Functions.

2.2.2.1. Parton Model for νp Interactions. Returning to Equation 8, it is now possible to specify and calculate the matrix element within the context of νp CC interactions. We will assume: (1) the V - A structure of the current, (2) J_μ^W as a weak, isospin raising operator, and (3) parity non-conservation. The equation can be written as:

$$\langle p'_i | J_\mu^W(0) | p_i \rangle = \bar{u}(p'_i) \gamma_\mu (1 - \gamma_5) u(p_i). \quad (19)$$

Squaring, and then summing over initial and final states yields:

$$8[p_{i\mu} p'_{i\nu} - g_{\mu\nu} p_i \cdot p'_i + p_{i\nu} p'_{i\mu} - i\epsilon_{\alpha\mu\beta\nu} p_i^\alpha p_i'^\beta]. \quad (20)$$

Substituting this into Equation 17, we then integrate over $d^3 p'$, rewriting the energy part of the delta function in terms of z and x and obtain:

$$W_{\mu\nu}(P, q) = \sum_n P_n \sum_{i=1}^N \int dz f_i^N(z) \frac{1}{ME_i'} \left[\frac{2P_\mu P_\nu z}{M\nu} - \frac{i}{M\nu} \eta_i \epsilon_{\mu\nu\alpha\beta} P^\alpha q^\beta - g_{\mu\nu} \right] x^P \delta(z - x) \lambda_i^2 \quad (21)$$

for νp interactions. The factors λ_i and η_i are explicitly shown in order to account for the V - A, isospin raising nature of the current, where

$$\begin{aligned} \lambda_i &= +1, \text{ for any } I_3 = -1/2 \text{ parton} \\ &= 0, \text{ otherwise} \end{aligned}$$

for νp scattering,

$$\begin{aligned} \lambda_i \rightarrow \bar{\lambda}_i &= +1, \text{ for any } I_3 = 1/2 \text{ parton} \\ &= 0, \text{ otherwise} \end{aligned}$$

for $\bar{\nu} p$ scattering, and

$$\begin{aligned} \eta_i &= +1 \text{ for partons} \\ &= -1 \text{ for antipartons.} \end{aligned}$$

Comparison of Equations 15 and 21 allows us to make the connections between νp structure functions and parton probability densities:

$$M W_1^{\nu}(\nu, q^2) = \sum_N P_N \sum_{i=1}^N f_i^N(x_i) \lambda_i^2 = F_1^{\nu}(x) \quad (22a)$$

$$\nu W_2^{\nu}(\nu, q^2) = 2 \sum_N P_N \sum_{i=1}^N f_i^N(x_i) x_i \lambda_i^2 = F_2^{\nu}(x) \quad (22b)$$

$$\nu W_3^{\nu}(\nu, q^2) = 2 \sum_N P_N \sum_{i=1}^N f_i^N(x_i) \eta_i \lambda_i^2 = F_3^{\nu}(x). \quad (22c)$$

Notice that $2xF_1 = F_2$, which is the Callan-Gross⁴⁵ relationship, a result of the assumption that the partons are spin-one-half. Also implicit in this analysis is that the masses of the partons are negligible. In the case of heavy partons, the "scaling" variable is no longer x but ξ , where:

$$\xi = x + \frac{m_h^2}{2M\nu},$$

m_h is the mass of the heavy parton. The relationships in Equation 22 still hold, but the cross section in Equation 18 no longer factors.

2.2.2.2. Parton-Quark Relationship. What are the partons? In 1964, Gell-Mann⁴⁶ and Zweig⁴⁷ proposed that the hadrons were made up of "quarks". The quark model had some success, especially in making sense of the large number of meson and baryon states which existed at that time. Only three quarks were needed to explain the existing mesons as quark-antiquark systems and baryons as three-quark systems.

When the SLAC ep data was combined with neutrino data from CERN, it was discovered that the quantum numbers of the partons matched those of the quarks. A fourth quark (charm) was predicted and was discovered in 1974. Since then a fifth (bottom) has been found and a sixth (top) is being sought and has probably been recently found. There is now firm theoretical and experimental evidence that the partons which participate

in the EM and Weak interactions are the quarks. Table 2.1 lists the quantum numbers of the first four quarks.

2.2.2.3. Quark Density Description of the Structure Functions. With these quantum numbers, we can write out the structure functions in terms of the quark densities. Let

$$\sum_N P_N \sum_{i=1}^N f_i^N(x) \rightarrow u(x), d(x), s(x), c(x)$$

represent the probability of finding a given quark at momentum fraction x , then

$$F_1^{\nu P}(x) = d(x) + \bar{u}(x) + s(x) + \bar{c}(x) \quad (23a)$$

$$F_2^{\nu P}(x) = 2x[d(x) + \bar{u}(x) + s(x) + \bar{c}(x)] \quad (23b)$$

$$F_3^{\nu P}(x) = 2[d(x) - \bar{u}(x) + s(x) - \bar{c}(x)] \quad (23c)$$

for neutrinos, and

$$\bar{F}_1^{\bar{\nu} P}(x) = u(x) + \bar{d}(x) + c(x) + \bar{s}(x) \quad (23d)$$

$$\bar{F}_2^{\bar{\nu} P}(x) = 2x[u(x) + \bar{d}(x) + c(x) + \bar{s}(x)] \quad (23e)$$

$$\bar{F}_3^{\bar{\nu} P}(x) = 2[u(x) - \bar{d}(x) + s(x) - \bar{c}(x)] \quad (23f)$$

for antineutrinos. The extension to νn and $\bar{\nu} n$ scattering is performed via the isospin relationship between protons and neutrons:

$$u_p = d_n = u, \text{ etc.}$$

Since most experiments are done using a (nearly) isoscalar target, the cross sections are written as in Equation 18:

$$\frac{d\sigma(\nu, \bar{\nu})}{dx dy} = \frac{G^2 ME}{\pi} \left[(1-y)F_2^{(\nu, \bar{\nu})}(x) + xy^2F_1^{(\nu, \bar{\nu})}(x) \pm \left(1 - \frac{y}{2}\right)yxF_3^{(\nu, \bar{\nu})}(x) \right]. \quad (18')$$

where

$$2xF_1^{(\nu, \bar{\nu})}(x) = F_2^{(\nu, \bar{\nu})}(x) = x\Sigma(x)$$

$$xF_3^{(\nu, \bar{\nu})}(x) = xV(x) \mp x\Delta(x)$$

Table 2.1. Quark Quantum Numbers

QUARK	Q	I	I_3	B	S	C
U	$+2/3$	$1/2$	$+1/2$	$+1/3$	0	0
D	$-1/3$	$1/2$	$-1/2$	$+1/3$	0	0
S	$-1/3$	0	0	$+1/3$	-1	0
C	$+2/3$	0	0	$+1/3$	0	1

and,

$$\begin{aligned}
 x\Sigma(x) &= xq(x) + x\bar{q}(x) \\
 xV(x) &= xq(x) - x\bar{q}(x) \\
 x\Delta(x) &= -[xs(x) + x\bar{s}(x)] + [xc(x) + x\bar{c}(x)] \\
 q(x) &= u(x) + d(x) + s(x) + c(x) \\
 \bar{q}(x) &= \bar{u}(x) + \bar{d}(x) + \bar{s}(x) + \bar{c}(x).
 \end{aligned}$$

The elementary cross sections for neutrino- and antineutrino-quark interactions, in units of $\frac{G^2ME}{\pi}$, are:

$$\begin{aligned}
 \frac{d\sigma}{dx dy} &= 1, \text{ for } \nu q, \bar{\nu}\bar{q} \\
 &= (1-y)^2, \text{ for } \nu\bar{q}, \bar{\nu}q.
 \end{aligned} \tag{24}$$

This is a consequence of basic helicity arguments.

2.2.2.4. Sum Rules. Various sum rules can be formed from the structure function-quark relationships. The Gross-Llewellyn-Smith sum rule⁴⁸ defines the quark-antiquark difference in the nucleon:

$$\int_0^1 \frac{x F_3(x)}{x} dx = 3$$

and indicates a nucleon carries three valence quarks. All other quarks in the nucleon come from a "sea" of quark-antiquark pairs. The Adler sum rule⁴⁹ exploits the isospin symmetry between protons and neutrons. Ignoring strange and charm quarks:

$$\int_0^1 \frac{1}{x} [F_2^{\nu n}(x) - F_2^{\nu p}(x)] dx = 2$$

and indicates that the proton's quark content is uud. Finally, the Callan-Gross relationship is:

$$2xF_1(x) = F_2(x).$$

This is a consequence of the spin-one-half nature of the quarks.

2.3. THE STANDARD MODEL.

Even though the quark-parton model has had some success, it remains, nonetheless, a phenomenological model. Work was done in the 1960's and early 70's to place weak interactions on a strong theoretical footing. At that time, a very good theory existed for Electromagnetic interactions, Quantum Electrodynamics (QED).

There existed many similarities between the EM and Weak interactions. Both processes involved the interaction of two currents. EM interactions also contained the effects of the photon propagator, whereas Weak processes resemble a four-particle point vertex (Fermi type interaction). In an attempt to gain a resemblance to the EM process, one could imagine that the Weak process is mediated by a heavy weak-boson. This would add a propagator term to the interaction. Then, in the limit of $q^2 \ll M_W^2$, the propagator term would be close to unity and the interaction would resemble a Fermi type interaction.

The Weak current in neutron decay is a charged current. Feynman and Gell-Mann⁵⁰ showed that the vector part of the current (the third component) is related to the isovector part of the EM current.

Finally, QED is a renormalizable theory. Weak interactions at the Fermi level are not. The dimensional coupling, G_F , with a dimension of inverse mass squared, gives rise to incurable divergences at higher orders of perturbation theory. Even adding a single heavy boson propagator "by hand" does not help.

2.3.1. The Weinberg-Salam Model for Leptons. The original conjecture of Weinberg⁵¹ and Salam⁵² gained possible relevance as a physical theory when it was shown by t'Hooft⁵³ that only if the

propagator acquires a mass through the spontaneous symmetry breaking⁵⁴ of the underlying theory can the theory be renormalizable.

An immediate prediction of the theory was the existence of weak neutral currents. Experiments at CERN⁵⁵ in 1973 discovered neutrino-nucleon neutral current interactions. Further experiments with CC, NC and neutrino-electron interactions, as well as recent discoveries of the charged⁵⁶ (W^\pm) and neutral⁵⁷ (Z^0) heavy bosons yields further credence to this model.

The Weinberg-Salam (WS) Model is based upon the $SU(2) \times U(1)$ gauge group. The leptons are organized into left-handed doublets:

$$L = \begin{pmatrix} \nu \\ e \end{pmatrix}_L,$$

and right-handed singlets:

$$R = (e)_R.$$

the projection operators are defined as:

$$L = \frac{1}{2}(1-\gamma_5)\begin{pmatrix} \nu \\ e \end{pmatrix}$$

$$R = \frac{1}{2}(1+\gamma_5)\begin{pmatrix} \nu \\ e \end{pmatrix}.$$

For complete generality, we should include a sum over all lepton families:

$$L = \sum_i L_i, \quad i = e, \mu, \tau$$

but for simplicity, we will only consider the electron family. The extension to other families is simple and obvious.

The generators of the gauge group are \vec{T} , the electronic isospin and Y , the electronic hypercharge. Hypercharge is related to the electric charge via $Q = T_3 + Y$. The interaction Lagrangian is constructed out of L and R , an isovector, spin-1 field, \vec{A}_μ and an isoscalar, spin-1 field, B_μ , (which couple to \vec{T} and Y , respectively), plus a spin-zero doublet field Φ , where

$$\phi = \begin{pmatrix} \phi^+ \\ \phi^0 \end{pmatrix}.$$

This "Higgs" field has a non-vanishing vacuum expectation value, $\langle 0 | \phi | 0 \rangle = v$, and will spontaneously "break" the underlying gauge symmetry.

The complete Lagrangian can be found in literature.⁵¹ The interaction Lagrangian for the lepton fields is:

$$\begin{aligned} L_{\text{int}} = & i\bar{R}\gamma^\mu (ig'B_\mu)R + i\bar{L}\gamma^\mu \left(\frac{1}{2}ig'B_\mu - \frac{1}{2}ig\vec{\tau}\cdot\vec{A}_\mu \right)L \\ & + \left| \left(\partial_\mu + \frac{1}{2}ig'B_\mu - \frac{1}{2}ig\vec{\tau}\cdot\vec{A}_\mu \right)\phi \right|^2 - G_\lambda (\bar{R}\phi^\dagger L + \bar{L}\phi R). \end{aligned} \quad (25)$$

By proper mixing of the massless boson fields, \vec{A}_μ and B_μ , we can form the real, physical boson fields:

$$W_\mu^\pm(x) = \frac{1}{\sqrt{2}} [A_\mu^1(x) \pm iA_\mu^2(x)] \quad (26a)$$

$$Z_\mu(x) = [-gA_\mu^3(x) + g'B_\mu(x)]/\sqrt{g^2 + g'^2} \quad (26b)$$

$$A_\mu(x) = [gB_\mu(x) + g'A_\mu^3(x)]/\sqrt{g^2 + g'^2} \quad (26c)$$

for the charged and neutral bosons and photon, respectively. Masses are assigned via the Goldstone⁵⁸ mechanism, which breaks the symmetry.

The couplings g and g' are related by:

$$\tan \theta_w = \frac{g'}{g} \quad (27)$$

where θ_w is called the "weak mixing angle" by Weinberg and the "Weinberg angle" by everyone else. The lepton Lagrangian can be written for a generic lepton field, " ℓ ", as:

$$\begin{aligned} L_{\text{int}} = & -g\sin \theta_w \bar{\ell}\gamma^\mu \ell A_\mu + \frac{g}{2\sqrt{2}} [\bar{\ell}\gamma^\mu (1-\gamma_5) \nu W_\mu^+ + \text{H.C.}] \\ & - \frac{g}{2} \frac{Z_\mu}{\cos \theta_w} \left[\frac{1}{2}\bar{\nu}\gamma^\mu (1-\gamma_5) \nu - \frac{1}{2}\bar{\ell}\gamma^\mu (1-\gamma_5) \ell + 2\sin^2 \theta_w \bar{\ell}\gamma^\mu \ell \right]. \end{aligned} \quad (28)$$

The EM and weak coupling constants are related by:

$$e = g \sin \theta_w.$$

The CC weak coupling constant, the W^\pm mass, and the Fermi coupling G_F are related by:

$$\frac{G_F}{\sqrt{2}} = \frac{g^2}{8M_W^2}.$$

The NC weak coupling is $g/\cos \theta_W$ and the Z^0 mass is predicted, in the "minimal" theory (one Higgs doublet), as:

$$M_Z^2 = M_W^2 / \cos^2 \theta_W.$$

The theory predicts left- and right-handed couplings of fermions as:

$$\delta_L = \tau_3 - Q \sin^2 \theta_W \quad (29)$$

$$\delta_R = -Q \sin^2 \theta_W$$

where Q and τ_3 are the particle's charge and third component of isospin, respectively.

2.3.2. Weinberg-Salam Extension to Hadrons. Based upon the success of the WS model for leptons, attempts were made to incorporate the hadrons (quarks). At that time, there were three quarks (u , d , and s) and they were incorporated into a left-handed isodoublet and three right-handed isosinglets:

$$q_L = \begin{pmatrix} u \\ d \end{pmatrix}_L, u_R, d_R, s_R. \quad (30)$$

This model correctly predicted all strangeness conserving semi-leptonic processes but predicted strangeness changing decays at a rate higher by a factor of 20. This led Cabibbo⁵⁹ to propose that the weak current contained a mixture of strangeness conserving and strangeness changing pieces:

$$d_c = d \cos \theta_c + s \sin \theta_c \quad (31)$$

$$s_c = -d \sin \theta_c + s \cos \theta_c,$$

where θ_c is the "Cabibbo" angle, $\sin^2\theta_c \approx 0.05$. This gave the correct form of the CC processes but predicted strangeness changing neutral currents at an unobserved rate.

A "minimal" model, proposed by Glashow, Iliopoulos, and Maiani,⁶⁰ (GIM), suggested a fourth quark, called "charm", which added a new isosinglet and an isodoublet:

$$q'_L = \begin{pmatrix} c \\ s \end{pmatrix}_L, c_R. \quad (32)$$

This new quark leaves the CC processes unchanged and adds a new piece to the NC Lagrangian but with the opposite phase with respect to the original strangeness changing piece thereby cancelling exactly (in the limit $M_u \approx M_c$).

The CC interaction Lagrangian for hadrons can be written as:

$$\begin{aligned} L_{cc} &= \frac{g}{2\sqrt{2}} [W_\mu^- J^{\mu+} + \text{H.C.}] \\ &= \frac{g}{2\sqrt{2}} [W_\mu^- \bar{u}\gamma^\mu(1-\gamma_5)d_c + \dots], \end{aligned} \quad (33a)$$

the EM piece as:

$$L_{em} = qJ_\mu^{\text{em}}A^\mu = \frac{2}{3} \bar{u}\gamma_\mu u A^\mu - \frac{1}{3} \bar{d}\gamma_\mu d A^\mu + \dots \quad (33b)$$

and the NC piece as:

$$L_{nc} = \frac{gZ^\mu}{\cos\theta_w} [J_\mu^3 - \sin^2\theta_w J_\mu^{\text{em}}], \quad (33c)$$

where

$$J_\mu^3 = \frac{1}{2} \bar{u}_L \gamma_\mu u_L - \frac{1}{2} \bar{d}_L \gamma_\mu d_L + \dots$$

The addition of the fourth quark was justified by the discovery of the Ψ/J meson in 1974. This scheme is easily extended to more quark families (we now have three) and it is possible to determine generalized Cabibbo matrices to mix the $I_3 = -1/2$ quarks.

2.4. NEUTRAL CURRENT NEUTRINO-NUCLEON SCATTERING.

A diagram of neutrino-nucleon neutral current scattering is shown in Figure 2.3b. As in the CC case, we can write this process as the interaction of a lepton and hadron current. The lepton piece is:

$$L^\mu = \frac{1}{2} \bar{\nu} \gamma^\mu (1 - \gamma_5) \nu \quad (34a)$$

and the hadronic piece is:

$$\begin{aligned} H_\mu = & \frac{1}{2} \delta_{uL} \bar{u} \gamma_\mu (1 - \gamma_5) u + \frac{1}{2} \delta_{uR} \bar{u} \gamma_\mu (1 + \gamma_5) u \\ & + \frac{1}{2} \delta_{dL} \bar{d} \gamma_\mu (1 - \gamma_5) d + \frac{1}{2} \delta_{dR} \bar{d} \gamma_\mu (1 + \gamma_5) d \end{aligned} \quad (34b)$$

which, in general, may contain both left- and right-handed pieces. For clarity, only u and d quarks are shown and (as in the CC case) we set $\theta_c = 0$ for simplicity. The couplings are defined in the WS-GIM model as:

$$\begin{aligned} \delta_{uL} &= \frac{1}{2} - \frac{2}{3} \sin^2 \theta_w \\ \delta_{dL} &= -\frac{1}{2} + \frac{1}{3} \sin^2 \theta_w \\ \delta_{uR} &= -\frac{2}{3} \sin^2 \theta_w \\ \delta_{dR} &= \frac{1}{3} \sin^2 \theta_w. \end{aligned} \quad (35)$$

We could then proceed and calculate the cross sections as before, however, by using the elementary cross sections already developed, (Equation 24) we can write (for an isoscalar target):

$$\begin{aligned} \frac{d\sigma^\nu}{dx dy} = & \frac{G^2 M E}{\pi} \{ x q(x) [(\delta_{uL}^2 + \delta_{dL}^2) + (1-y)^2 (\delta_{uR}^2 + \delta_{dR}^2)] \\ & + x \bar{q}(x) [(1-y^2) (\delta_{uL}^2 + \delta_{dL}^2) + (\delta_{uR}^2 + \delta_{dR}^2)] \}. \end{aligned} \quad (36)$$

In terms of the structure functions:

$$\frac{d\sigma^\nu}{dx dy} = \frac{G^2 M E}{\pi} \left[(1-y) F_2^\nu(x) + xy^2 F_1^\nu(x) + (1 - \frac{1}{2}y) xy F_3^\nu(x) \right], \quad (37)$$

where:

$$\begin{aligned} 2xF_1^\nu(x) = F_2^\nu(x) = & x\Sigma(x) [\delta_{uL}^2 + \delta_{dL}^2 + \delta_{uR}^2 + \delta_{dR}^2] \\ & + x\Delta(x) [\delta_{uL}^2 + \delta_{uR}^2 - \delta_{dL}^2 - \delta_{dR}^2], \end{aligned}$$

$$xF_3^{\nu}(x) = xV(x) \left[\delta_{uL}^2 + \delta_{dL}^2 - \delta_{uR}^2 - \delta_{dR}^2 \right].$$

Similar equations can be written for antineutrino scattering.

Within the WS-GIM model, certain predictions can be made about CC and NC interactions. Of particular interest are the ratios:

$$R_{\nu} = \frac{\nu N \rightarrow \nu X}{\nu N \rightarrow \mu^- X}, \quad R_{\bar{\nu}} = \frac{\bar{\nu} N \rightarrow \bar{\nu} X}{\bar{\nu} N \rightarrow \mu^+ X}.$$

The standard model predicts, with $\sin^2 \theta_w = 0.23$, and minimal Higgs symmetry breaking, $R_{\nu} = 0.30$ and $R_{\bar{\nu}} = 0.38$. Current data are in excellent agreement with these predictions. (See Baltay⁶¹ for an excellent review.)

CHAPTER 3. THE E594 DETECTOR

3.1. GENERAL OVERVIEW

The E594 detector is a fine-grained, massive detector suitable for neutrino calorimetry. The fine-grain nature is useful for measuring both the energy and direction of showers, as well as differentiating between hadronic and electromagnetic showers. Since neutrino reactions are rare, especially neutrino-electron elastic interactions, the detector must also be massive. The detector is based upon plastic flash chambers and aluminum-extruded proportional tube planes. These devices allow us to build a detector with excellent pattern recognition at an acceptable cost.

The detector has two parts: a flash chamber calorimeter and an iron toroidal spectrometer (see Figure 3.1). This Figure illustrates the configuration of the detector during the NBB run period. For the 1981 Engineering run, the active area of the calorimeter was 12 ft X 12 ft in cross section and 40 feet in length. It consisted of 416 flash chambers and 25 proportional tube planes. One module of the detector consisted of four, 4 inch wide steel box beams with 4 chambers per beam. The chambers were in sequence U-X-Y-X, where X chambers have horizontal cells and Y and U chambers have cells oriented $\pm 10^\circ$ from vertical, respectively. Flash chambers have 5 mm X 5 mm cell size and each chamber contains approximately 635 cells. Each chamber is read out, using magnetostrictive techniques, from both ends of a wand placed

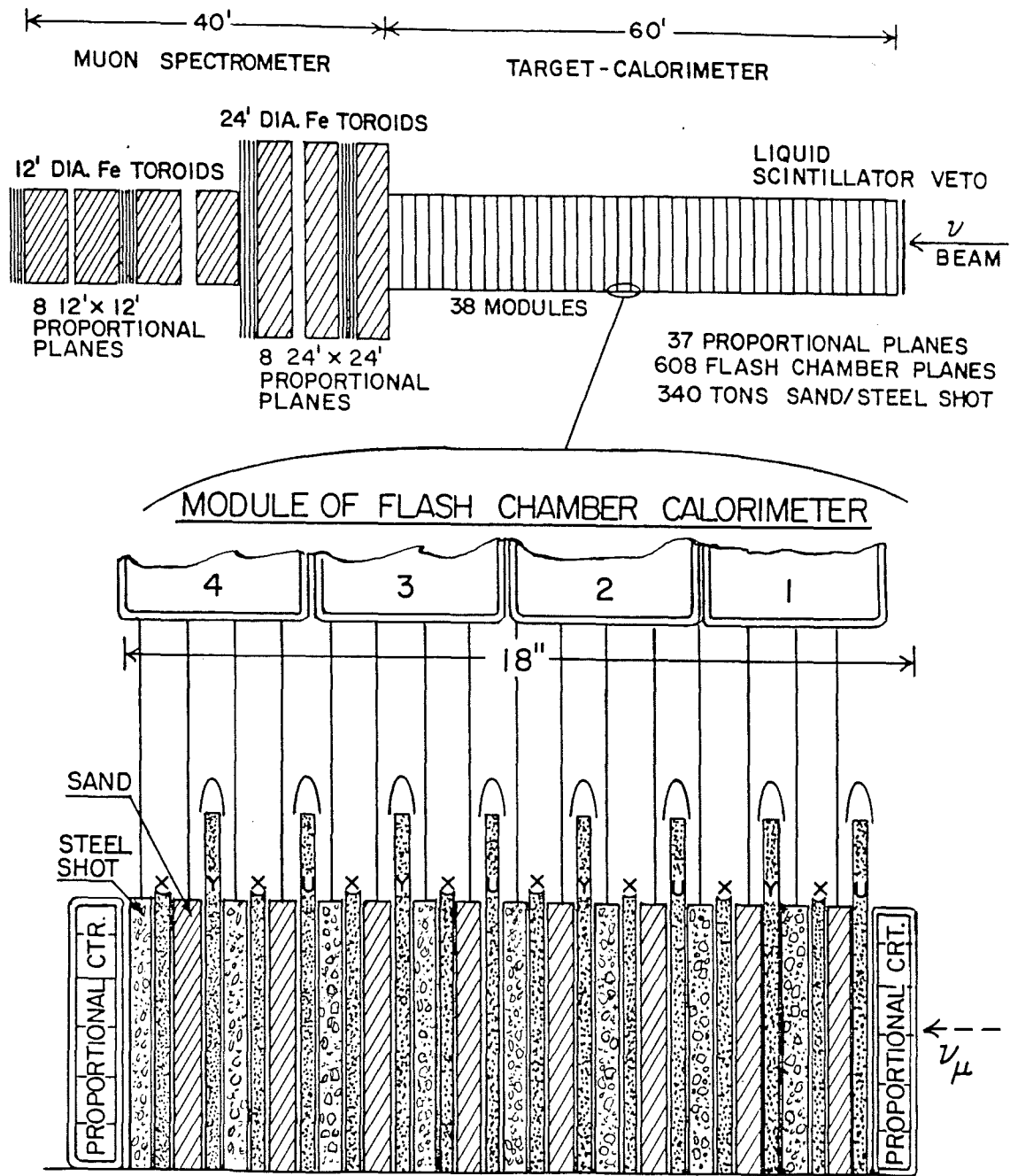


Figure 3.1. The E594 Detector

across the cells. The flash chambers are sandwiched between 5/8 inch thick acrylic extrusions which are alternatively filled with sand or with steel shot. These filled extrusions form the target mass of 240 metric tons.

The proportional tube planes alternate X-Y (wires running horizontally and vertically) throughout the detector and are placed after each flash chamber module (16 chambers). The proportional tubes have 1 inch cell size and provide both a trigger and an independent measure of the shower energy. Liquid scintillation counters are placed every five modules (80 chambers) and provide a muon trigger for calibration purposes and software alignment of the flash chambers. A liquid scintillation counter was placed in front of the calorimeter to veto on incident charged particles.

The iron spectrometer followed the calorimeter and consisted of three, 24 foot diameter toroids and four, 12 foot diameter toroids. Proportional tube planes with a one inch cell size were placed in the toroid gaps. For the 1981 Engineering run, only the second and fourth 12 foot toroid gaps contained proportional tube planes. Each gap contained both X and Y planes. These planes were "double" planes. Two layers of cells, with the second layer offset by 1/2", comprised one "double" plane. Large 24 foot planes were installed behind the last 24 foot toroid but were not operational during most of the 1981 run.

The average sampling step of the flash chambers is 3.6 g/cm^2 , corresponding to 22% of a radiation length and 3% of an absorption length. The average distributed density of the calorimeter is 1.4 g/cm^3 , and the average Z is 19.1. This construction offers a good

compromise for angular and energy resolution and neutrino event rate, optimized for the physics we studied.

3.2. THE FLASH CHAMBERS

3.2.1. Construction. Each chamber was constructed from three, 4 foot wide black polypropylene sheets to form an active area of 12' X 12'. The three sheets are fastened together with mylar tape to prevent sparking through the seams between the polypropylene sheets. Aluminum foil sheets, 5 mil thick and 36 inch wide by 14 feet long, are glued to each side with a water based latex contact glue to the polypropylene to form the high voltage (HV) electrodes. The foil is overlapped and is fastened together by conductive aluminum tape. The HV electrodes are cut back 12" from the gas manifolds to quench the plasma discharge before it reaches the gas manifolds eliminating cell-to-cell cross talk.

The gas manifolds are made by welding translucent polypropylene strips around the ends of each of the 4 foot wide polypropylene sheets. The ends of the gas manifolds are fused together by heat to form a complete seal. The use of a polypropylene manifold avoids outgassing problems as well as avoiding strength uncertainties associated with adhesive bonding to the polypropylene.

Standard 90% Ne-10% He gas, with small amounts of Argon and other impurities as quenchers, is used in the chambers. The gas flows through the chambers at the rate of 1.5% of the chamber volume per minute. The gas is continuously purified, replenished and recirculated using a molecular sieve gas purification system. This gas purification system is detailed later.

To achieve good efficiency independent of location on the chambers, the high voltage pulse must have a duration of approximately 500 μ sec at a voltage of 5 kV. The HV rise time is critical in initiating the plasma discharge within the chamber cells. Measurements⁶² show the chamber efficiency degrades by 14% if the high voltage rise time is increased from 40 to 100 nsec. The duration of the pulse is critical in sustaining the plasma discharge long enough for it to propagate through the cell to the readout section. At 5 kV, the propagation speed is roughly 10 nsec/foot⁶² and this speed has a weak dependence on the applied voltage.

The high voltage pulse is produced by a pulse forming network (PFN). Each chamber has its own PFN. The PFN has a capacitance of roughly 100 nF, with the capacitance distributed in three stages to insure a fast rise time and a sustained pulse. The HV system and HV monitoring is detailed later. The HV pulse is fed into the chamber by a 30" wide HV tongue at the lower corner (for X chambers) or at the side (for U and Y chambers) and is terminated by two 10 Ω , 2 Watt carbon resistors. No significant variation of the HV pulse is observed at different locations on the chamber.

The flash chambers are read out using magnetostrictive wire techniques to detect the current pulse induced by the plasma discharge in a struck cell. The current pulse is induced on 0.118" (3 mm) wide copper strips about 20" long and glued to the outside surface of the polypropylene sheets about one foot from the edge of the polypropylene. These copper strips are connected to the chamber ground plane and form a set of capacitors (one for each cell) with the chamber HV plane acting as the other side of the electrode. The plasma discharge, once it has

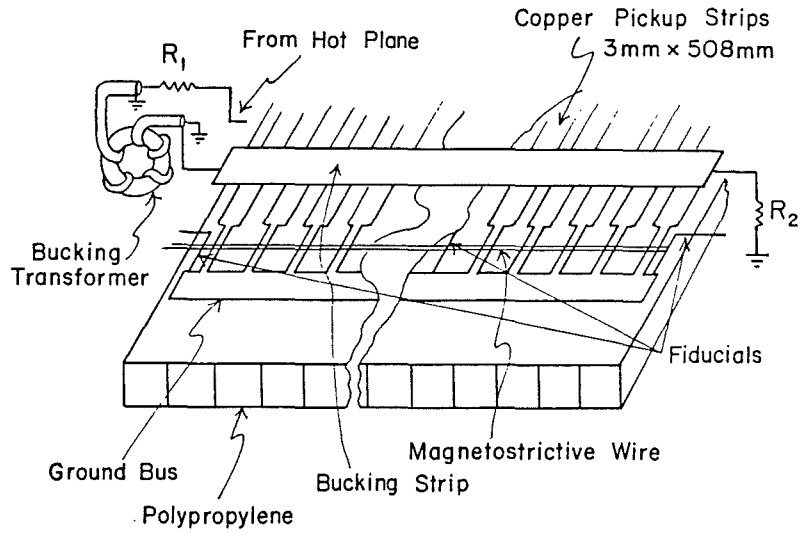
propagated along the length of the cell causes the capacitance between the copper readout strips and the HV plane to change. This induces about a 0.5 A current pulse to flow through the copper strips to ground. The copper strips are made of photoetched copper clad mylar sheets with appropriate cell-to-cell spacing. On the photoetched mylar, each strip is connected to a ground bus via a narrow "sense wire".

A 5 X 12 mil Remendur 27 magnetostrictive wire is laid over the sense wire region. The current pulse from a struck cell causes an acoustic pulse to propagate down the magnetostrictive wire. The acoustic pulse propagates at approximately 5000 m/sec, corresponding to a 1 μ sec separation between adjacent hit cells. Figure 3.2 shows a schematic diagram of this construction.

When the chamber operates in the plateau region, the plasma induced current pulse is roughly five times larger than the no plasma induced current pulse. To improve this signal to noise ratio a type of ac bridge is made which balances the current through the sense wires. The bridge is produced by a 1:1 inverting transformer connected to the HV plane of the chamber. The inverting transformer applies an opposite polarity pulse to a 2" wide Aluminum "bucking strip" laid perpendicularly across all of the read out strips (see Figure 3.2). The pulse is optimized by input resistance (R_1) and output resistance (R_2). This reduces unwanted capacitive pickup by a factor of 3 to 4. Since the operation of the bucking strip is determined by geometry, no chamber to chamber tuning is necessary. Figure 3.3 shows typical pulses from the magnetostrictive amplifier with the bucking current turned on and turned off. A typical signal to background ratio of 10:1 to 20:1 is achieved when using a properly tuned bucking circuit.

READ OUT SCHEME

TOPVIEW



SIDE VIEW OF READOUT

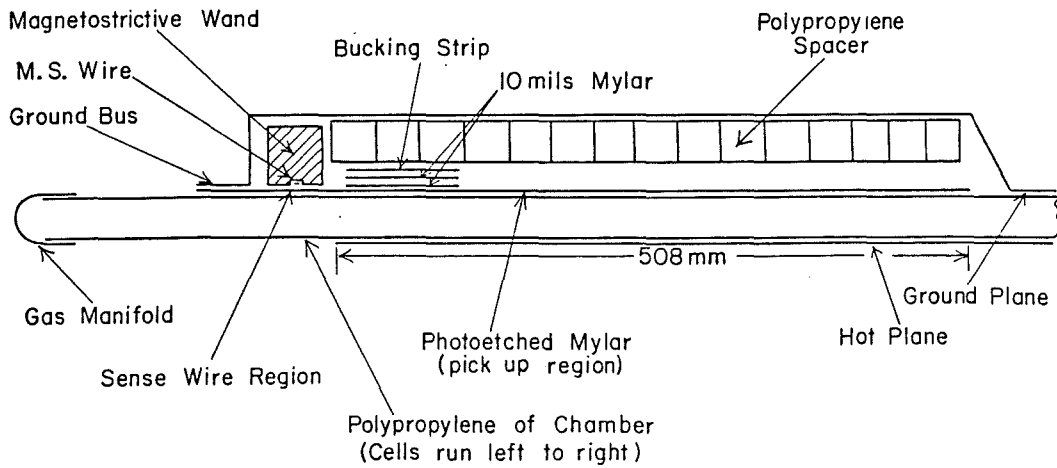


Figure 3.2. Construction of Flash Chamber Readout

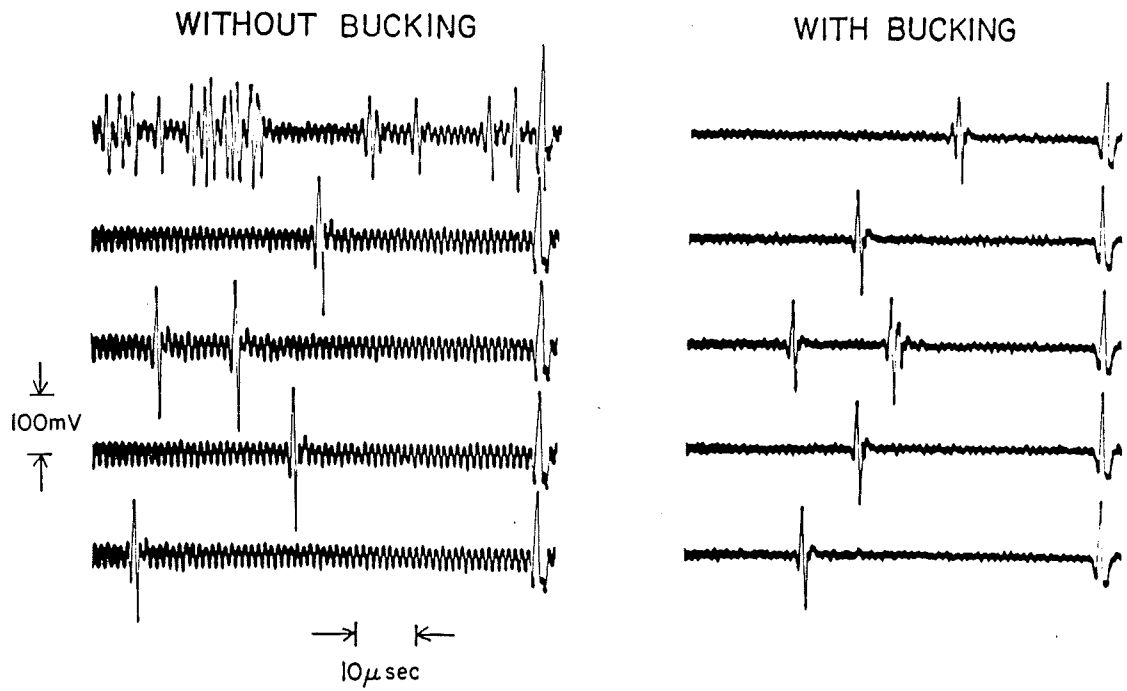


Figure 3.3. Voltage Output from Magnetostrictive Amplifier

The magnetostrictive wire is held in a 10 mil deep groove in a long extruded aluminum bar (wand). A solenoidal coil is wound around the entire length of the wand to periodically magnetize the magnetostrictive wire. During data taking the wire was magnetized every 200 events (one event per accelerator cycle). We found that there is an optimum magnetization of the wire which minimizes dispersion and limits the attenuation of the acoustic pulses down six feet of wand to less than 20%. Amplifiers with a gain of approximately 10^3 at each end of the wand provide analogue signals for the readout system.

Three fiducials, one at each end and one in the middle of the chamber calibrate the wand. Typical amplitudes from the flash chambers are in the 100 to 200 mV range. Using two amplifiers on each wand limits the number of cells which must be monitored by each amplifier.

Each wand amplifier feeds a discriminator circuit which in turn clocks a 1024×1 memory. The discriminator threshold is programmed with an exponentially decreasing function to compensate for the 20% attenuation of signals from the middle fiducial regions. The clocking of the memory advances at a frequency such that $2+\epsilon$ (ϵ is a small number) counts occur per microsecond. The use of this clock frequency avoids synchronization problems caused by slight variations in the cell separation. The memory boards are read out asynchronously into CAMAC to a PDP 11/45 computer.

3.2.2. Performance.

3.2.2.1. Efficiency. The chambers were tested using cosmic ray muons and "beam" muons from upstream neutrino interactions. Initial tests of the chambers' performance were performed using the standard 90% Ne-10% He gas. The high voltage characteristics are shown in Figure

3.4. The chambers roughly follow the same curve and reach an efficiency plateau of 90% in the range from 3.75 kV to 5 kV. Roughly half of the 10% inefficiency is due to the inner wall thickness which separates individual cells. The remaining 5% inefficiency is thought to be due to recombination of the initial ionization electrons and due to the sweeping of these electrons by the HV pulse before the avalanche mechanism begins. Multiplicity is defined to be the number of neighboring cells which fire due to the ionization in one cell. The multiplicity per trigger is shown in Figure 3.4 and is a slowly increasing curve.

The uniformity of the high voltage response of a chamber has been tested by measuring the HV plateau of selected chambers at various locations on each chamber. The results of the study show that the chamber is uniformly efficient over the entire 12' X 12' active area for a high voltage ≥ 3.75 kV.

The chamber efficiency versus trigger delay has been investigated.⁶² The sensitivity is dependent upon gas flow, but at a flow of 1.5% volume/min, the efficiency drops roughly 16%/μsec. Higher flow allows higher efficiency. Flash chamber recovery time is measured as the probability for a given struck cell to reignite as a function of the time between triggers. The reignition probability is roughly 6-8% after a 10 second repetition rate.

Extensive tests were begun to determine if the refire probability could be decreased even more by the addition of a small amount of electro-negative gas. The gas chosen is usually O₂, or CO₂. In our case, a fraction of the recirculating gas is reinjected into the chambers without passing through the purification sieves. Refire

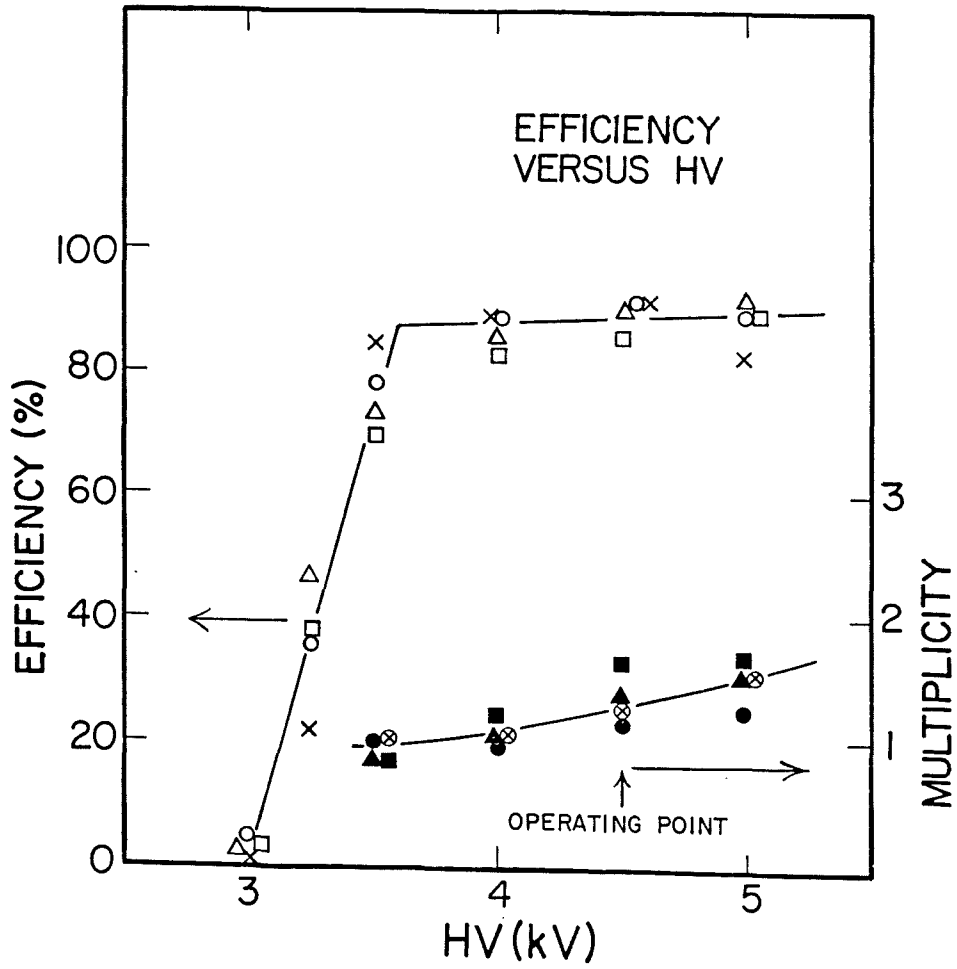


Figure 3.4. Flash Chamber Efficiency and Hit Cell Multiplicity

depends upon both the amount of "dirt" and upon the applied high voltage. It was decided⁶³ to reduce the applied high voltage from 9kV to 8.5kV as our gas sample changed from Ne-He to a mixture of Neon, Helium, and dirt. Unfortunately, these two changes reduce the efficiency of the flash chambers. The impure gas contains water vapor. The water vapor diffuses through the chamber walls and its amount is strongly correlated to the absolute humidity in Lab C. Since water is a strongly polar molecule, the ionization electrons are attracted to the water vapor and this depletion reduces the chances for the plasma to develop. To compensate for this efficiency drop, a small amount ($\approx 0.2\%$) of Argon is added to the gas. Argon increases the primary ionization which in turn increases the chances for the plasma to develop.

Thus, starting in January 1981, the standard gas running conditions were: 96% Neon, 4% Helium, $\approx 0.04\%$ Oxygen (and Nitrogen), 0.17% Argon, and ≈ 0.05 to 0.08% water vapor (depending upon humidity). As a result of these changes, the refire probability was reduced from 6-8% to 1-2% at a 10 second repetition rate. The efficiency does not suffer too badly, and is $\approx 70-74\%$ at the minimum delay of approximately 700 nsec. This delay is the time between the muon transversing the chambers and the HV being applied to the flash chambers. It has been found that doubling the gas flow rate does not improve the efficiency appreciably.

3.2.2.2. Stability. The stability of the flash chambers was monitored during the WBB run. Runs in which we used the scintillation tanks to trigger on beam and cosmic muons were used to determine efficiency and refire probability. Figure 3.5a shows the efficiency as a function of time. The error bars shown are all equal to $\pm 0.6\%$ as derived from data. It is evident, however, that the graph shows a

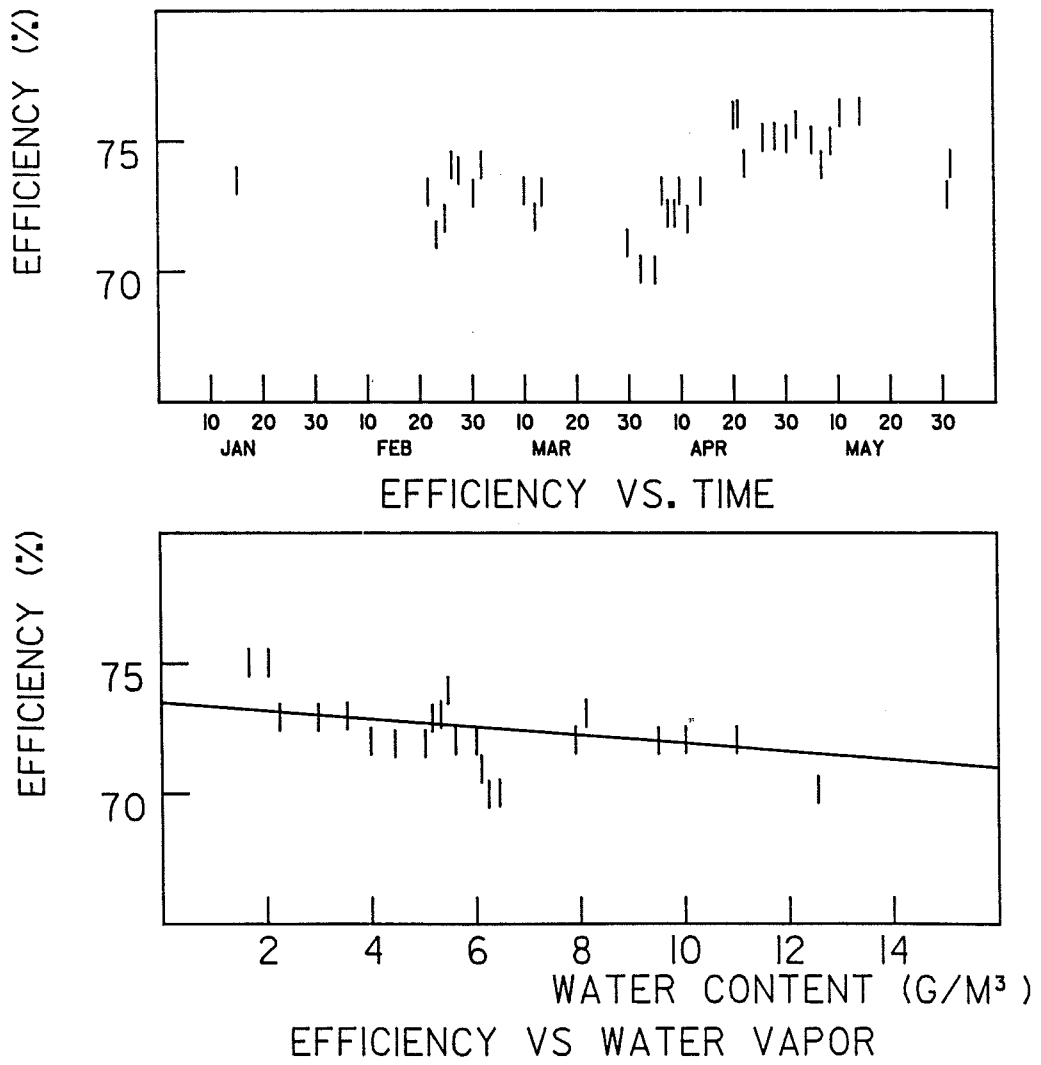


Figure 3.5. Efficiency Stability During WBB Run

greater dispersion of the data than suggested by the error bars. This dispersion reflects the variation of parameters which affect the chamber efficiency. The amount of water vapor in the chambers is one of these factors. The average efficiency is shown in Figure 3.5b. The average efficiency drops about 0.15% per 0.01% of water vapor by volume. Since one third of the recirculating gas was reinjected into the chambers without filtering, the actual proportion of water at the center of the chamber is less by a factor of two thirds.

The high efficiency region in Figure 3.5a from April 18 through May 20 is in part due to low atmospheric humidity, but two other factors were involved. On April 18, a high voltage monitoring system was installed. With monitoring, it was possible to identify chambers with low efficiencies due to HV pulse problems and to correct the PFN. Also, the muon trigger was changed. The change allowed for muons which were more perpendicular to the chambers. The chambers are more efficient to these types of tracks. Figure 3.5b shows the correlation between absolute humidity and the amount of water vapor in the gas. Apart from one possible mismeasurement, and a few temporary leaks in the gas cart, the correlation is strong. The refire probability during the five month running period was $1.5 \pm 0.25\%$.

A quick check was made at the end of the run on the operating characteristics of the flash chambers. We checked the efficiencies and refire probabilities as well as the reproducibility of the delay curves and the HV plateau curves. The chambers were tested using the standard high voltage and gas mixture given above. The humidity in LAB C was constant and high ($\approx 10-11 \text{ g/m}^3$). Figure 3.6 shows the delay curves and HV plateau curves from the test. For comparison, the curves from

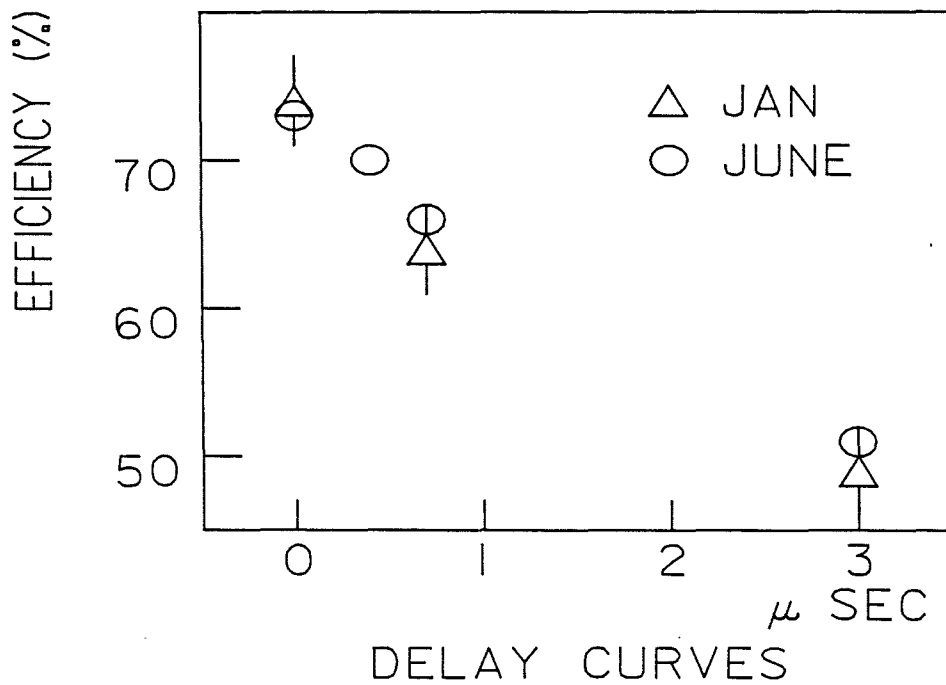
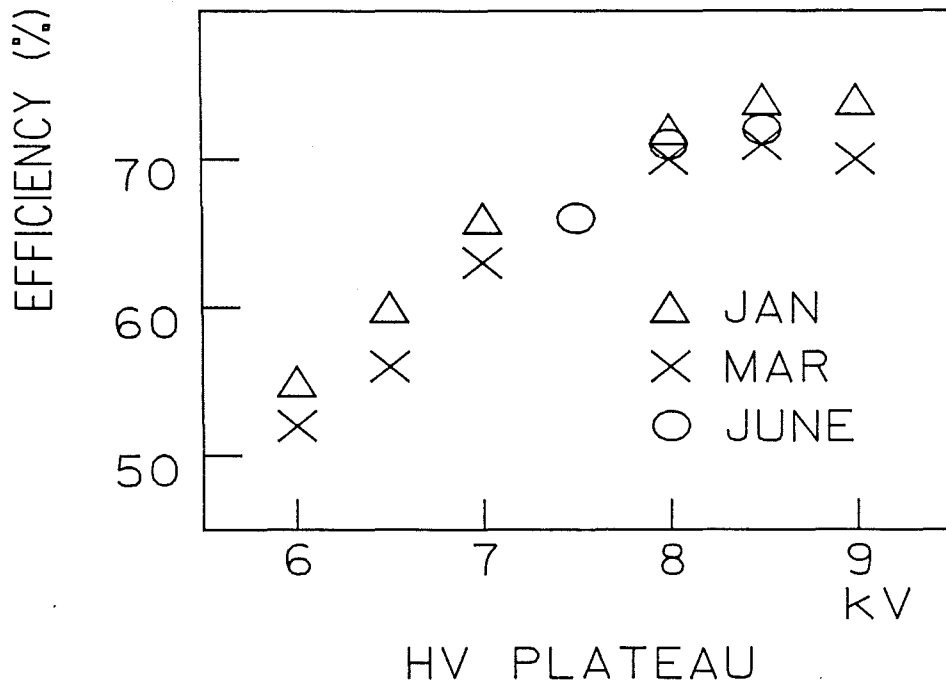


Figure 3.6. Efficiency and Delay Measurements - June 1981

earlier tests are shown. The curves are stable within the running period within the fluctuations noted before. The efficiency drop is approximately 12% per microsecond in the region from "minimum delay" to "minimum delay" + 700 nsec. The average efficiency was approximately 70-74%, and the average refire probability was $1.5 \pm 0.25\%$ at a 10 second repetition rate.

3.3. THE GAS CART

3.3.1. Gas Flow. The 416 flash chambers represent a volume of about 37 m^3 (1300 ft^3). From the chamber efficiency studies, the efficiency plateaus, at fixed trigger delay, occur at a flow rate of about one volume change per hour.

Two gas recirculators were built. Each recirculator has a flow capacity of about 900 l/min. Although one recirculator would have been sufficient, two were built to provide an extra margin of safety in case higher gas flows were required and to serve as a backup in case of mechanical failure. The basic system is an upgrade of the recirculator used at SPEAR on the Mark II experiment.⁶⁴

With the addition of "dirt" into the standard gas mixture, both recirculators were used. One "gas cart" would purify a fraction of the total volume ($13.3 \text{ ft}^3/\text{min}$) while the second merely recycled the remaining gas ($10 \text{ ft}^3/\text{min}$) back into the chambers.

The rugged flash chamber construction eliminates the need for delicate pressure regulation. The overall system pressure reference point is established by a regulator on an NeHe backfill bottle. This gas reservoir makes up for any system losses due to leaks or diffusion. Overall flow rate is controlled by a variable feedback adjustment on the

two-stage blowers by means of a butterfly valve which routes a percentage of the gas into the flash chambers. The blowers themselves run at a constant rate. A M-D Pneumatics rotary blower model 57/81 with a butterfly valve controlled feedback loop was used.⁶⁵ More detailed adjustment was possible using individual flowmeters which serviced combinations of four chambers.

3.3.2. Gas Purification. The gas is cleansed by passing it through two molecular sieves, one operating at room temperature, the other at liquid Nitrogen temperatures. Two pairs of sieves resided on each cart, one undergoing cleansing by being baked and pumped with a vacuum pump while the other was on-line. Details of the plumbing is shown in Figure 3.7.

The molecular sieves consist of two stainless steel cylinders of 66.7 liter volume, filled with 41 kg each of 3 mm Linde 13X molecular sieve pellets. One sieve is run at room temperature to trap water vapor and the other at liquid Nitrogen temperature (-196°C) to remove Oxygen and Nitrogen. Argon was also trapped out in the cold sieve and had to be continuously added to the purified gas going back to the chambers.

In normal operation, the sieves are cycled from temperatures of -196°C to 290°C . Heat shields were placed surrounding the heating coils to prevent uneven heating of the dewars. Temperature regulation during the heating cycle inside the dewars was accomplished by a chromel-alumel thermocouple control device⁶⁶ and temperature was monitored with a commercial iron-constantan thermometer.

At a flow rate of 600 l/min, nearly 14.3 kcal/min of heat is removed from the incoming gas to cool it to liquid Nitrogen temperatures, while the same amount must be added to the outgoing gas.

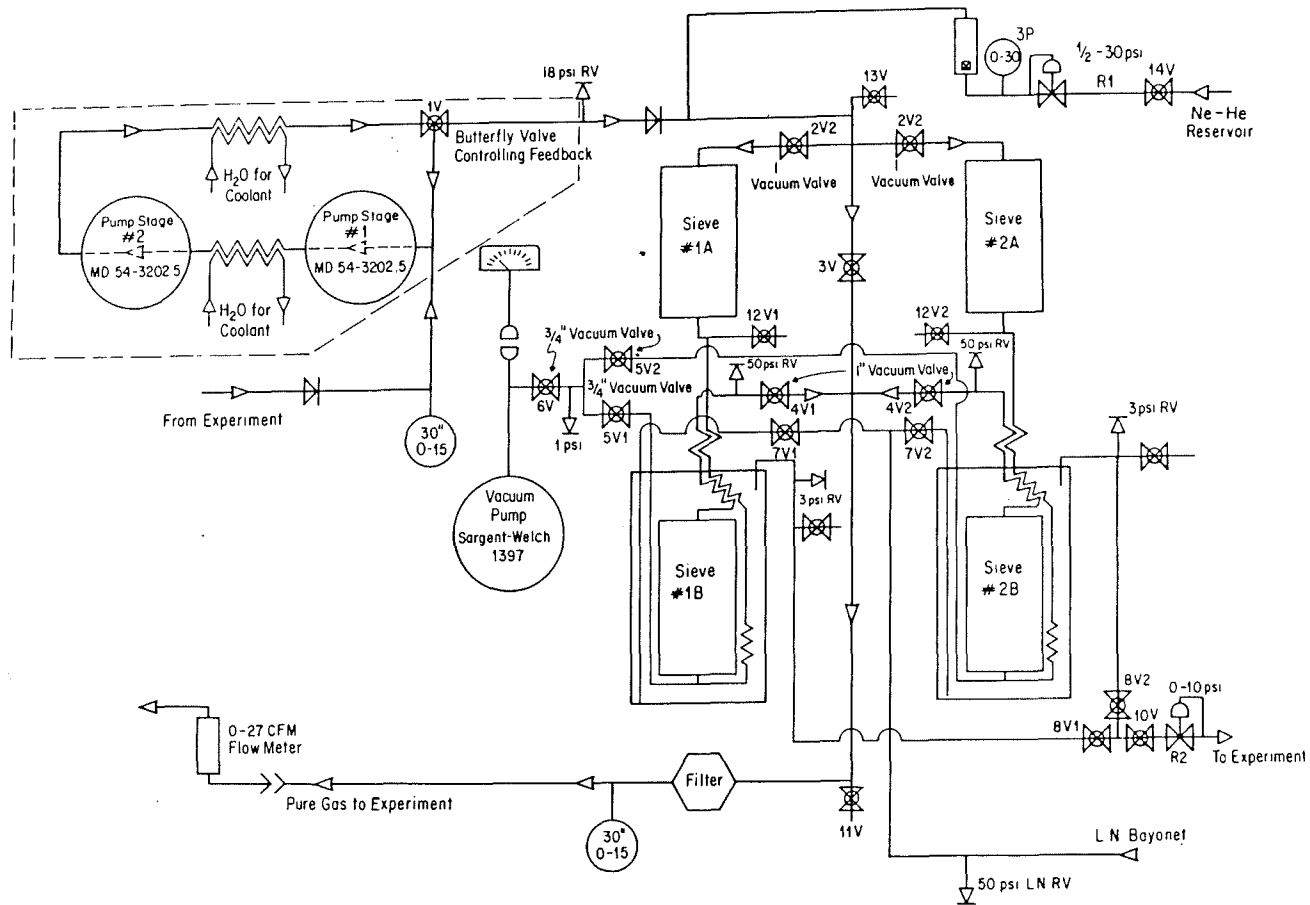


Figure 3.7. Schematic of Gas Recirculator

If this were accomplished simply by boiling off Nitrogen with no recovery, the usage of LN_2 would be large. Internal heat exchangers were used in the dewar to (1) facilitate faster cooling/warming of the gas and (2) to reduce Nitrogen consumption. After the WBB, large external exchangers were added.⁶⁶

3.3.3. Gas Monitoring. Under normal conditions, the gas is pushed through the chambers where it picks up Oxygen, Nitrogen and water vapor. A small quantity of gas is lost through leaks in the chambers and some Helium is lost due to diffusion. The gas returns to the cart at a small overpressure (4-6 mm of Hg) carrying about 600 ppm each of O_2 and N_2 . The amount of water vapor varies with the absolute humidity, but can approach 600 ppm. After purification, the $\text{O}_2/\text{Ar}/\text{N}_2$ content drops to less than 30 ppm. The operation of the system was checked three times daily by means of a two column chromatograph. We used a model 69-550 gas chromatograph manufactured by Gow-Mac Instrument Company.⁶⁷

Under normal conditions, with our standard gas mixture, a sieve would become saturated after about three days. Saturation is detected by an increasing O_2 content in the post sieve gas which grows to about 20% of the input level within 12 hours. The cleansing cycle takes about four days: one for boiling, two for evacuation, and one for cooldown. Since we had four sieves on two carts, one sieve would be on-line, two being cleansed, and the last cooled down and ready to come on-line. The presence of Argon in the gas greatly reduces the saturation time as it is trapped out in the cold sieve. Had we run with straight NeHe gas with no bypass, the saturation time increases to 7-10 days.

3.4. THE HIGH VOLTAGE SYSTEM

3.4.1. Overview. Each chamber had its own pulse forming network (PFN) to produce the HV pulse. A schematic of the PFN circuit is shown in Figure 3.8a. Direct current high voltage (DCHV) charged up the capacitors. The spark gap acts as the switching element and uses a spark plug in the gap. High voltage thyratrons provided the trigger pulse. Upon receiving a trigger, the charge stored on the capacitors is switched to the chamber. The chamber has a capacitance of roughly 100 nF, so half of the charge on the PFN is transferred to the chamber. A typical HV pulse is shown in Figure 3.8b.

A mini-computer controlled monitoring system (PQD) was installed to check the PFN performance on a pulse-by-pulse basis. The PQD monitors the total charge applied to the chambers, the timing of the HV pulse and verifies that no spurious pulsing occurs between triggers. The monitoring system is detailed later.

A block diagram of the high voltage system is shown in Figure 3.9. Multipurpose distribution panels service 8 PFN's. The panels provide DCHV, the HV thyatron pulse, dry N₂ gas for the spark gaps and bulkhead lemo feed-through connections to link the HV monitor signals from the PFN's to the PQD. One thyatron pulser usually serviced 10 distribution panels, with a single power supply (Hipotronics, model 815-75, 15 kV-15 mA) for all of the thyratrons. There are 8 PQD units, each servicing up to 80 chambers and interfaced to an LSI 11/23 computer. Two main DCHV power supplies (Hipotronics, model 815-335, 15 kV-335 mA) supplied up to 9 kV to one half of the 608 NBB detector, one supply was used for the 416 WBB detector. Each supply feeds a fan-out box, each box supplying up to 40 distribution panels.

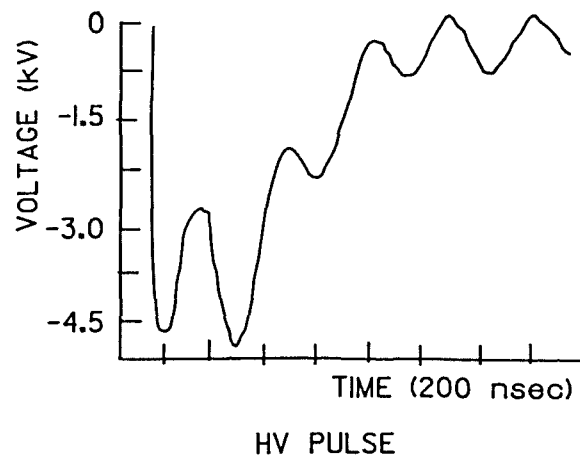
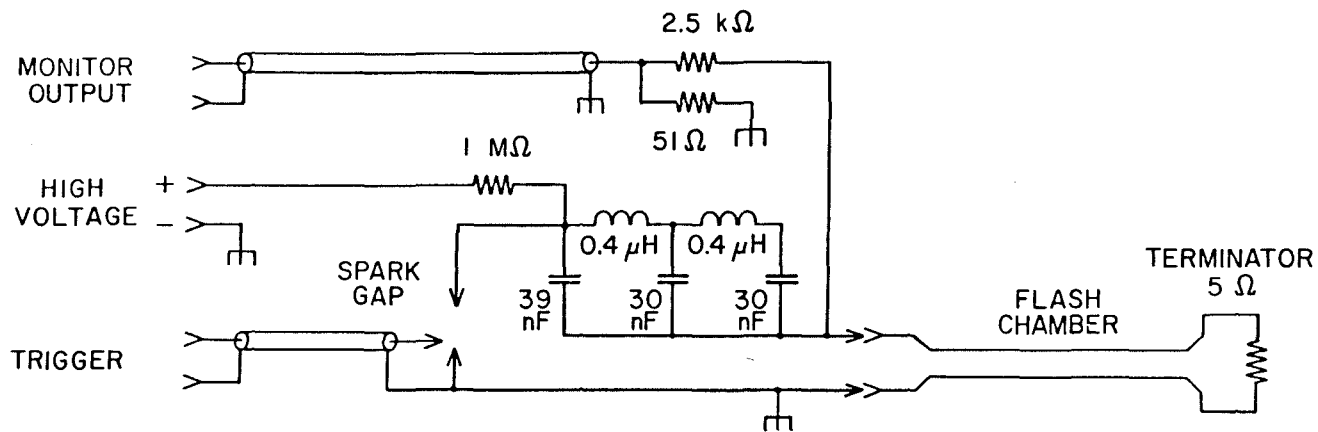


Figure 3.8. PFN Circuit and High Voltage Pulse

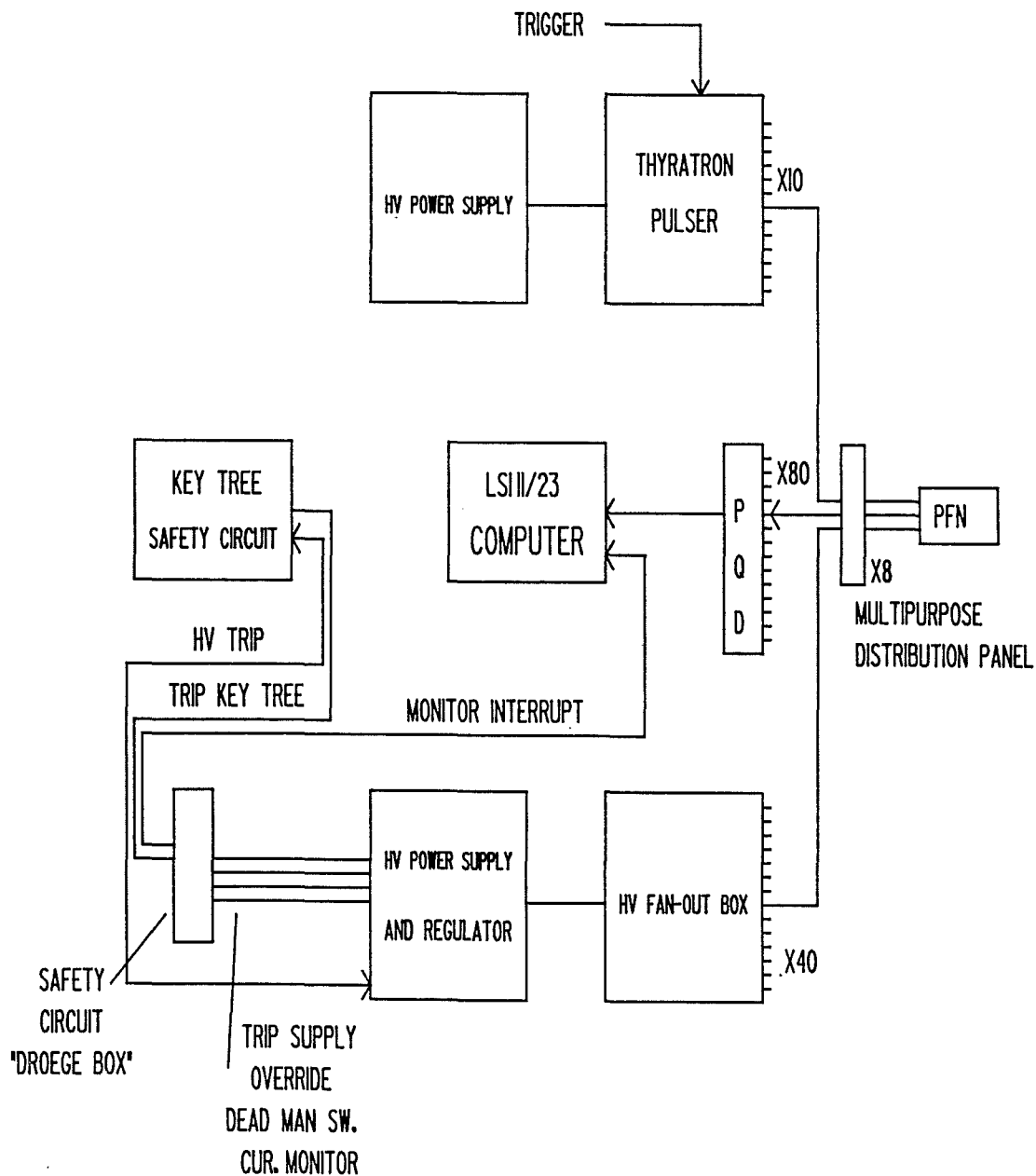


Figure 3.9. Schematic of High Voltage System

Safety circuits, "Droege Boxes" were installed to monitor the total current in the ground return of the main power supplies. The Droege Box trips the main power supply and the Key Tree safety circuit when the current exceeds preset limits (typically 2 mA). After a trigger has caused the PFN's to discharge, a dead time is allowed to accommodate the high recharging current. After this time, typically 4-5 seconds, a current in excess of 2 mA will cause a trip.

Override switches were available. A "dead man" switch provided a high current (10 mA) trip and required the switch to be continuously depressed. Releasing the switch caused a trip. This override satisfied a "two man" safety rule when it was necessary to work near the high voltage. A second override "blanked out" current monitoring for a preset time, typically 20 seconds, to facilitate turning on the HV system.

3.4.2. The High Voltage Regulator. Fluctuations in the ac line voltage, due to the power drain by the accelerator magnets, created a need for better regulation in the HV power supplies. Two silicon controlled rectifier (SCR) based regulators were built and installed in each of the HV supplies. A block diagram of the regulator circuit is shown in Figure 3.10 and consists of a comparator card, phase card, gate card as well as low voltage dc supplies, transformers and SCR's.

Inside of the HV power supplies, the 3 phase 240 VAC line is continuously varied from 0-240 VAC by means of a VARIAC, enters a HV tank where it is transformed and full wave rectified and then emerges as DCHV from 0-15 kV. The regulator was inserted electronically between the VARIAC and the HV tank. Taps were taken off of the input voltage to

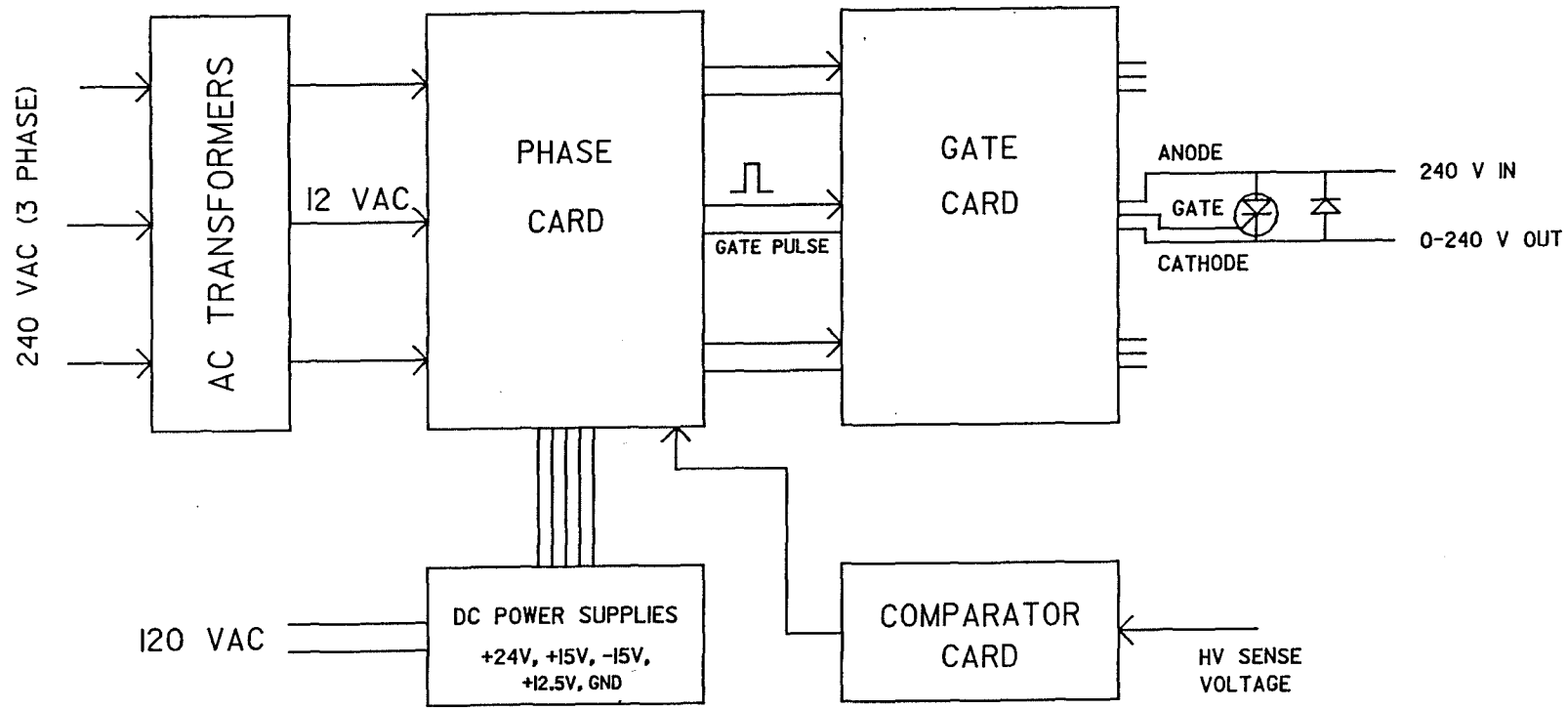


Figure 3.10. Schematic of Regulator Circuit

provide 240 VAC to the transformers and 120 VAC to the low voltage dc supplies.

An SCR behaves like a "triggerable" diode. In the regulator, an SCR will hold a positive voltage between the anode and cathode until the gate receives a pulse. Upon receiving a gate pulse, the SCR triggers and allows current to flow which is proportional to the voltage difference between the anode and cathode. The power diodes, in parallel with each SCR, short out the negative phase (with respect to the anode) of the ac cycle.

In actual operation, the DCHV from the output of the main supply is picked off and voltage divided via a resistor chain and used as input to the comparator card. This low sense voltage (typically ≈ 5 volts) is compared to an internal preset voltage. When the sense voltage is greater than or equal to the reference, the comparator card output is high (off). When the sense voltage is less than the reference voltage, the output is low (on).

It is this change in output states which adjusts the timing of the gate pulse within the ac cycle. The SCR can fire early for maximum current or late for minimum maintenance current. On the phase card, the voltage from the comparator card is seen by the emitter of a transistor. The base of the transistor sees the 12 V, half wave rectified, ac voltage from the transformers. When this base voltage exceeds that of the emitter, the transistor fires, discharging a capacitor. This discharge pulse travels to the gate pulse card where it is shaped, acceptable to the main SCR's.

On the comparator card, the difference voltage between the sense and reference voltages originally had a gain of unity with respect to

the output voltage. The gain was changed to 30, providing faster switching between the high and low output states.

The HV regulator was easy to build and debug. The phase and gate pulse cards were used in accelerator magnet power supplies, the rest was assembled using easily obtainable components. The regulator provides at least a factor of 40 improvement over no regulation. At 9 kV output, a 20% change in the input voltage resulted in a 20% change in the output voltage without regulation and a 0.5% change with regulation. The regulator provided faster recharge times, roughly by a factor of two over no regulation.

3.4.3. High Voltage Pulse Monitoring System. The system, shown in Figure 3.11, has a capacity of monitoring 640 channels and consists of up to 8 special crates of electronics controlled by an LSI 11/23 computer. Each crate contains a crate controller and five data modules. Each data module contains the electronics to monitor 16 PFN's as well as an 8-bit serial shift register readout system.

Upon receiving a trigger, the pulse monitor system (PQD) checks whether the front edges arrive in proper synchronization with the trigger, determines whether there is spurious pulsing and measures the total charge in each pulse.

The front edge arrival time is considered satisfactory if the pulse amplitude exceeds a preset comparator level by the time a preset timing signal is received from the controller. Any channel with a bad front edge is flagged by setting a bit in a storage register.

To check for spuriously firing (run-on) spark gaps, each 16 channel data module contains two, 4-bit "run-on" counters. Each counter is the logical OR of the eight PFN's serviced by a single multi

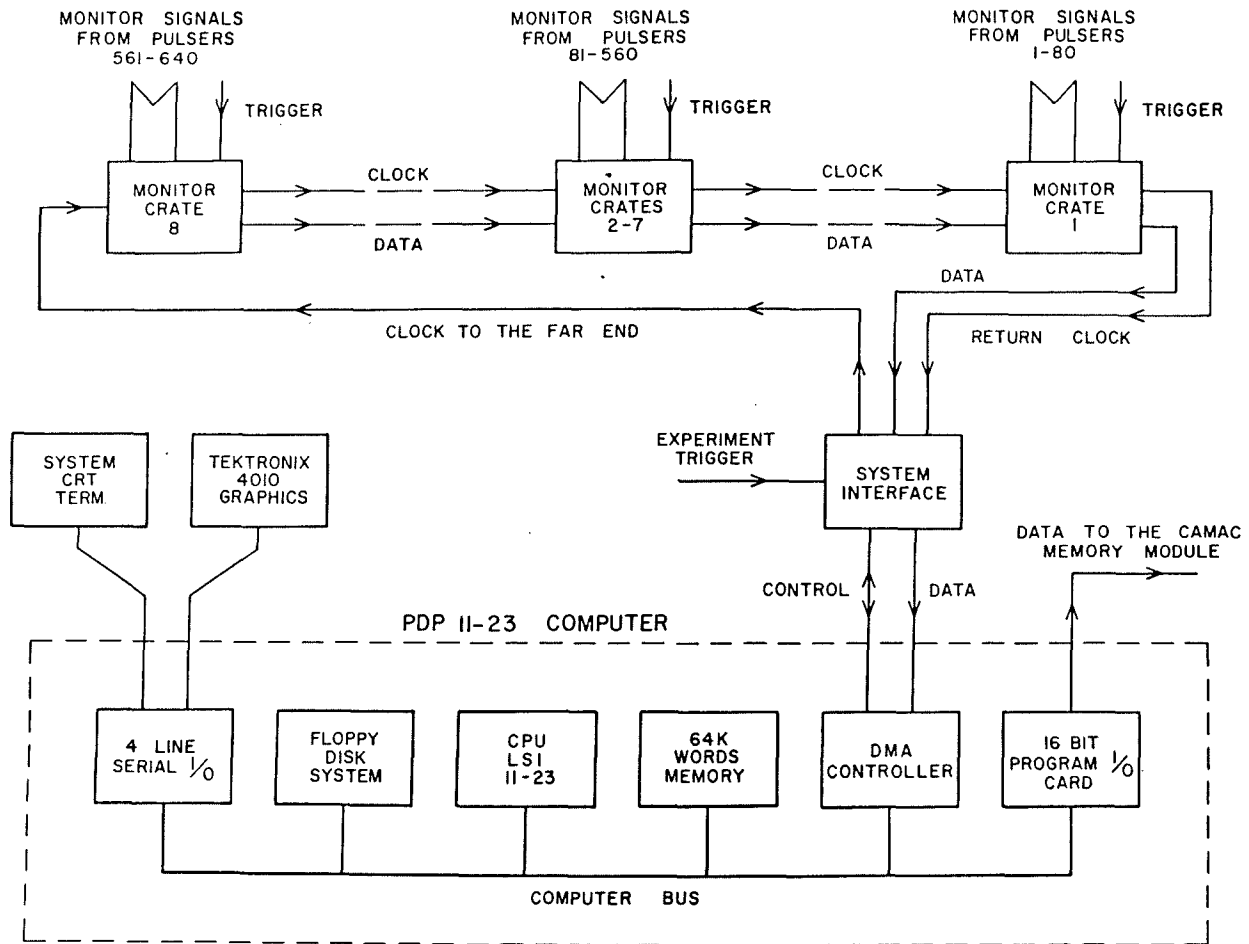


Figure 3.11. High Voltage Pulse Monitoring System (PQD)

purpose distribution panel. The run-on counters contain a count of one if all the PFN's worked properly. In the event of a spurious discharge in any one of the 8 PFN's being monitored, the run-on counter is increased by one.

To measure the total charge of the high voltage pulse, the monitor signal for each channel is integrated with a resistor-capacitor combination and then digitized using an 8-bit analog-to-digital converter (ADC). The voltage across the 16 integrating capacitors is digitized in succession with each conversion taking about 100 μ sec. The capacitors are allowed to discharge throughout this process with a time constant of 50 msec, allowing for complete discharge by the time of the next trigger. No dispersion in the measured pulse-heights is introduced by the capacitor discharge since digitization occurs at the same time relative to the monitor pulse.

The information from the three pulse analysis sections is read into the computer by a single shift register bit serial path connecting all the modules. The details of the data transfer are given elsewhere.⁶⁸ The program used for data acquisition and display is an RT-11 version of MULTI⁶⁹ with special data handlers to accommodate our hardware configuration. Once all the data has been read in, it is written into a CAMAC memory module in the data acquisition system of the main computer and combined with the rest of the event's data and written onto magnetic tape. The monitor computer then unpacks the data, displays it via standard MULTI commands and statistically analyzes the data for an end of run summary. Poor PFN performance can be easily determined either on an event-by-event basis or from the end of run summary. PFN maintenance is then performed based upon the information.

3.5. PROPORTIONAL TUBE PLANES

3.5.1 Construction. The proportional tube planes provided the trigger for the experiment as well as provide energy measurement at higher energies (above ≈ 100 GeV). The calorimeter contained 25 planes for the WBB (36 for the NBB), with each plane containing 144 cells. The planes were made of extruded Aluminum. Each cell measures 1" X 1" X 12' and is strung with a 50 micron diameter Gold-plated Tungsten wire. Four cells are connected to one amplifier to reduce the cost of the electronics while still maintaining adequate granularity for triggering purposes. An Argon-Methane (90%-10%) gas mixture is used to give the fast drift time (≤ 200 nsec at 1650 volts) needed to form the trigger within the flash chamber sensitive time. The planes are calibrated using Cd^{109} sources which are mounted on the planes.

3.5.2. Trigger Electronics. The amplifiers are charge-integrating with a rise time of 180 nsec. The gain is 1 mV/fC within $\approx 2\%$. The calibration, gain, and operation is discussed elsewhere.⁷⁰ The four cell wires were capacitively coupled in parallel to the amplifier input. The amplified output signal passed through a 600 nsec delay line. This delay line was tapped at 250 nsec and subtracted from the undelayed signal. This differential pulse, called FAST-OUT, was sent to other electronic boards in the planes. These boards are the Sum and Multiplex Board (SMB), the Electron Logic Board (ELB) and an Interface Card (IFC). Two signals labeled B (Before) and A (After) were generated to sample and hold, on capacitors, the delayed amplifier output voltage. In normal operation, the delay between B and A was set to 400 nsec. The SLOW-OUT pulse height was the difference of the capacitor voltages,

$$\text{PH} = V_A - V_B.$$

Each of the 36 FAST-OUT signals were terminated into a comparator on the ELB. The comparators discriminated at programmable threshold levels. These levels were externally adjustable in 5 mV increments, from 5 to 128 mV. The comparator output was logically TRUE whenever the input voltage exceeds the threshold. The logical state of each comparator was stored in a latch, called HITBIT.

The comparator outputs were processed further by the ELB. Three fast signals were constructed which contained information about the pattern of energy deposition in the plane:

- 1) Single (S), the logical OR of the 36 comparator outputs.
- 2) Analog Signal (A), the multiplicity of comparators above threshold in units of 50 mV per channel ON.
- 3) Fat Shower Veto (FSV), indicated that the shower width was greater than a preset span of amplifier channels.

The ELB operated in either of two modes, EVENT or CALIBRATION. In each mode comparator thresholds were automatically adjusted. In EVENT mode, the ELB responded to an external trigger, in CALIBRATION, an internal trigger. At the end of each trigger cycle, a RESET cleared the HITBITS and reenabled the circuits.

The SMB performed four functions. First the 36 FAST-OUT pulses were summed to create an analog signal, SUMOUT, which corresponded to the total energy deposited in the plane. Second, the A and B switching signals were made when a trigger was received and sent to the amplifiers. Third, the trigger and RESET signals were sent to the ELB. Finally, the 36 SLOW-OUT pulse heights and the 36 HITBIT latches were multiplexed through the SMB for digitization.

During EVENT mode, the FSV, the discriminated SUMOUT and the Analog Signals are gated into CAMAC latches. The discriminated SUMOUT rates

were stored in CAMAC scalars. All information was read out by the computer and added to the event record on tape.

3.5.3. Trigger Logic. Since many processes deposit energy in the detector, it is necessary to develop a trigger which can discriminate the interesting processes from the uninteresting (Cosmic Rays, beam muons, noise). Even within the interesting interactions, it is desirable to determine whether the energy being deposited is from final state electrons, muons or hadrons, especially when searching for rare processes.

In forming a trigger, some constraints are imposed by the detectors. The proportional tube response to an ionizing transversal is delayed by the time for electrons to drift to the anode. Full information is typically available 300 nsec after a transversal. Time is needed to develop the SLOW-OUT voltages, but not so much time as to degrade flash chamber efficiency.

A two-stage trigger was developed. First, a pre-trigger gave early indications of activity and second, after a fixed delay for electron drift and signal development, higher level conditions were interrogated. The pre-trigger chosen required a coincidence of any two SUMOUT signals above a common threshold. A new pre-trigger could not be generated until after a fixed delay (1 μ sec), resulting in dead time.

The second level was then checked. Cable lengths from the individual planes were tailored so that the signals from the planes generated by a particle traveling at the speed of light in the direction of the neutrino beam would all arrive simultaneously.

The analog signals were discriminated for use in multiplicity decisions. The A(c) of a plane was ON if at least c channels were above

the ELB comparator threshold. The single plane SUMOUT was ON when the pulse height was above 50 mV (corresponding to <30% efficiency for a single minimum ionizing particle). Each SUMOUT was included in a total energy sum, SUMSUM, which was discriminated at several levels.

Due to saturation of linear summing electronics and minimum voltage threshold of discriminators (30 mV) the SUMOUT pulses were divided resistively into a 90%-10% split. The 90% parts were discriminated at 50 mV and the 10% parts were summed to give SUMSUM.

When any two SUMOUT's were ON in coincidence (600 nsec window) the pre-trigger, M condition (WAIT), was generated and other conditions were tested after the signal development delay. These conditions were:

- 1) $N(n)$ was TRUE when $>n$ SUMOUT's were On.
- 2) $AM(c,p)$, at least p planes satisfied the $A(c)$ condition.
- 3) $FM(w,p)$, ON if, from the FSV conditions, at least p planes had greater-than- w -wide patterns.
- 4) $L(k)$, the length, measured in SUMOUT's above threshold, exceeded a length k .
- 5) From the muon spectrometer, the logical OR of discriminated SUMOUT signals in the FRONT (F) set and BACK (B) set of planes indicated penetration through the toroids.

Specific triggers for various neutrino induced interactions were formed from these signals. Further descriptions will be given when data acquisition is discussed.

3.6. TOROIDS

The toroids consist of three, 24' diameter and four, 12' diameter magnets. The toroids are constructed of 20 cm thick toroidal disks, three disks for the 24' toroids, six disks for the 12' toroids. Inner diameters are 30 cm and 15 cm for the 24' and 12' toroids, respectively.

The magnets are energized by hollow, water cooled copper conductor, and driven into saturation at 800 A by standard beam line power supplies. Low conductivity cooling water circulates through the conductor. Each disk had 3 mm gaps for field measurement. The fields have been measured using a Hall probe, and are reasonably well understood.⁷¹

3.7. ONLINE COMPUTER

The detector was interfaced via CAMAC standard data bus hardware to a PDP 11/45 computer. All on-line data handling was controlled by MULTI, a Fermilab supported software package and was installed under the RSX-11 operating system. Data from the CAMAC bus were stored on disk and written onto magnetic tape each event. The MULTI system then made event information available for diagnostic histogramming and evaluation. The computer automatically performed certain tests, such as rate checks and run-summary calculations, to inform the experimenters of equipment failure and beam status, and to simplify the operation of the detector.

CHAPTER 4. SURVEYING AND ALIGNMENT

4.1. OVERVIEW

The alignment of the flash chambers and proportional tube planes affects the experimental resolutions (vertex, hadronic shower angle and muon track angle), thus understanding and correcting for chamber to chamber variations is important. Muon momentum depends upon the proportional tube planes in the toroid gaps. Our alignment consisted of two parts: (1) a physical survey of selected flash chambers, toroids, and toroid proportional planes and (2) software track fitting. The survey endeavored to provide direct measurement of the chamber to chamber variations as well as provide an external coordinate system for the flash chambers, proportional tube planes and toroids.

4.2. SURVEYING

An external coordinate system was used and was based upon the direction of the NØ beamline, distance from the target in the NØ line and absolute elevation above sea level. During the surveying, I assisted a pair of on-site, professional surveyors.

The flash chambers measure a coordinate along the direction of the wand. X chambers measure the vertical coordinate, the U and Y can be combined to provide a horizontal coordinate. The origin of the measurement is chosen to be at the pick up coil within an amplifier at one end of the wand (see Figure 4.1). The survey measured groups of six

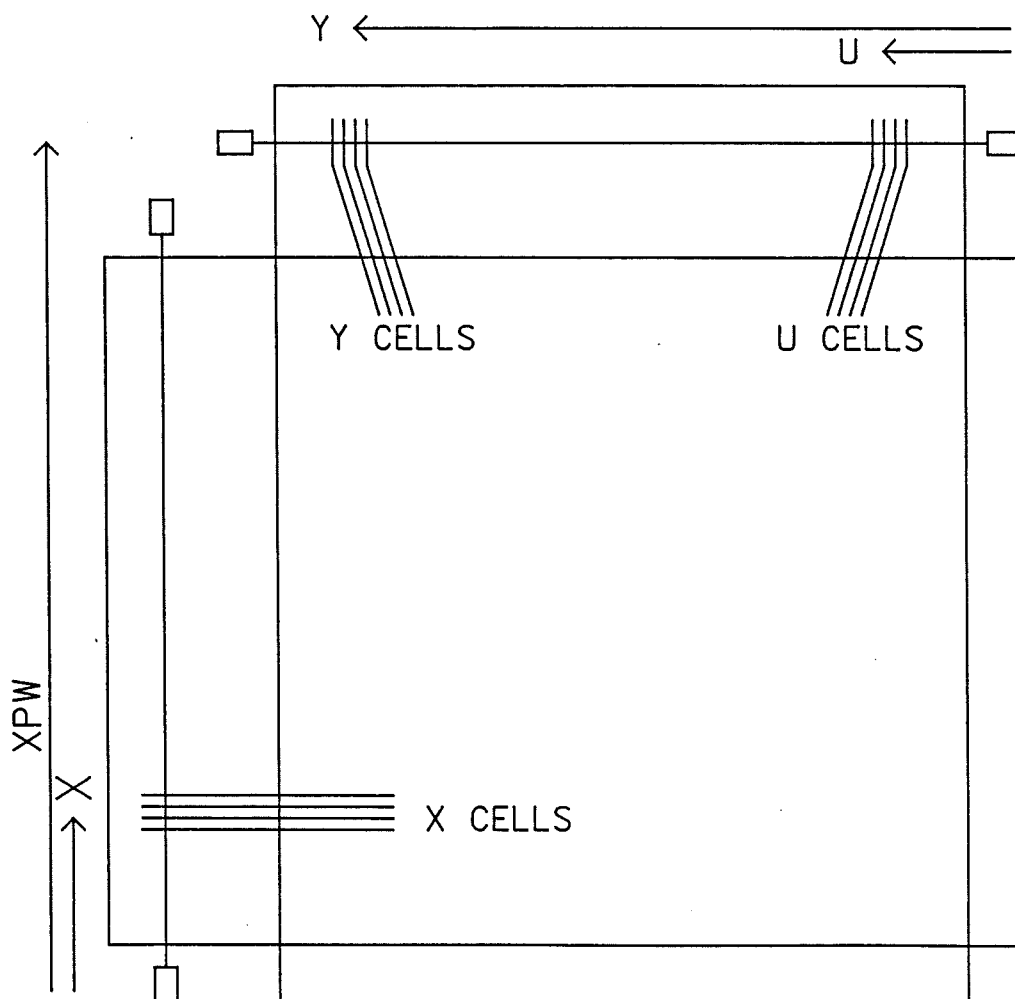


Figure 4.1. Flash Chamber Coordinate System

chambers per group (two of each of the three views), all members of a group within a space of 20-30 cm. The selected groups were spaced uniformly throughout the detector. Measurements in all three spatial coordinates were taken at the "origin" coil and a single coordinate was measured at the opposite end of the wand to determine the angular deviation from vertical (or horizontal) of the wand.

Since the wands were glued to the plastic flash chambers, there existed some variation in the angle between the wand and the chamber cells. Random cells on the surveyed chambers were selected and the angular direction, relative to the external coordinate system was determined. Angles between cells and wand could then be calculated.

The toroid proportional chambers were surveyed. Measurements were made to determine position and angle of the chambers. Since these chambers are rigid structures with fixed wire spacing, it was possible to determine the position and angle of each wire within a given chamber.

Finally, the Iron toroids were surveyed and their center point determined. Relative position of the calorimeter center to the toroid centers could be determined. Measurements showed that the toroid center is roughly a foot lower than the calorimeter center. Since the WBB has only a very small variation with radius, the offset is not a serious problem.

4.3. ALIGNMENT

The software alignment used cell hits in the chambers from straight through muon tracks. The alignment followed a specific procedure to obtain a set of software shifts and rotations for each of the chambers.

The orientation of the three flash chamber views is seen in Figure 4.1. The axes represent the coordinate along the wand by a particular chamber type. The canonical three view relationship is easily seen to be:

$$Y - U = 2 * \text{TAN}10 * (XPW - X)$$

where U, X, and Y are the coordinates measured by each chamber type, TAN10 is the tangent of the half angle between the U and Y chambers, and XPW is the X position of the U and Y wands.

A shift and rotation of a given chamber represents the two degrees of freedom allowed for the fitting. A shift is a change along the axis measured by the chamber and a rotation is an angular change of the chamber about a perpendicular axis. The axis of rotation is arbitrary, but by choosing the axis at beam center, the rotation corrections will be small and the shift corrections alone will be sufficient for most of the hits.

A least squares fit is applied to tracks in each of the three views separately. Single view shifts and rotations are found by examining the deviations between observed and predicted sparks and then minimizing these deviations.

In order to obtain three view shifts and rotations, two views were used to predict the hit position in the third view, deviations are examined and then minimized. Three view corrections are not absolute, so the survey information is used to estimate the corrections needed for each chamber. A final pass through the data is made to determine any remaining shifts and rotations. The residual deviations are shown in Figure 4.2 the single view and in Figure 4.3 for the three view fit.

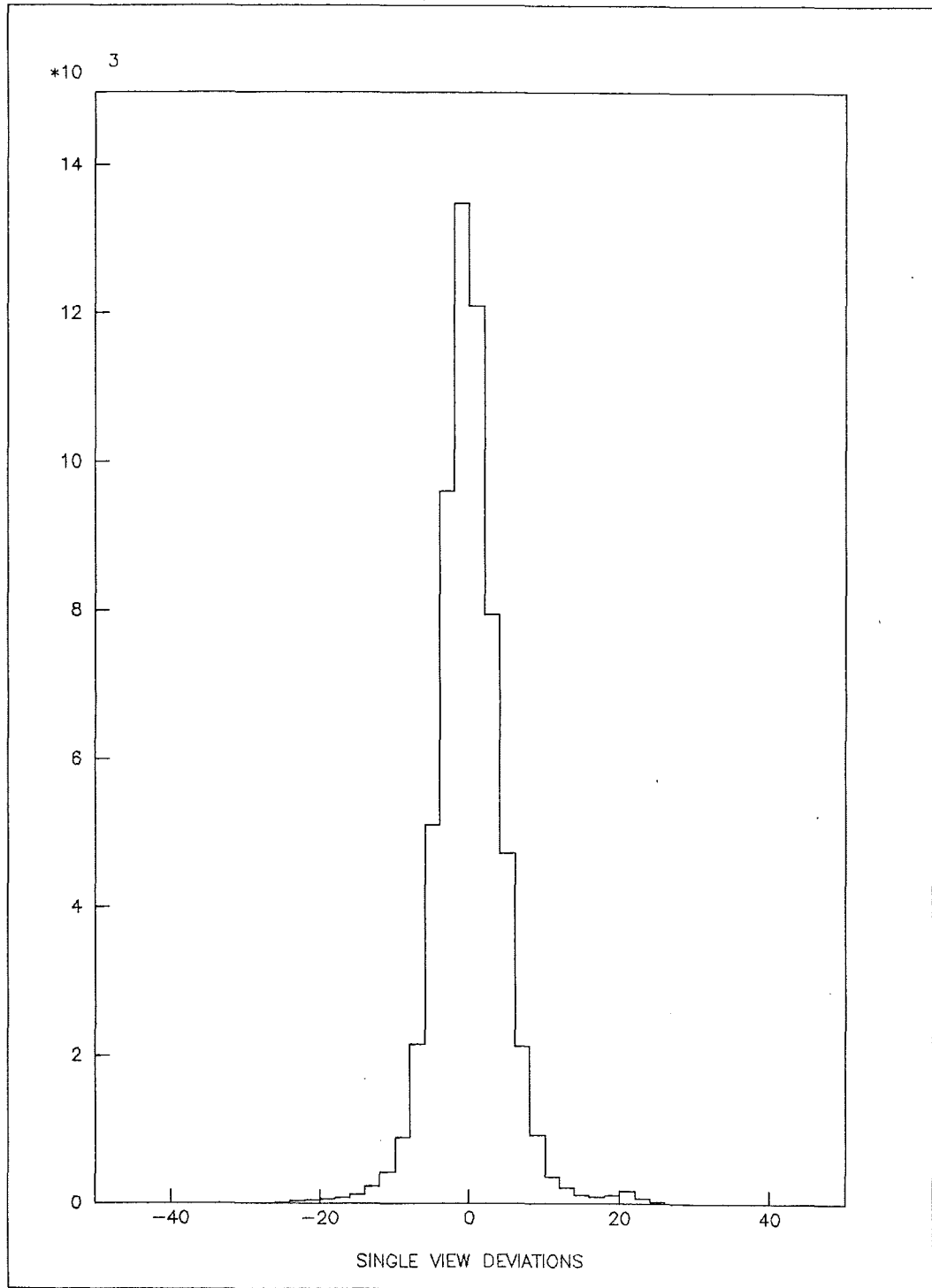


Figure 4.2. Single View Deviations (in clock counts)

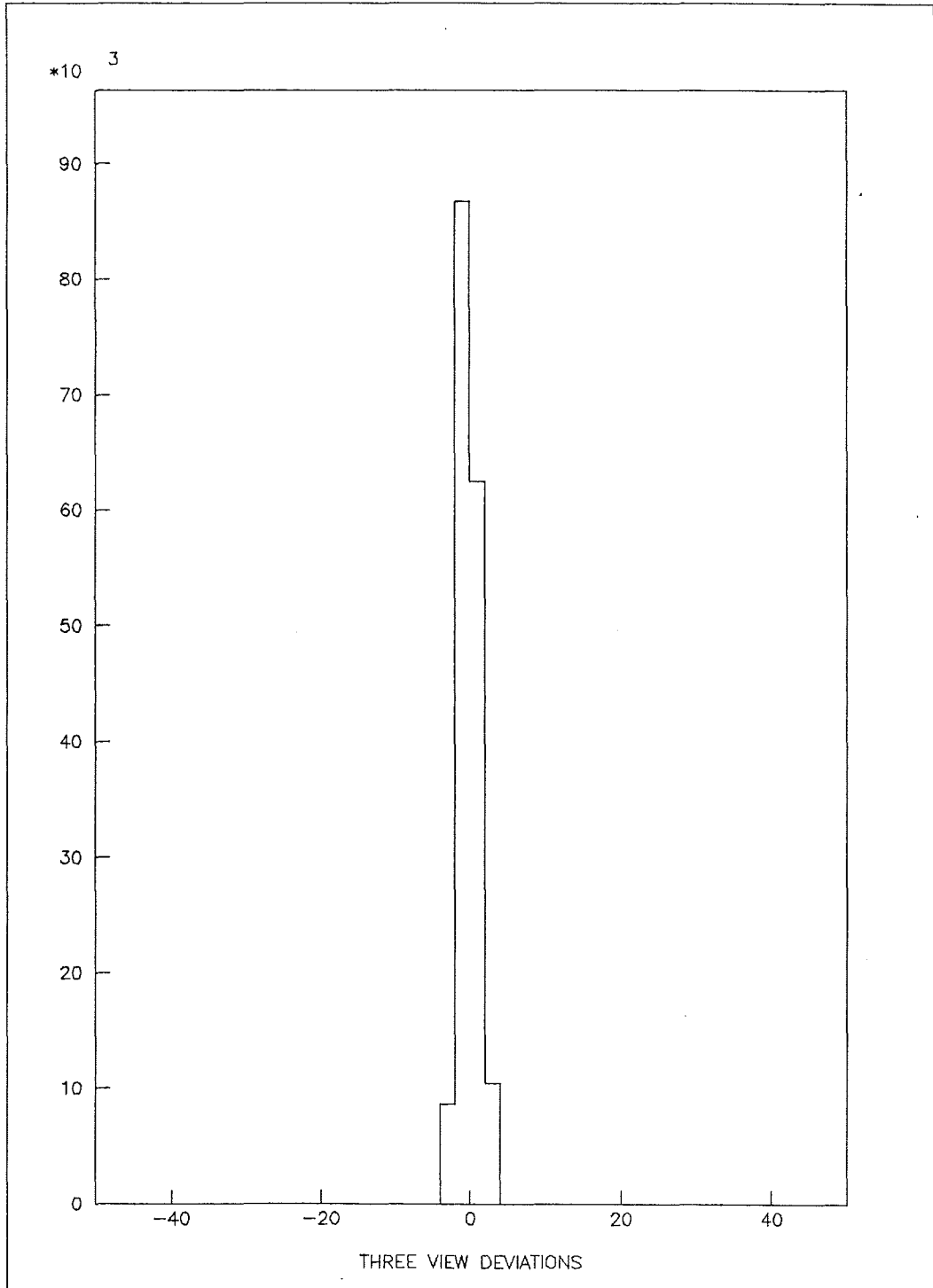


Figure 4.3. Three View Deviations (in clock counts)

This alignment procedure makes shifts both internally (within the flash chambers) and externally (in relation to other elements of the detector) consistent, but the rotations are only internally consistent. Survey information was used to determine an overall rotation (≈ 2 mrad) of the detector.

CHAPTER 5. CALIBRATION

5.1. BEAM LINE

A calibration run for the detector was done June 1980. Hadrons, electrons and muons were transported through the Fermilab N5' beamline⁷² to the detector. The beamline is shown in Figure 5.1. Particles with energies from 5 to 125 GeV were transported. Beam momentum was selected by two sets of bending magnets. The momentum resolution of the beam was known to be $dP/P \approx 0.5-1.0\%$.⁷³ At low energies, it was necessary to retarget the primary proton beam from the main ring to just upstream of the second set of bend magnets. The momenta of the retargeted particles is assumed to be at nominal value, but resolution and central value are uncertain. The beam divergence was measured by hodoscopes and found to be less than 1 mrad.

5.2. THE TRIGGER

The trigger for the run consisted of a hodoscope telescope (H_1 and H_2) and a threshold Cerenkov counter. The hodoscope telescope consisted of two scintillator counters (2" X 3" X 1/16"), one (H_1) set between the Cerenkov counter and the calorimeter, the second (H_2) roughly 25 meters upstream. The Cerenkov counter could be set to trigger on either electrons (low gas pressure) or hadrons (high gas pressure). The trigger demanded a coincidence in both hodoscopes and either coincidence or anti-coincidence in the Cerenkov counter depending upon gas pressure.

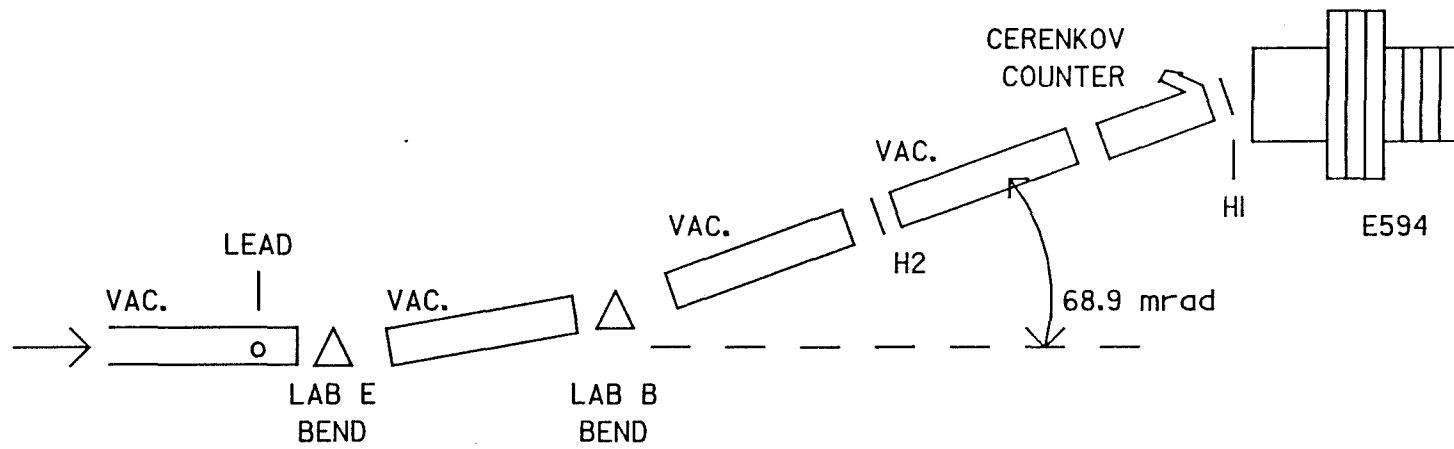


Figure 5.1. Calibration Beam Line

The flash chambers were fired after a fixed delay. This delay was approximately equal to the delay expected from the proportional tube planes. Occasionally an absorber (Lead) was placed in the beamline to filter out the electrons, enhancing the hadron to electron ratio.

5.3. ANGLE RESOLUTIONS

To obtain good angle resolutions, one must take into account (1) the accurate determination of the shower vertex, (2) the best calculation of the shower center of gravity at a given depth and (3) the best use of the centers of gravity as a function of shower depth taking into account statistical shower fluctuations.

The lateral position of a shower or muon track at a given depth is determined by calculating a center of gravity of hit cells within a given flash chamber. A least squares fit is made to these centers of gravity. This fit determines the angle of energy flow. Shower vertex is determined by using the incident particle track before interaction (in the case of electrons) or by using pattern recognition algorithms (for hadrons). The pattern recognition algorithms are the same as was used to determine the vertex of neutrino induced interactions.

The center of gravity for a given flash chamber plane is determined by calculating a weighted mean of the coordinates of the hit cells. The weighting depends directly upon the deviation from the estimated shower direction, and upon the inverse one half power of the number of hit cells within the chamber. As a consequence, the beginning of a shower is weighted more. At the end of a shower, fluctuations controlling the deviation from the estimated shower direction increase with increasing

shower depth. The length of a shower is somewhat arbitrary, but a length was chosen which contained 80% of the total number of hit cells.

Muon angle resolutions are shown in Figure 5.2. The resolution values are the rms deviation of a Gaussian fit to the distribution of computed shower angles. Separate data is shown for resolutions in the X chambers, and for the view orthogonal to the X view, which is determined by combining U and Y data. The solid curve is a theoretical prediction⁷⁴ which takes into account multiple scattering and the finite cell size.

Electron angle resolutions are shown in Figure 5.3 and the hadron angle resolutions in Figure 5.4. Again, the resolutions plotted represent the rms deviation of a Gaussian fit to the data. A functional fit to the data yields

$$\sigma(\theta_e) = 3.5 + (52.5 / E_e) \quad (\text{mrad})$$

for electrons, and

$$\sigma(\theta_h) = 6.0 + (640.0 / E_h) \quad (\text{mrad})$$

for hadrons. For comparison, angle resolutions from the CHARM collaboration at CERN are shown. Our angle resolutions are better due to the finer granularity of the flash chambers.

5.4. ENERGY RESOLUTIONS

The energy of a shower can be measured by counting the total number of hit flash chamber cells (HITTOT). If all of the energy of a shower were visible, the detector would show a linear response. Unfortunately, the energy response is degraded by the fluctuation of the visible fraction of the total shower energy, the effects of colinear

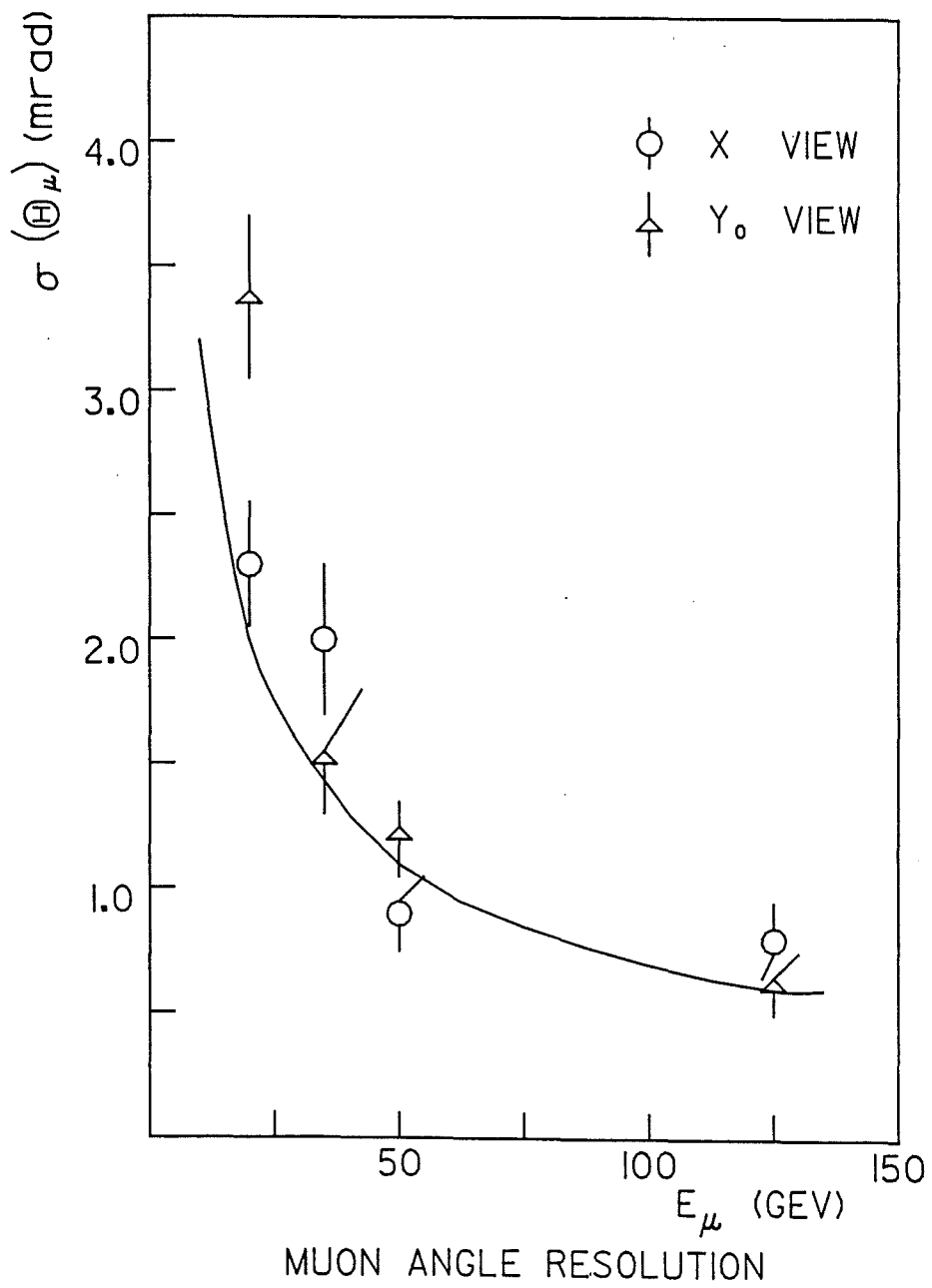


Figure 5.2. Muon Angle Resolution

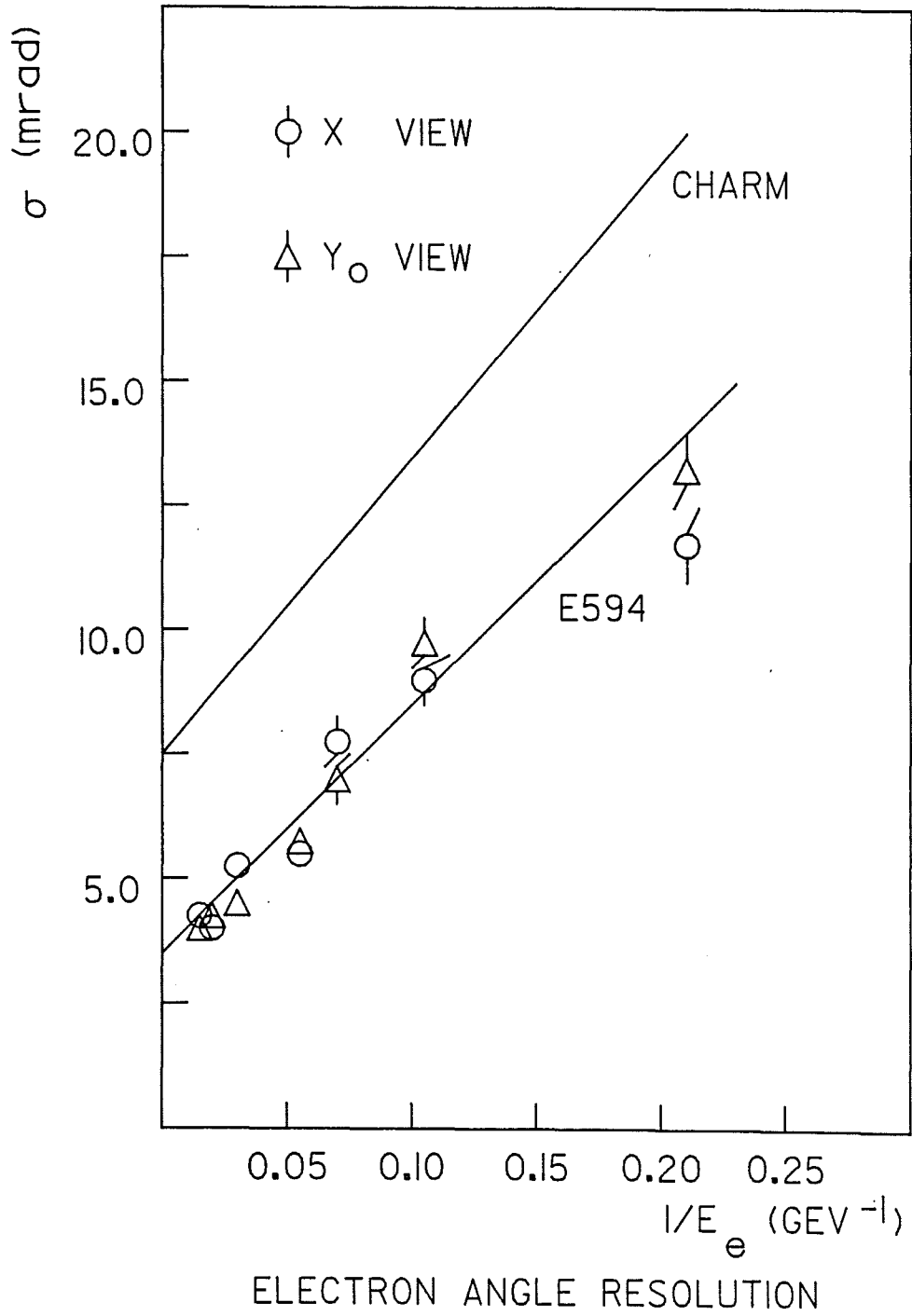


Figure 5.3. Electron Angle Resolution

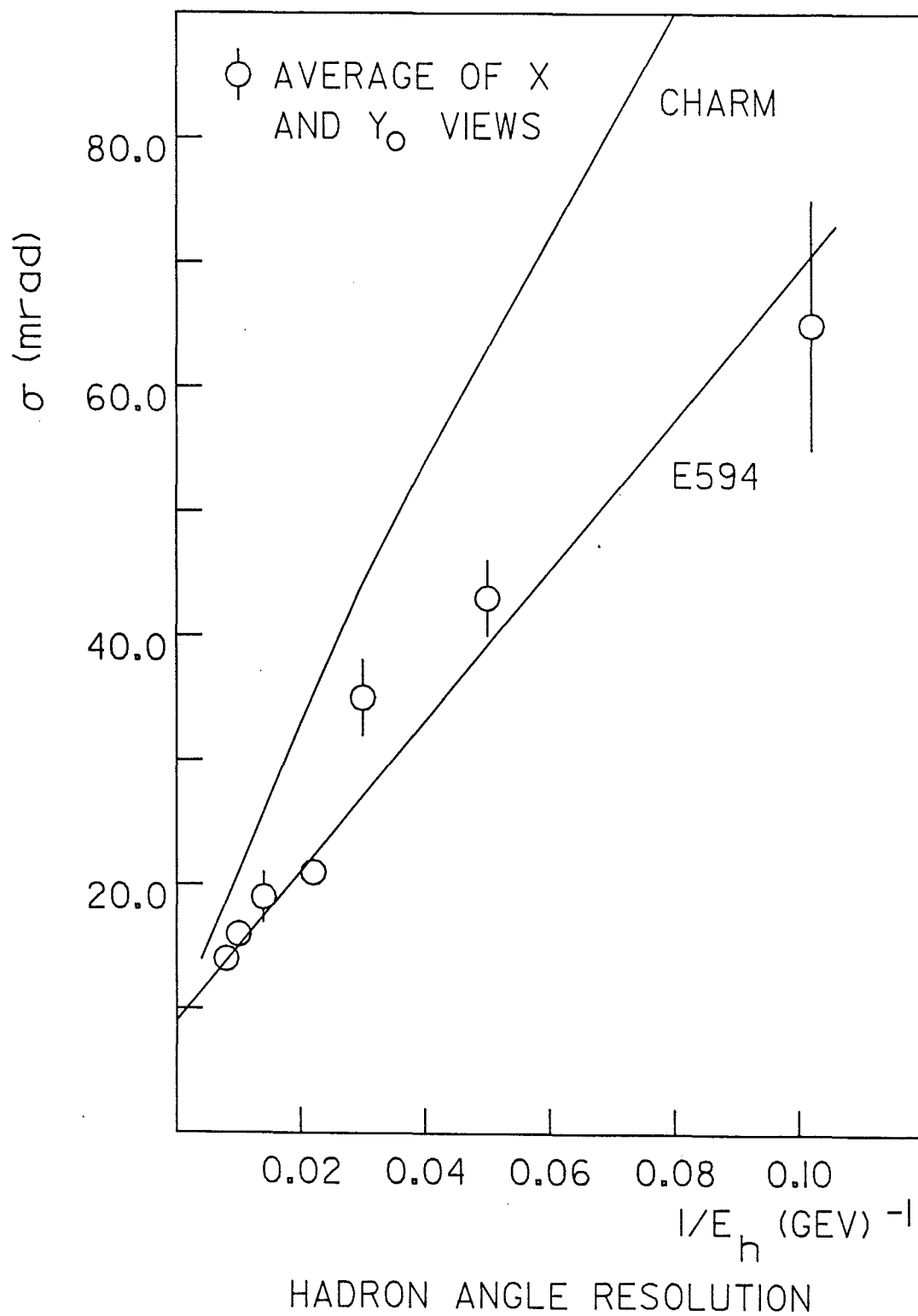


Figure 5.4. Hadron Angle Resolution

electron-positron pairs, and by saturation of the flash chambers in the dense shower core.⁷⁵

The effect of saturation can be partially corrected. Given a local n cell region, with m cells ($m \leq n$) hit, statistical calculations can be made to estimate the number of "effective" particles through the region, and corrections are made to HITTOT. Table 5.1 shows the correction applied for ten cell local regions. No corrections are made for the factor of two arising from the colinear electron-positron pairs. The corrections were optimized for hadron showers in the range of 20 to 125 GeV. The same corrections are applied to electron showers.

The energy calibration and resolution for electrons is shown in Figure 5.5. The local density correction is nearly a factor of two at 75 GeV and improves the energy resolution somewhat. The resolution degrades at higher energies due to unavoidable loss of information which cannot be fully corrected by the local density effect.

The hadron energy calibration and resolution are shown in Figures 5.6 and 5.7. The energy corrections are smaller, due to the lower hit density of hadron showers. The correction greatly improves the resolution, especially at higher energies where a factor of two is gained. A fitted curve to the data yields a hadron energy resolution of

$$\sigma(E_h) / E_h = 80\% / \sqrt{E_h}.$$

Above 125 GeV, where flash chamber saturation begins, better resolution can be achieved by using the proportional tube information. Again, energy resolutions from CHARM are plotted for comparison. The use of scintillation counters yields better energy resolutions than our detector.

Table 5.1. Hit Cell Enhancement for 10 Cell Regions

RAW HITS	CORR. HITS
1.0	1.0
2.0	2.1
3.0	3.4
4.0	4.9
5.0	6.7
6.0	9.0
7.0	12.0
8.0	16.5
9.0	25.4
10.0	42.6

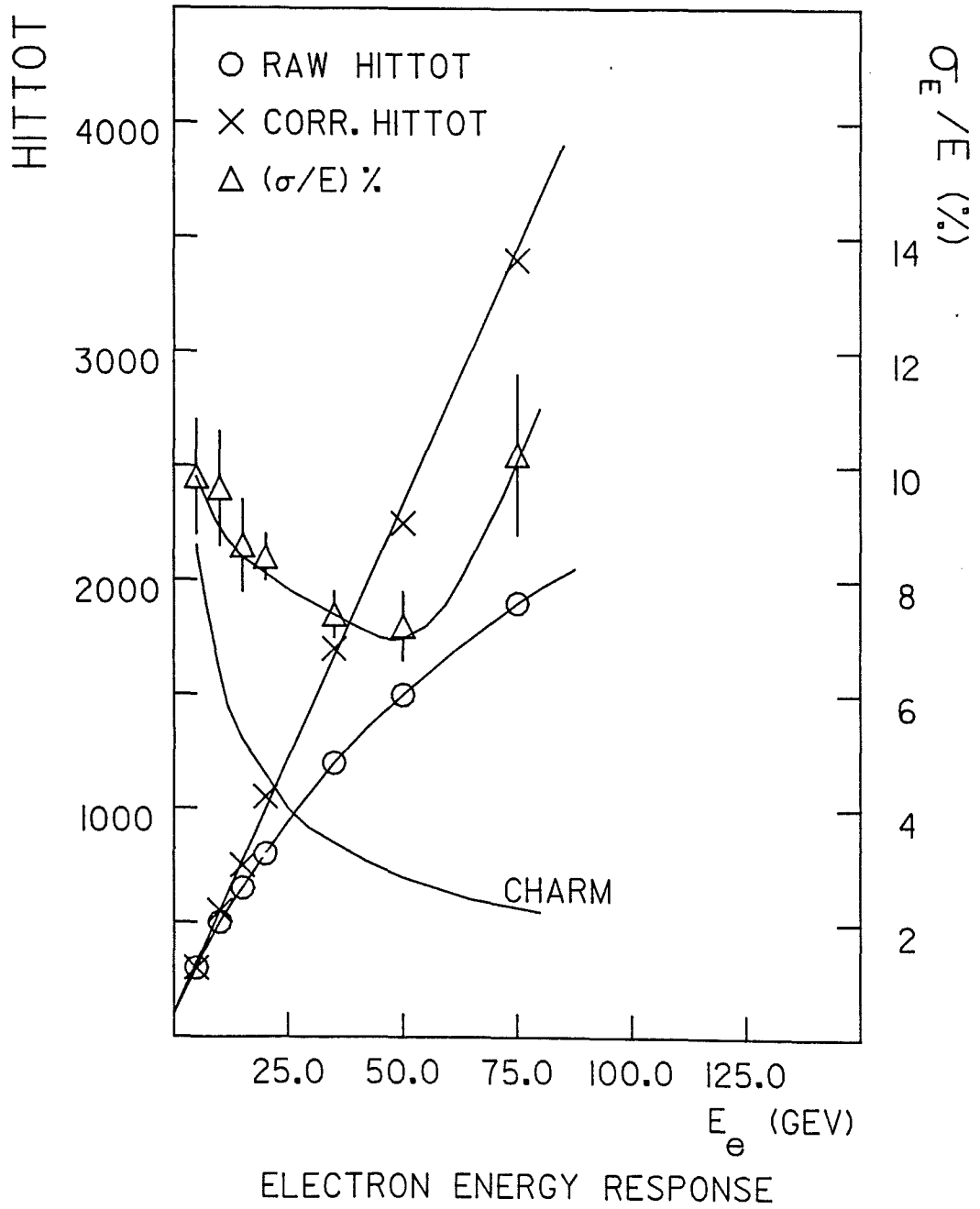


Figure 5.5. Electron Energy Calibration and Resolution

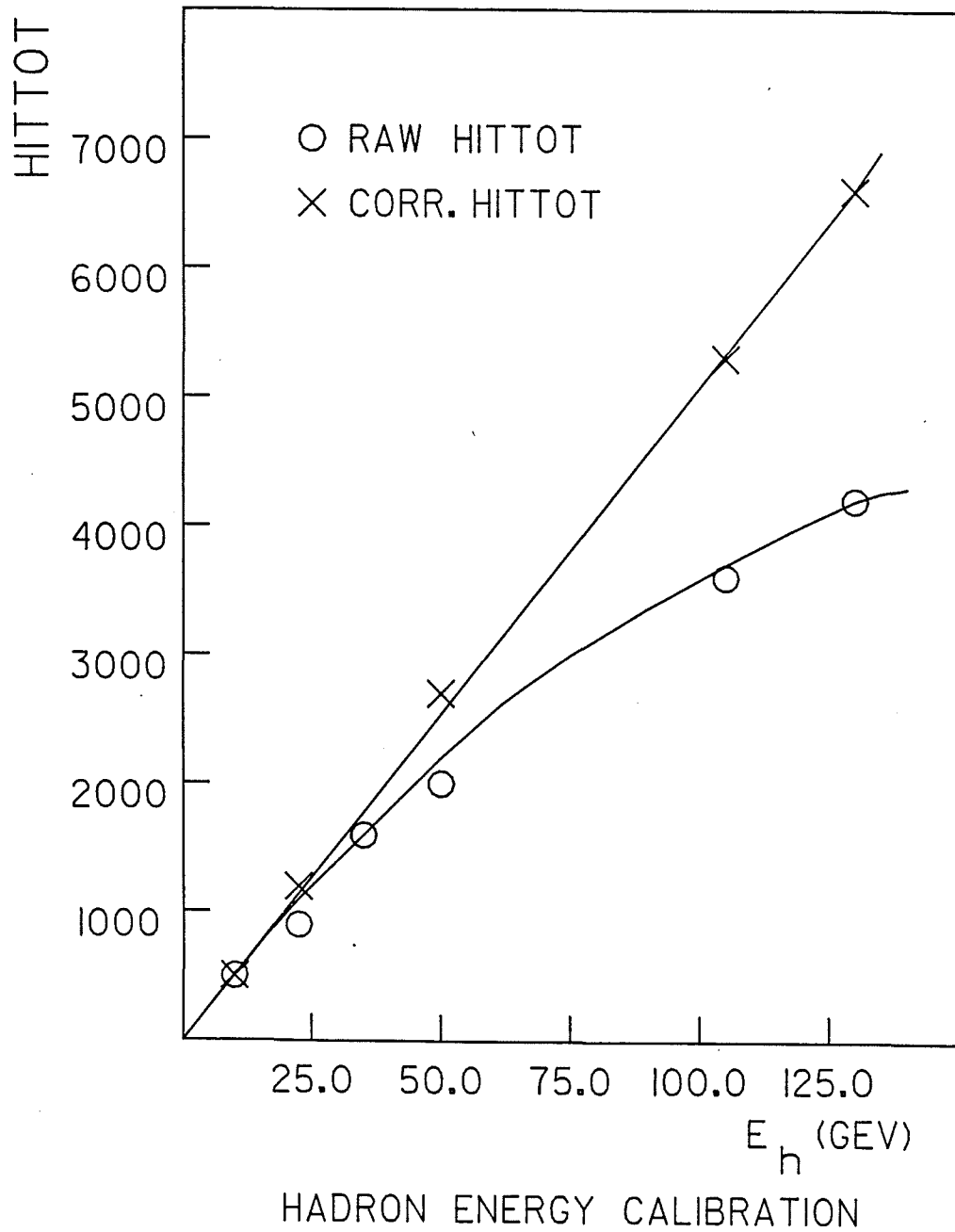


Figure 5.6. Hadron Energy Calibration

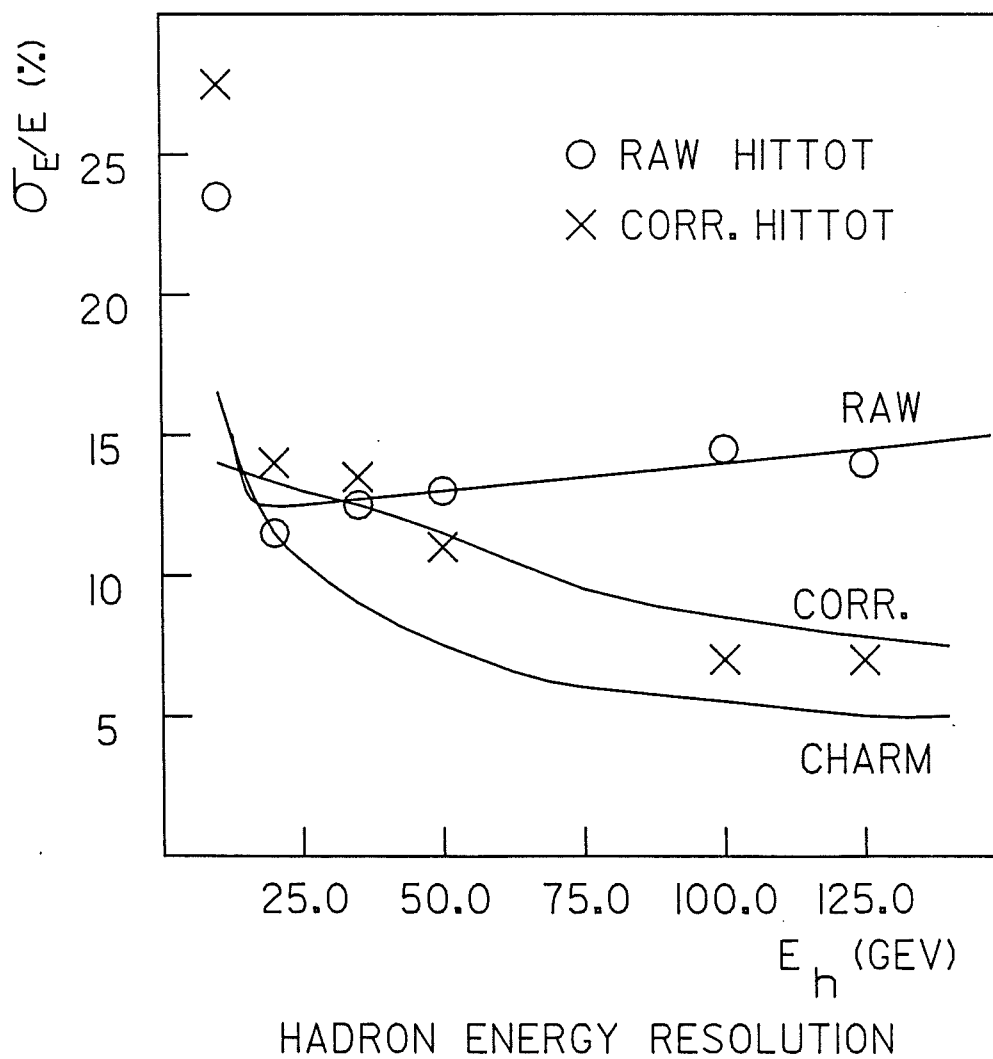


Figure 5.7. Hadron Energy Resolution

CHAPTER 6. THE EXPERIMENT

The 1981 WBB run was intended to be an "Engineering Run" in order to gain an understanding of the detector, develop a trigger(s) and understand the trigger efficiencies. Nonetheless, certain Physics goals were set and achieved. The run was set up for neutrino running, but the last two weeks were devoted to antineutrinos. For the analysis, only the neutrino exposure is discussed.

6.1. BEAMLINER

The neutrino exposure for the February - June 1981 period used a single HORN-focused wide band beam in the Fermilab NØ line. The beamline is shown schematically in Figure 6.1. The primary proton beam of 400 GeV is targeted upon Beryllium. The target was cylindrical in shape, 33 cm long with a radius of 1 cm. The HORN magnet, with a current of 80 kA, sign selects and focuses the secondary particles, mostly pi⁻ and K-mesons. These mesons traverse a decay region, 343 meters long, with decays dominated by 2-body decays, into muons and neutrinos.

The front face of the HORN is located 7.25 meters from the front of the target. It is 2.42 meters long, with a conical section and a cylindrical section. The conical section is 1.95 meters long, front radius of 7.1 cm, back radius of 1 cm. The cylindrical section is 0.47 meters long, radius of 1 cm. The Iron is magnetized by a current

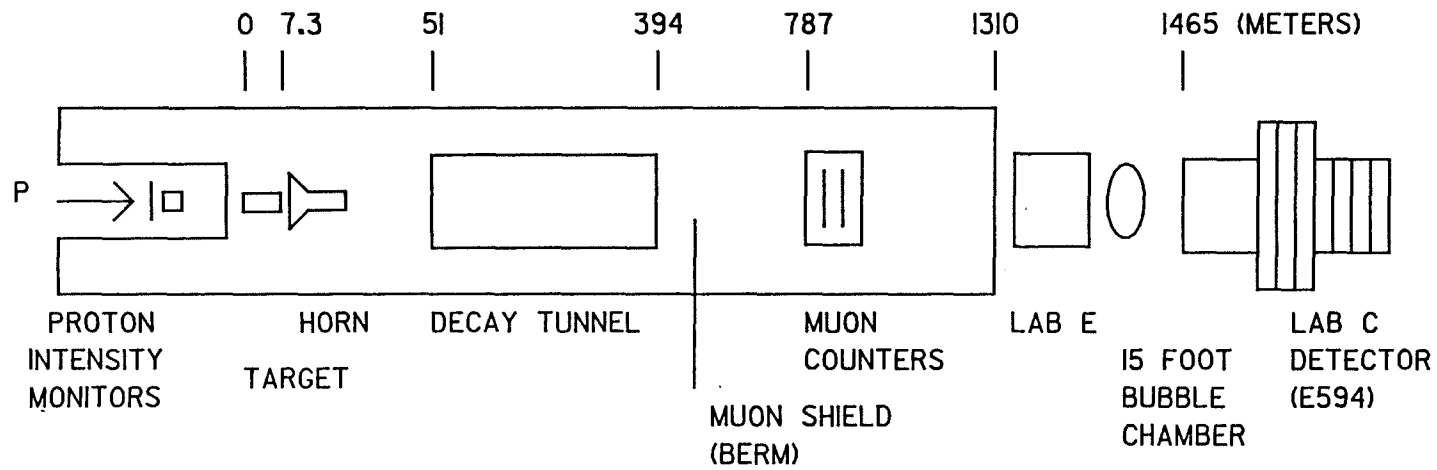


Figure 6.1. NØ Wide Band Beam Line

circulating around the outside surface of the HORN. A complete description of the HORN has been given by Nezzrick and Mori.⁷⁶

An antineutrino flux formed a significant background to the ν WBB, due to meson decays before the HORN and due to incomplete defocusing of wrong sign mesons in the HORN magnet. Three-body decays of charged and neutral kaons account for electron type neutrinos, and occurred at the 1-2% level relative to the ν_{μ} flux.

6.2. MONITORING

Monitoring of the primary proton beam is done before the target. Flux was monitored by a Beam Toroid (BMTOR)⁷⁷ and by a Secondary Emission Monitor (SEM). These devices counted absolute numbers (in units of 10^{10}) and agreed with each other to within 6% during the run. A plastic scintillation counter was placed upstream of LAB C to measure the muon flux through the berm. This counter was located 787 meters from the target and was accessible via a beamline access enclosure. The counter measured 1' X 2' and had a rate of 70-100 counts per beam spill. This muon counter also served to define the experiment's trigger gate, discussed in detail latter. During the run, a second counter was placed behind the first, and run in coincidence with the first. This counter was used to lower accidental coincidences from Cosmic Rays and had roughly half of the area of the first.

Information from the primary proton beam monitors, muon flux counters, and HORN OFF/ON status was received and merged with the event data records on tape. The muon counter information always arrived in time to be included with the current event's data (in-phase). The timing of the proton monitor information was such that it had to be

included with the next event's data record (out-of-phase). While this necessitated a certain amount of software data recombination, no information was lost. From the period 5 April 1981 to the end of the run, ("steady state" running conditions) the timing of the HORN information was fixed and always arrived out-of-phase. Before this time, the timing was uncertain. Information could arrive either in- or out-of-phase, changing on an event-by-event basis.

This is a serious problem. The flux shape and the $\bar{\nu}_\mu/\nu_\mu$ ratio change significantly between HORN ON and HORN OFF conditions. We analyzed the proton and muon monitor information during the "steady state" running. Figures 6.2 and 6.3 show the proton-on-target (POT) and muon counter information for the HORN OFF and HORN ON conditions for this running period. The HORN OFF triggers represent 8.5% of the total (2.3% of total POT). These triggers are clustered at low POT and muon count. (In fact, the HORN was set to remain OFF for low intensity spills.) Cuts on triggers with either less than 0.2×10^{13} POT or less than 20 counts in the muon monitor can eliminate most of the HORN OFF pulses. The HORN OFF triggers remaining represent 3.0% of the total triggers and 2.2% of the total POT flux. Since a large fraction of the data occurs before the "steady state" running, these cuts were used to reduce the uncertainties in flux shape and in the $\bar{\nu}_\mu$ contamination throughout the entire run period.

Very early in the run period, it was discovered that the HORN would go OFF for a low intensity spill and then stay OFF until after a fixed number of high intensity ($\approx 10^{13}$ POT) spills. To counter this condition, we looked at the Charged Current data and noted the μ^+/μ^- ratio as a function of run number (or time). Runs with a μ^+/μ^- ratio in excess of

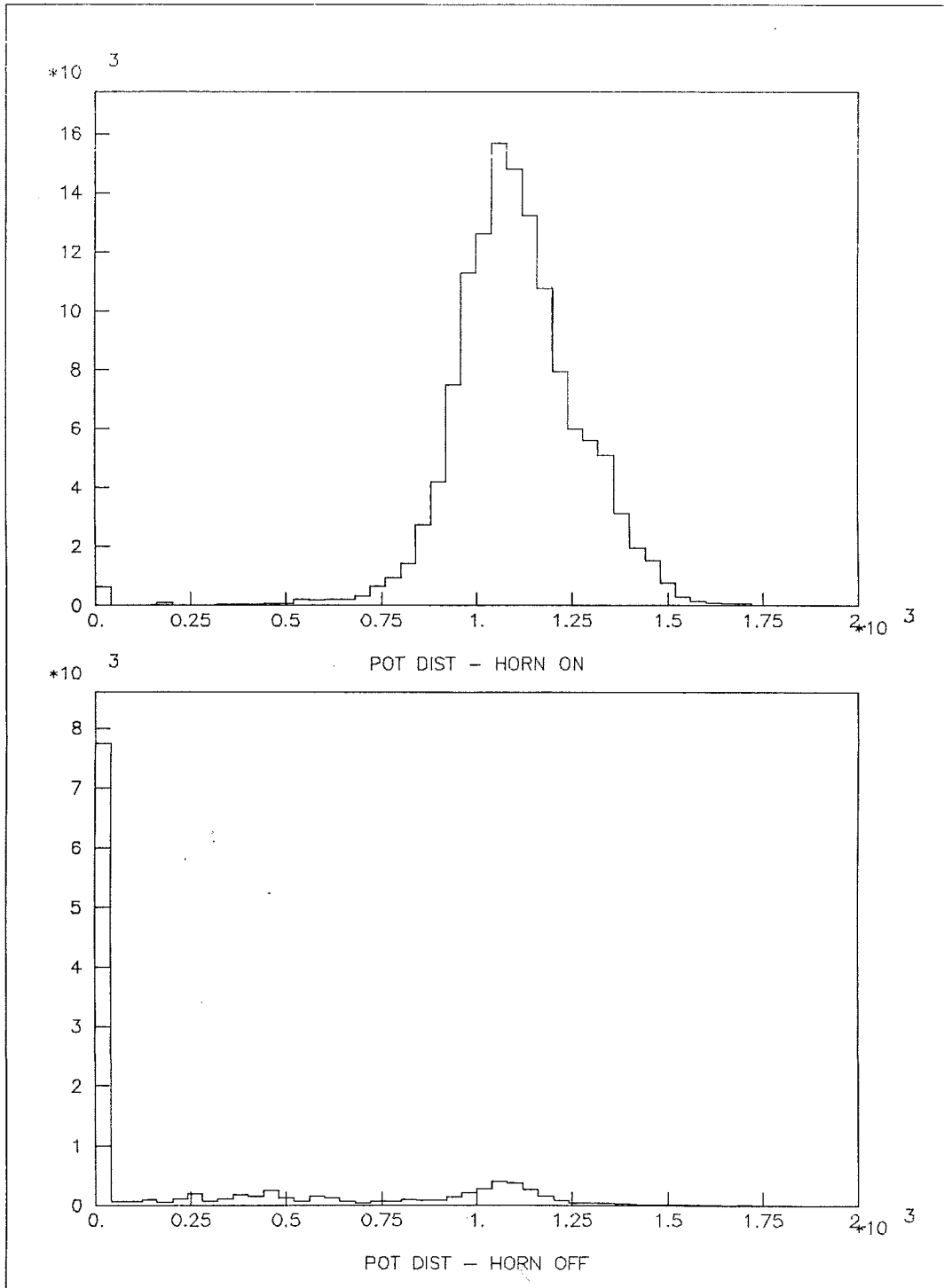


Figure 6.2. POT Distribution for HORN ON/OFF

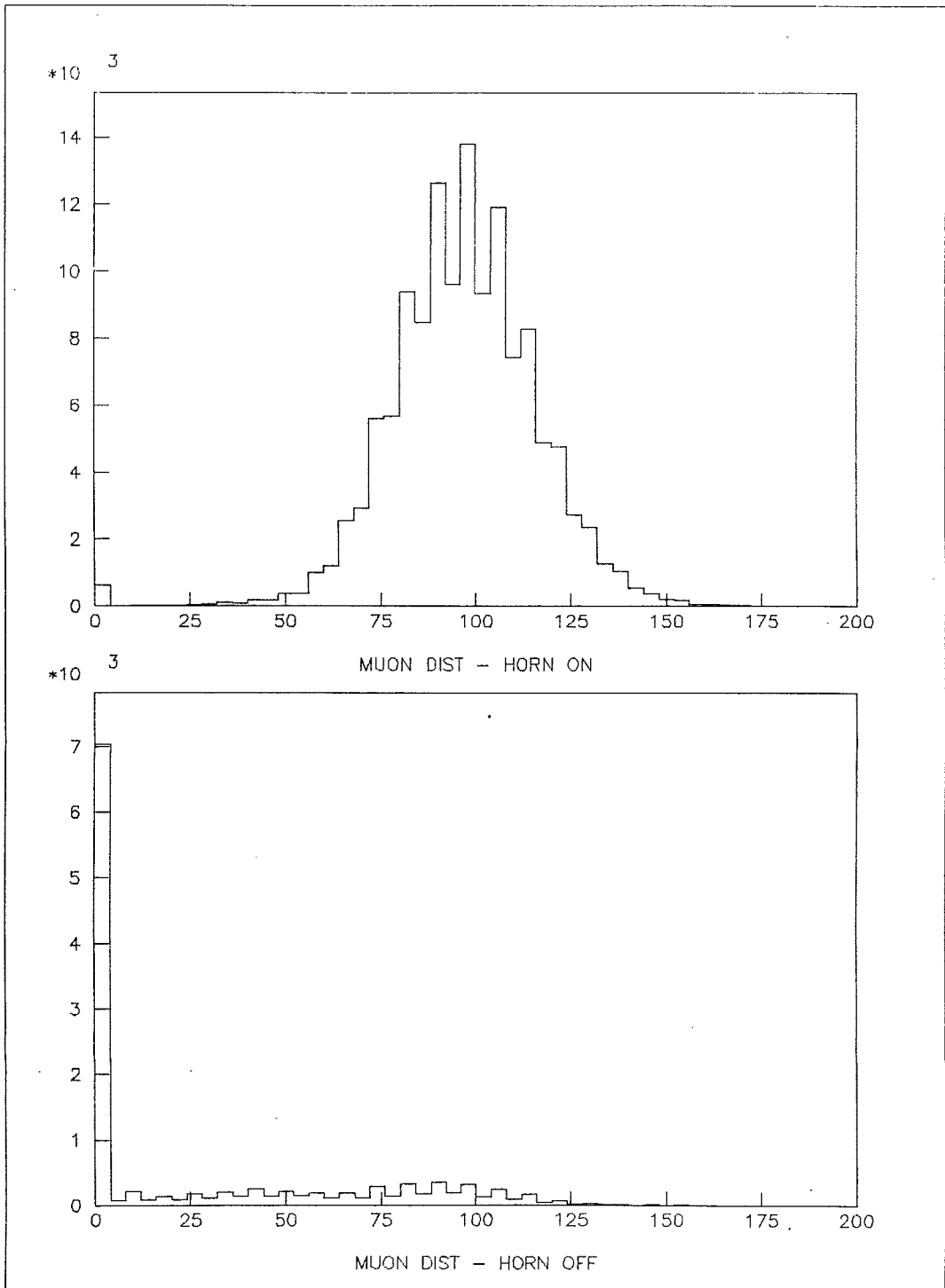


Figure 6.3. Muon Counter Distribution for HORN ON/OFF

roughly 10% were eliminated from the analysis. HORN trigger logic was changed to make an ON/OFF decision every spill after this discovery.

6.3. WBB FLUX

6.3.1. Monte Carlo Simulation. The characteristics of the WBB neutrino flux have been calculated by Monte Carlo. The Monte Carlo had to model both the single-HORN focusing system, and the production spectra and angular distributions of secondary hadrons from protons on a Beryllium target. The Monte Carlo considered production, absorption by the HORN, and two- and three-body decays of π^\pm , K^\pm , and K_L^0 as sources of neutrinos. The Monte Carlo calculated the various spectra as a function of the lateral (from the beam center) position for electron and muon type neutrinos, as well as their antiparticles.

The standard beam Monte Carlo, "NUADA", performed flux calculations for two-body decays. This Monte Carlo contained a model for the HORN. A more sophisticated model was developed by Brock^{7,8} to account for three-body decays, neutral kaon decays, and HORN OFF configurations. Comparisons of the two Monte Carlo methods yield an estimation of the uncertainty in absolute normalization of the integrated, energy-weighted neutrino fluxes to be $\pm 10\%$.^{7,9}

Several production models were used to estimate the production of secondary hadrons. Measurements of pion production from thin films have been parameterized by Wang,^{8,0} while Stefansky and White,^{8,1} and Mori^{8,2} considered the kaon production.

Given these parameterizations, the comparison of the parameterized neutrino spectra and the energy distribution of the Charged Current (CC) events in the detector was poor. More recent particle production

measurements have been made at CERN by Atherton et al.,⁸³ with targets of varying thicknesses. These measurements have been parameterized by Malensek⁸⁴ to predict absolute numbers of each type of secondary meson, by energy and angle, per POT. This new parameterization took into account multiple proton interactions in the target. From calculations, it was possible to fix the absolute ratio of each type of neutrino to the number of POT.

6.3.2. Comparison With Data. The measured CC energy distributions are in good agreement with the predicted shapes. The predicted flux shapes are compared with the momentum distributions of μ^- from quasi elastic data in Figure 6.4. The Charged Current energy spectra for ν and $\bar{\nu}$ are compared with prediction in Figure 6.5.

In all cases, the shapes are in good agreement with Monte Carlo predictions. From the Monte Carlo, the energy weighted fraction of $\bar{\nu}_\mu$ to ν_μ in the WBB is predicted to be $\bar{\nu}_\mu/\nu_\mu = 6\%$. Above 20 GeV in neutrino energy, the antineutrino fraction increases to approximately 7.5%. This is in good agreement with the quasi-elastic muon data where the $\bar{\nu}_\mu/\nu_\mu$ ratio is 8%.⁸⁵

Initially, there appeared to be some discrepancy in the Charged Current data. The antineutrino to neutrino ratio was 6%. This ratio must be corrected for the relative acceptance ($\eta_{\bar{\nu}}/\eta_{\nu} \approx 0.8$) and cross sections ($\sigma_{\bar{\nu}}/\sigma_{\nu} = 0.5$). After corrections, the Charged Current data indicated a 15% contamination, in disagreement with both quasi-elastic data and Monte Carlo prediction.

This discrepancy was eliminated after observation of CC samples for both neutrino and antineutrino events. There is an estimated "cross over" error in the data samples of $\approx 2-4\%$. This error represents the

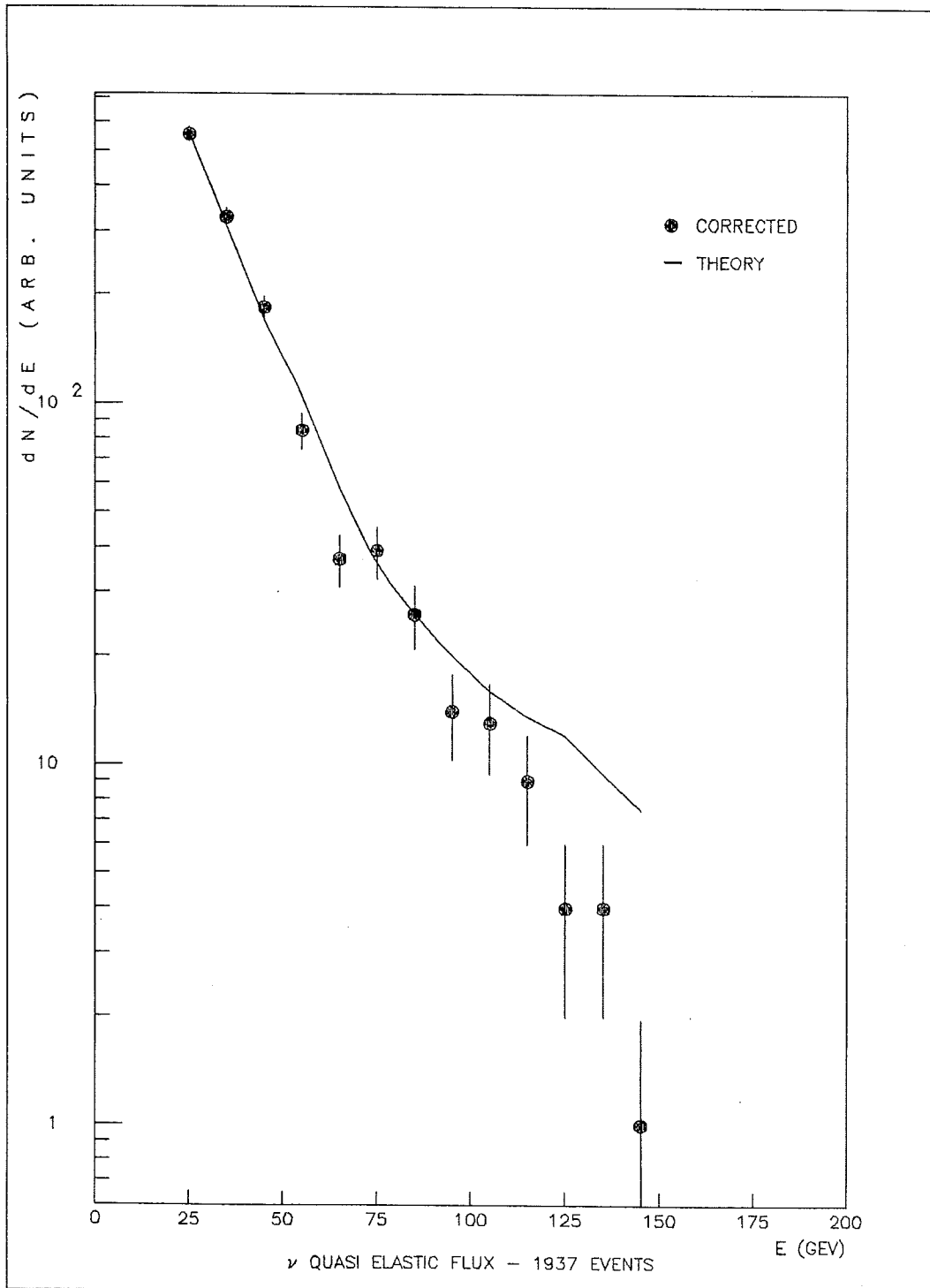


Figure 6.4. Energy Spectrum from Quasi Elastic Data

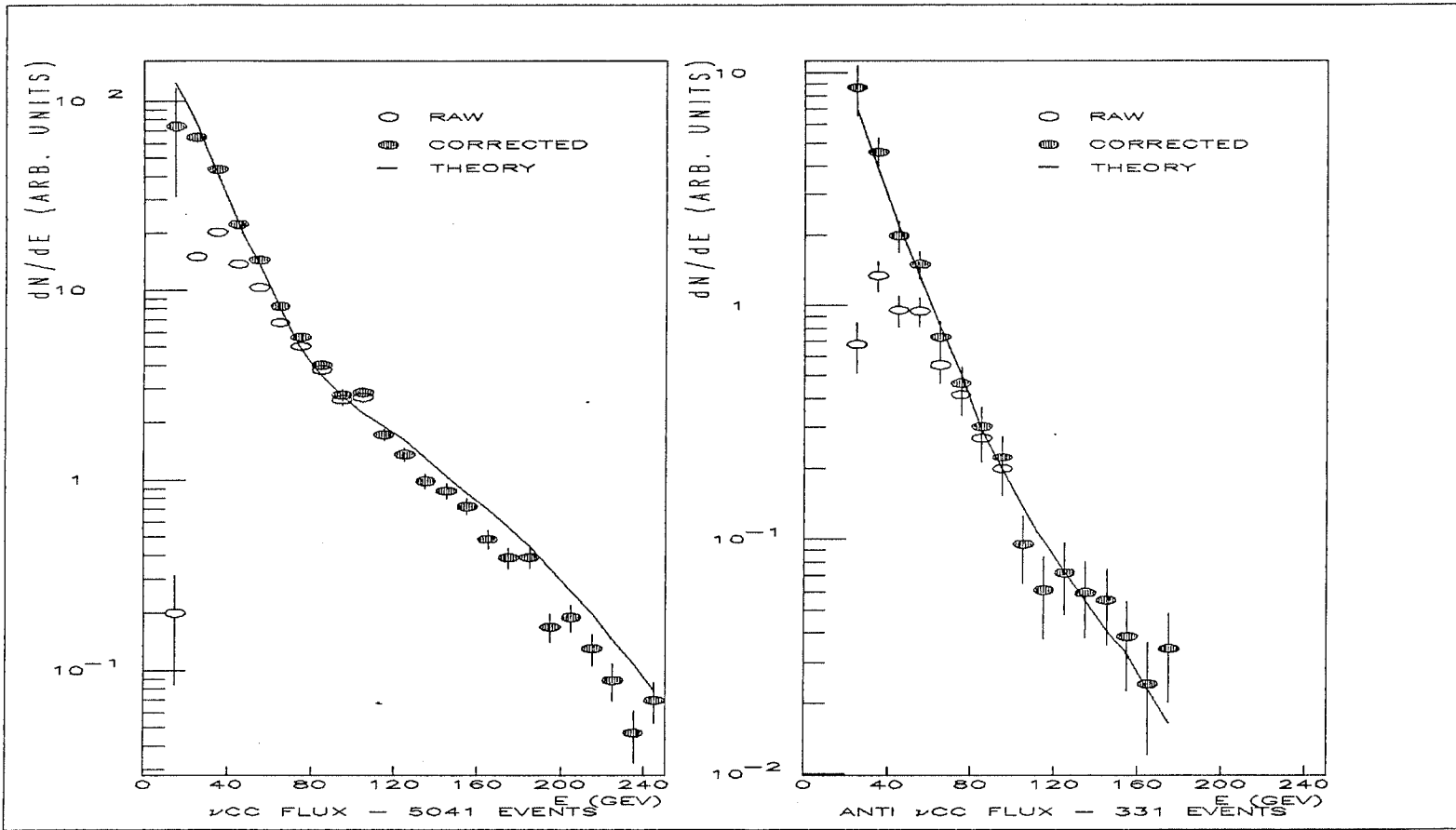


Figure 6.5. Energy Spectra from Charged Current Data

probability that the muon momentum analysis routine does not find the correct "hit" channel in the toroid proportional planes, thus calculating an incorrect sign and momentum. Sources of these incorrect "hits" are: random noise, "beam muons" from upstream neutrino interactions (upstream of the detector), muons associated with meson decays within the hadronic shower, and muons which penetrate the center of the toroids where the field is small and uncertain. Since there are a greater number of neutrino induced CC events, the "cross over" events will have a larger effect on the antineutrino sample. Upon applying a correction for this error, we determine the $\bar{\nu}_\mu/\nu_\mu$ ratio to be in the range of 1.8 to 4.0%, 4.5 to 10% after corrections for acceptance and cross section differences.

6.4. EVENT TRIGGERS

During the first half of the WBB run, the response of many of the trigger components was investigated. The toroid planes and some of the calorimeter planes were either not yet installed or contained non-functional electronics. All detector components were operational during the "steady state" run conditions. The data during the "steady state" period were logged with constant trigger conditions.

Nonetheless, it was possible to take data during the early setup and studies period. A simple "low-bias" (PTH) trigger was set up and used. The trigger consisted of a coincidence between the total energy, SUMSUM, and the delayed pre-trigger, M(WAIT). The SUMSUM was discriminated at 75 mV and the pre-trigger delay was set to 150 nsec:

$$\text{PTH} = \text{M}(150) \cdot \text{SUMSUM}(75).$$

From calibration data, it was determined that this trigger was 90% efficient above 5 GeV, and 100% above 10 GeV. The SUMSUM threshold was set at a compromise between minimum ionizing energies and reducing the accidental trigger rate from Cosmic Rays and Cd^{109} source noise.

Interactions at the end of the calorimeter were not acceptable, so the SUMOUT signals from the last five proportional planes did not contribute to the M condition, but were included in all other trigger components. In the WBB, a proton spill of 10^{13} POT, within 600 μsec , resulted in roughly six PTH triggers per spill. The background from non-neutrino sources contributed to about one PTH trigger. The neutrino intensity was roughly Gaussian within the spill window, the background flat, leading to a non-neutrino trigger fraction of roughly 16%.

The detector was limited to one event trigger per spill. The low-bias PTH trigger gave a high ($\approx 80\%$) dead time, which was unacceptable. In order to be sensitive to rare events such as neutrino-electron scattering, the PTH trigger was set up in a "pre-scaled" mode (PTH P/S). The PTH trigger was counted and allowed to compete after every 25th satisfied trigger condition. After this, the trigger was enabled and could compete with the triggers for the rare interactions.

In particular, triggers for the quasi-elastic (QE) Charged Current process $\nu_{\mu} + n \rightarrow \mu^{-} + p$, and the elastic neutrino-electron (ETRIG) process $\nu_{\mu} + e^{-} \rightarrow \nu_{\mu} + e^{-}$ were developed.

The quasi-elastic event signature was little or no hadronic energy, with muon penetration in the toroid spectrometer. The trigger required coincidence from both sets of toroid proportional planes and energy deposition in the calorimeter below a set maximum threshold:

$$QE = M(150) \cdot F \cdot B \cdot \overline{\text{SUMSUM}(250)}.$$

The rate for this trigger was too high, so it was pre-scaled by a factor of six (QE P/S).

For the electron trigger, differences in topology between electron and hadron showers were exploited. Electron showers are narrower, denser and shorter than hadron showers at fixed energy. Since no electron event could have an associated muon, the Single signals from the last two proportional planes in the calorimeter were used as a veto. A maximum shower length condition of six planes was set up from the SUMOUT signals. Six planes represented roughly 25 radiation lengths.

A width condition was investigated using the FSV component. This component required longer drift time, so WAIT was set to 400 nsec. The FSV was not efficient in rejecting hadrons, since hadron showers were similar to electron showers at the proportional plane sampling frequency. Even though the FSV was not used, the 400 nsec delay was kept since all trigger studies had been performed at this delay. A higher energy threshold and an AM condition were used to reduce background rates. The final trigger was:

$$\text{ETRIG} = M(400) \cdot \text{AM}(1,1) \cdot \text{SUMSUM}(150) \cdot \overline{[S(39) + S(40) + N(6)]}.$$

A special High Energy trigger (PTHIE) was also used. This trigger was identical to the PTH trigger but had a higher threshold:

$$\text{PTHIE} = M(150) \cdot \text{SUMSUM}(1580).$$

This trigger had a threshold of roughly 130 GeV for full efficiency. Since only one out of every 100 PTH triggers satisfied the PTHIE condition, no pre-scaling was necessary.

6.5. GATING

The detector was triggered only during the "fast spill" of the accelerator cycle. The gating scheme is shown in Figure 6.6. The beam spill arrived a pre-determined (PRE-DET) number of accelerator clock cycles after a START signal.

The START signal had a certain amount of jitter on the order of tens of microseconds and tended to drift in time relative to the spill time. To obtain a gating system which would be insensitive to this drift, a dynamic beam gate (DBG) was established. The PRE-DET was used to open a 2 msec gate (BGATE) and a coincidence between the first signal from the upstream muon counters and the BGATE started the DBG. The DBG remained open for roughly 0.6 msec. In order to avoid prematurely starting the DBG from a Cosmic Ray coincidence, the PRE-DET was kept as close to the start of the spill as possible.

Neutrino triggers were enabled during the DBG. If a trigger did not occur within the DBG, a one second gate was opened to allow a Cosmic Ray (M • Liquid Scintillator μ) or a pulser trigger. It was necessary to trigger every spill in order to record beam monitor information. The cosmic ray triggers and pulser triggers were used for alignment studies, and to measure flash chamber refire probabilities, no-event "noise" pedestals, and single-muon efficiencies.

All triggers (PTH P/S, QE P/S, PTHHIE, ETRIG) were enabled during the entire DBG. A gate (20% GATE) was established, which occurred during the last part of the DBG. During this time, the non-pre-scaled "low-bias" PTH trigger was enabled and allowed to compete with the rest. The start of this gate was controlled by the number of hits in the muon counters.

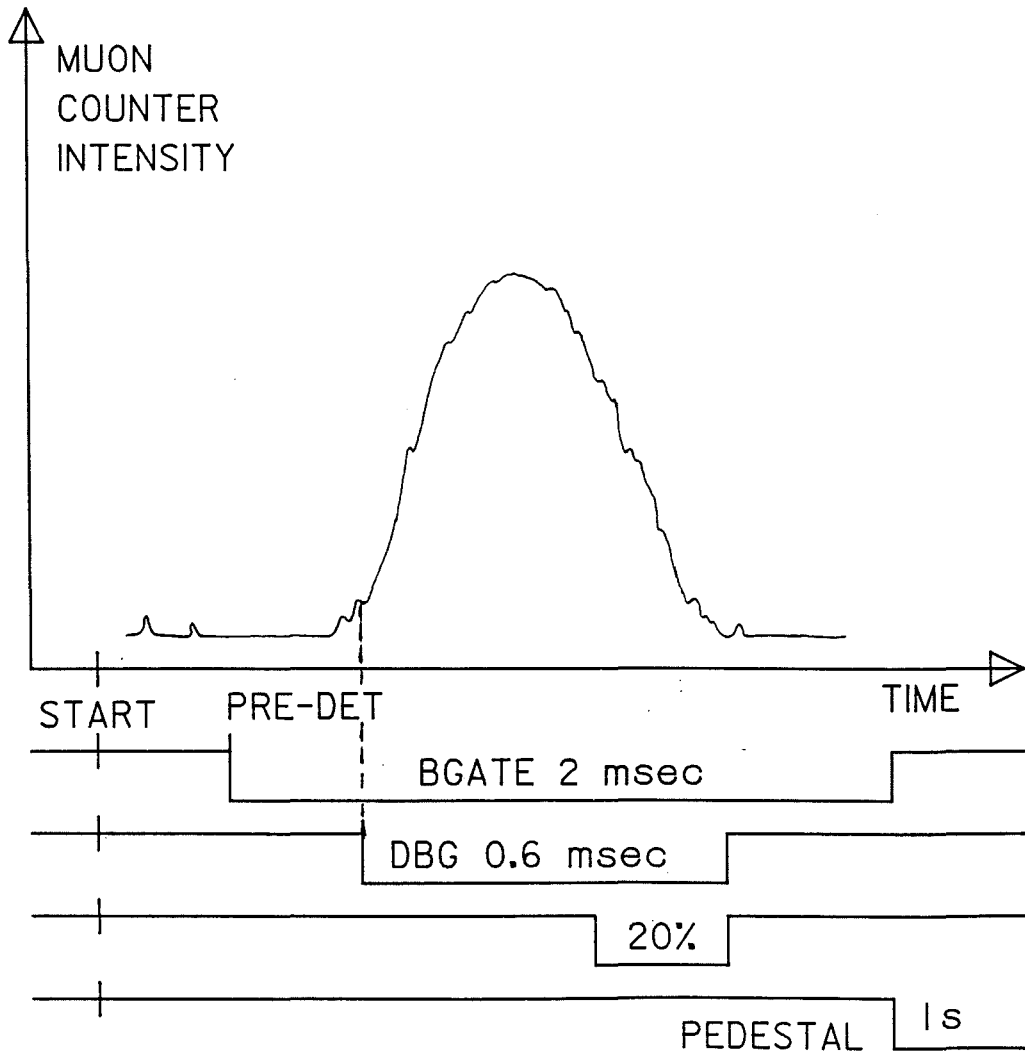


Figure 6.6. Schematic of WBB Gating

It is assumed that the number of muons scales linearly with the proton spill intensity. This is roughly true to within $\pm 15\%$. The average number of hits in the muon counters was 97 ± 18 . The 20% GATE was opened after roughly 80% (70 hits) of the total number of muon hits had been recorded. The 20% GATE ended with the DBG. Measurements of the 20% GATE, during the "steady state" running, indicated it was open during the last 25% of the integrated muon flux.

Once a trigger occurred, the detector was dead for the rest of the beam spill. Scalers recorded the number of muon hits during each of the gates, up until a trigger occurred (i.e. the "live" time). The dead time due to the pre-trigger(s) and due to charged particles traversing the front veto scintillator wall were also scaled in coincidence with the muon scalars. This allowed us to determine the intensity-weighted live fraction on an event-by-event basis. Measurements indicate an average live fraction of $\approx 40\%$ during the WBB run.

Events were recorded in sets called "runs". Each run allowed certain combinations of triggers to be enabled during the DBG and 20% GATE. The type of trigger(s) enabled as well as the type of trigger(s) responsible for a particular event were recorded on tape with each event record. Table 6.1 indicates the various run types, and the trigger types and gating scheme for each run type. Run types for both the setup and steady-state periods are shown.

With an integrated intensity of 3×10^{18} POT during the neutrino running and 0.5×10^{18} POT during the antineutrino running, Table 6.2 shows the number of triggers of each type we recorded.

Table 6.1. Run Type Triggers and Gate Scheme

RUN	TRIGGER (GATE)				
LABEL	PTH	P/S	QE	ETRIG	HIE
(SET UP)					
HRUN	DBG	—	—	—	—
ERUN	—	—	—	DBG	—
QRUN	—	—	DBG	—	—
(STEADY STATE)					
GRUN	20%	DBG	DBG	DBG	—
GGRUN	20%	DBG	DBG	DBG	DBG

Table 6.2. Total Triggers by Trigger Type

TRIGGER	ν EVTS	$\bar{\nu}$ EVTS
PTH, P/S	82,100	19,200
ETRIG	58,300	3,700
QE	28,300	6,500

CHAPTER 7. DATA ANALYSIS

7.1. PURPOSE

The goal of the analysis is to determine the NC neutrino-nucleon structure functions (see Equation 37, Chapter 2). The Standard Model predicts (ignoring the strange-charm asymmetry) that the CC and NC interactions couple to the quarks in exactly the same manner. It is desirable to test the Standard Model's prediction of the NC coupling. In particular, it is possible that the NC interaction couples to neutral partons within the nucleon which would be "invisible" to the CC interaction.

To date, only CHARM and our own collaboration, using the NBB data, have measured the NC x and y distributions with a large amount of data. It is hoped that by analyzing the WBB data, we can offer a complimentary method in determining the NC structure functions. In particular, with roughly twice the neutrino data as CHARM, we may have greater sensitivity to differences in the low x region.

Measurement of the NC structure functions in a Wide Band Beam must be made indirectly by comparing kinematical quantities of the NC interactions relative to the CC interactions. This is accomplished by analyzing NC/CC ratios as functions of the kinematical quantities. Also, by analyzing the data as a ratio, any flux uncertainties, in either shape or in absolute number, will cancel.

The CC structure functions have been measured^{8,6} as functions of x ($x=Q^2/2mv$) and y ($y=v/E_\nu$). The structure functions are typically parameterized using a polynomial form such as $Ax^\alpha(1-x)^\beta$. Using a parameterization, fits are made to the data and the individual parameters are determined.^{8,7} For this analysis, a particular CC parameterization will be assumed. Fits to the NC/CC ratios will determine (assuming the NC parameterization has the same form as the CC) the relative difference between NC and CC parameters.

In narrow band neutrino beams, x and y can be determined for both NC and CC interactions using the quantities E_ν , E_h , and θ_h . In a wide band neutrino beam, E_ν is unknown. Whereas x and y can still be determined for CC interactions using the information from the muon energy and/or angle, this is impossible in the NC case. It can be shown (see Appendix B) that the product of the hadronic energy and the square of the hadronic angle ($E\theta^2$) is a function of x and y , $E\theta^2 \approx 2mx(1-y)$, where m is the nucleon mass. The quantity $E\theta^2$ has, of course, the advantage of being calculable for both NC and CC neutrino interactions.

7.2. DATA ANALYSIS SOFTWARE

Analysis software was developed and maintained by the collaboration as a whole. This approach has several advantages: (1) a single set of routines are used to create, read, and unpack magnetic data summary tapes (DST's), (2) standard routines use standard variables and communication between these routines is well documented, and (3) this approach provides ready access to software updates and modifications.

A flow diagram of the data analysis is shown in Figure 7.1. We start with a set of nearly 250,000 triggers. Those triggers which

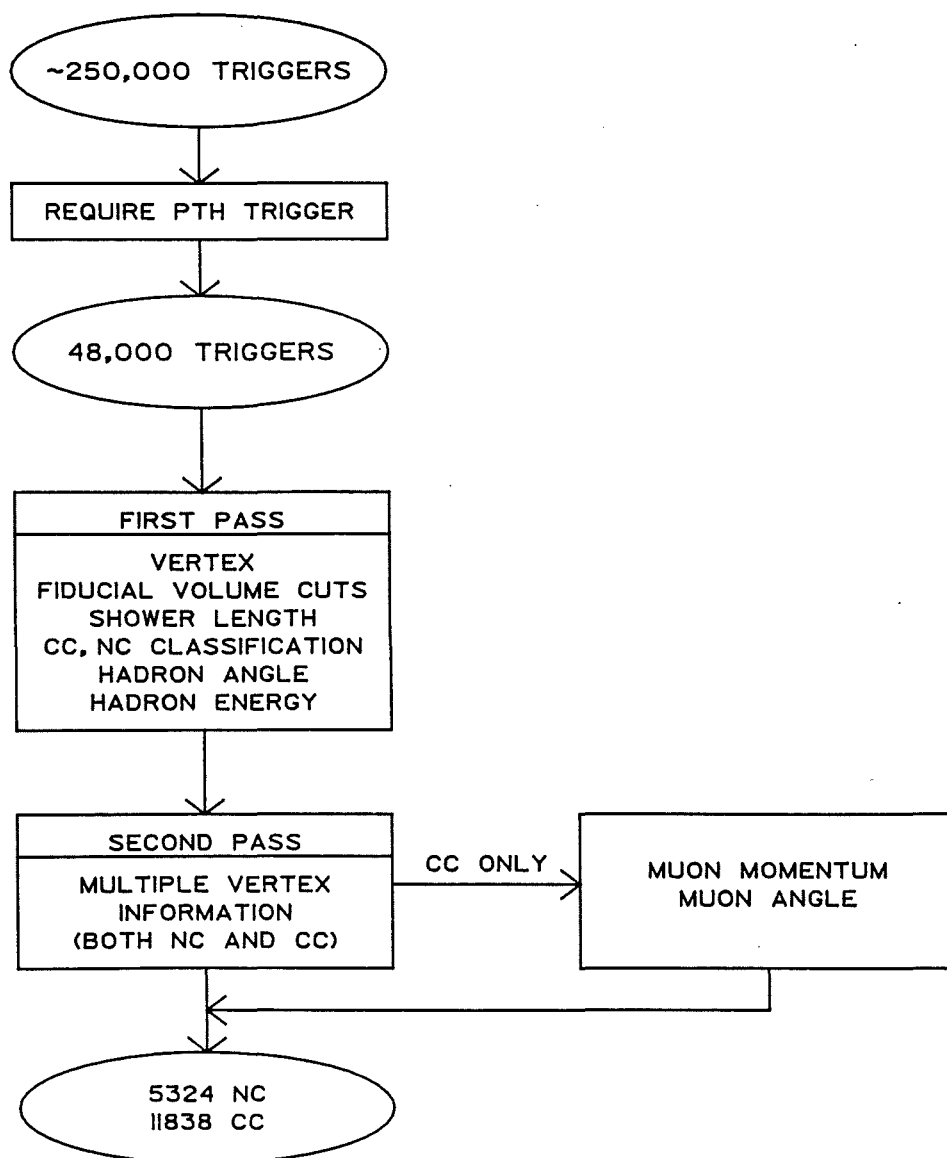


Figure 7.1. Data Analysis Flow Diagram

satisfy a PTH type trigger (PTH, PTH20%, PTH P/S) are selected out for further analysis. This filtering leaves approximately 48,000 triggers (events). These events are analyzed via software routines. A first pass analysis program determines the following quantities: interaction vertex, shower length, event classification (NC or CC event), and hadronic angle and energy. Once an event vertex is determined, fiducial volume cuts are made (to be described later) before subsequent analysis. During the second pass, triggers with multiple interactions are identified and the individual interaction vertices are determined. If an event is classified as a CC event, the muon angle and (if possible) momentum are determined.

Figures 7.2 and 7.3 show computer reconstructions of both a CC and NC event. Each picture is dominated by the flash chamber representation of the event. The neutrino beam enters from the left, and the event is shown in each of the three flash chamber views (U, Y and X). The proportional tube information is displayed above and below the flash chamber display. This shows energy deposited in each proportional tube amplifier for each of the horizontal and vertical views. To the right of the calorimeter displays are the 24' and 12' toroid displays. The struck wires for the 12' toroid proportional tube planes can be seen (for the CC event) in both horizontal and vertical views. As an example of the fine granularity available from the flash chambers, Figure 7.4 shows a blow-up of the CC event in Figure 7.2, about the region of the event vertex. At this level, each individual hit cell is clearly visible. All analysis software is designed to analyze the data at the level of the individual hits.

RUN 1426 EVENT 201
 HITS TOT = 1393
 PAT: MAX = 512 SUM = 3215 HBT = 2671

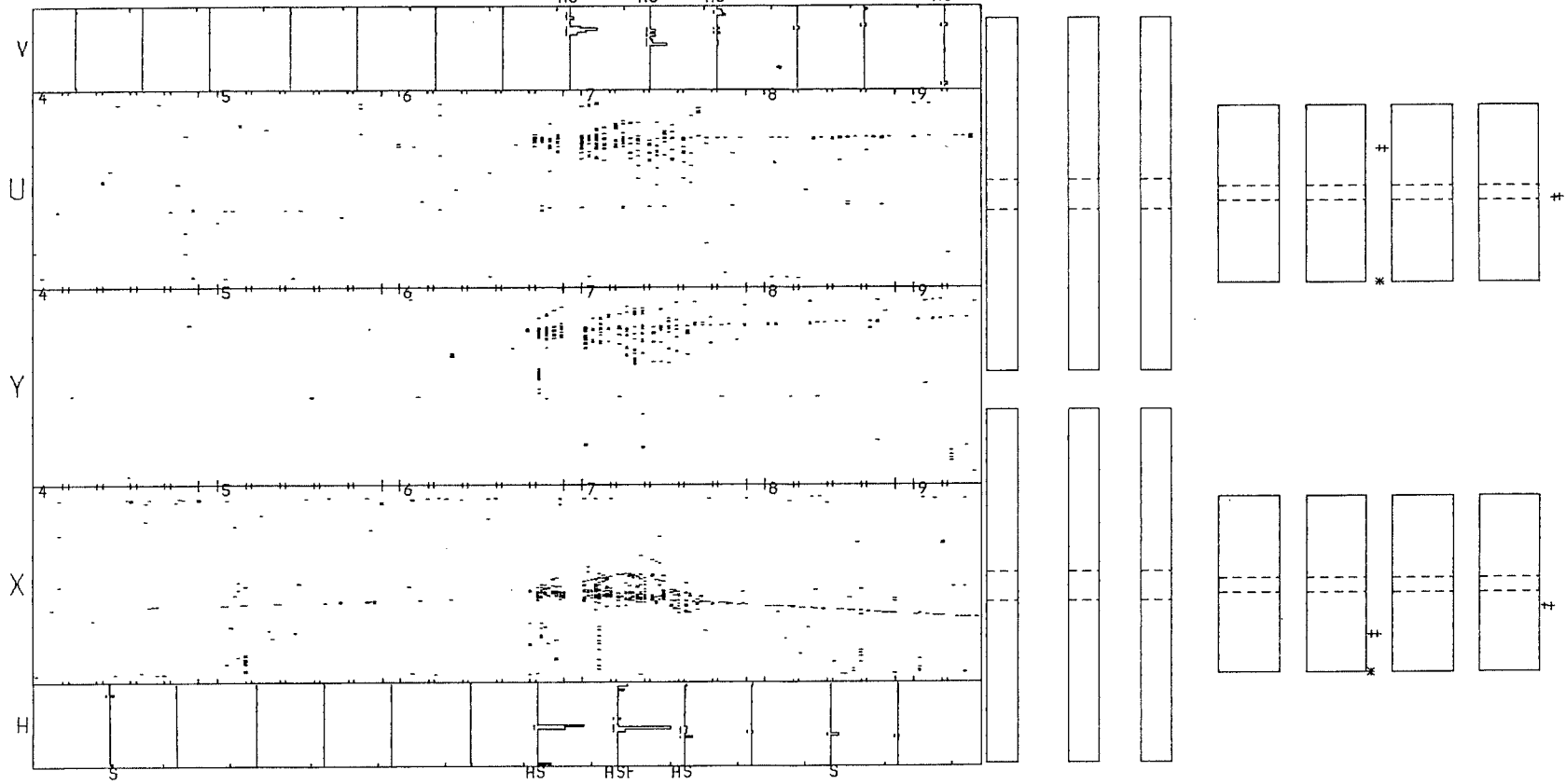


Figure 7.2. Typical CC Event

RUN 1416 EVENT 72
 TOT=1874
 PAT: MAX=2048 SUM= 7273 HBT= 6586

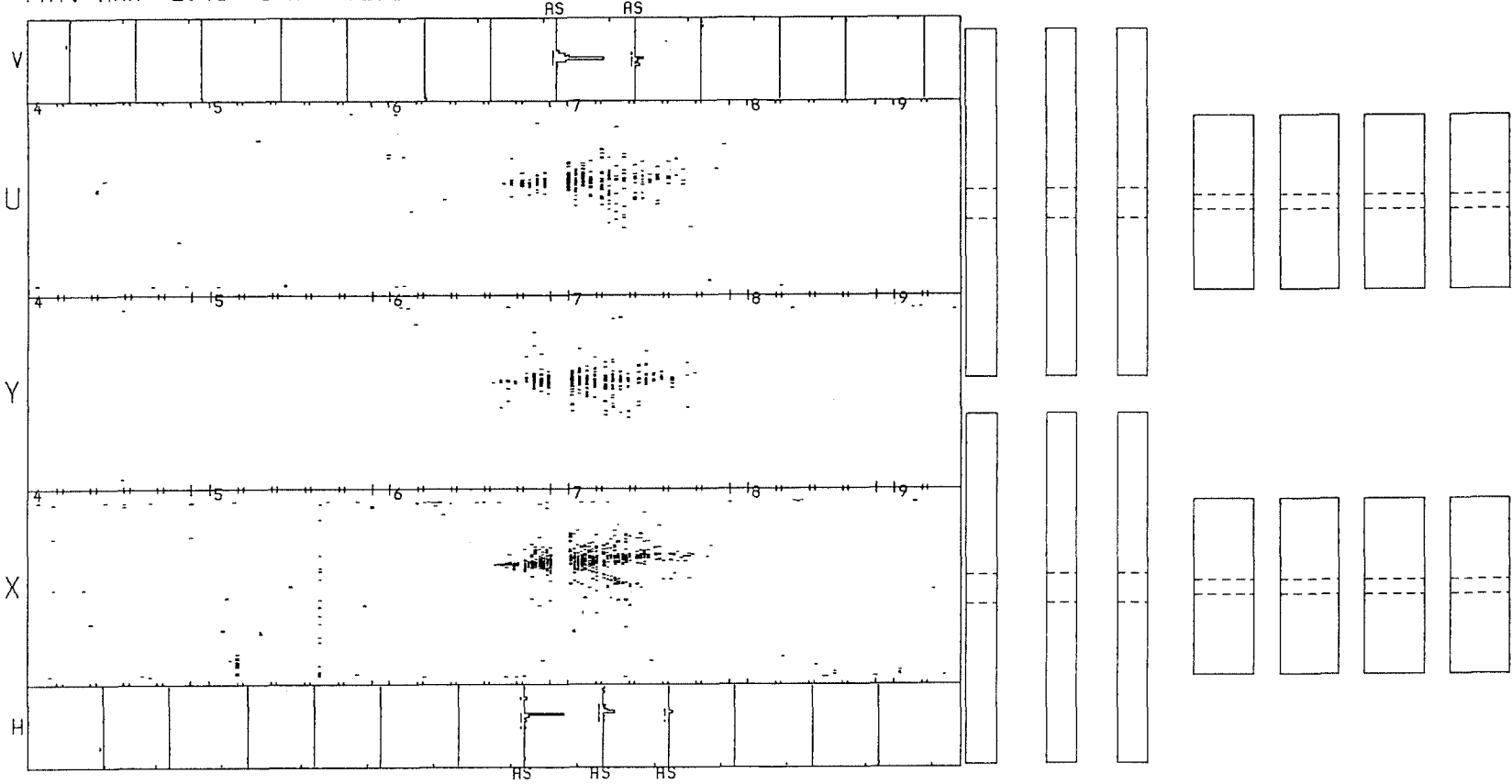


Figure 7.3. Typical NC Event

RUN 1426 EVENT 201
FITTOT=1393

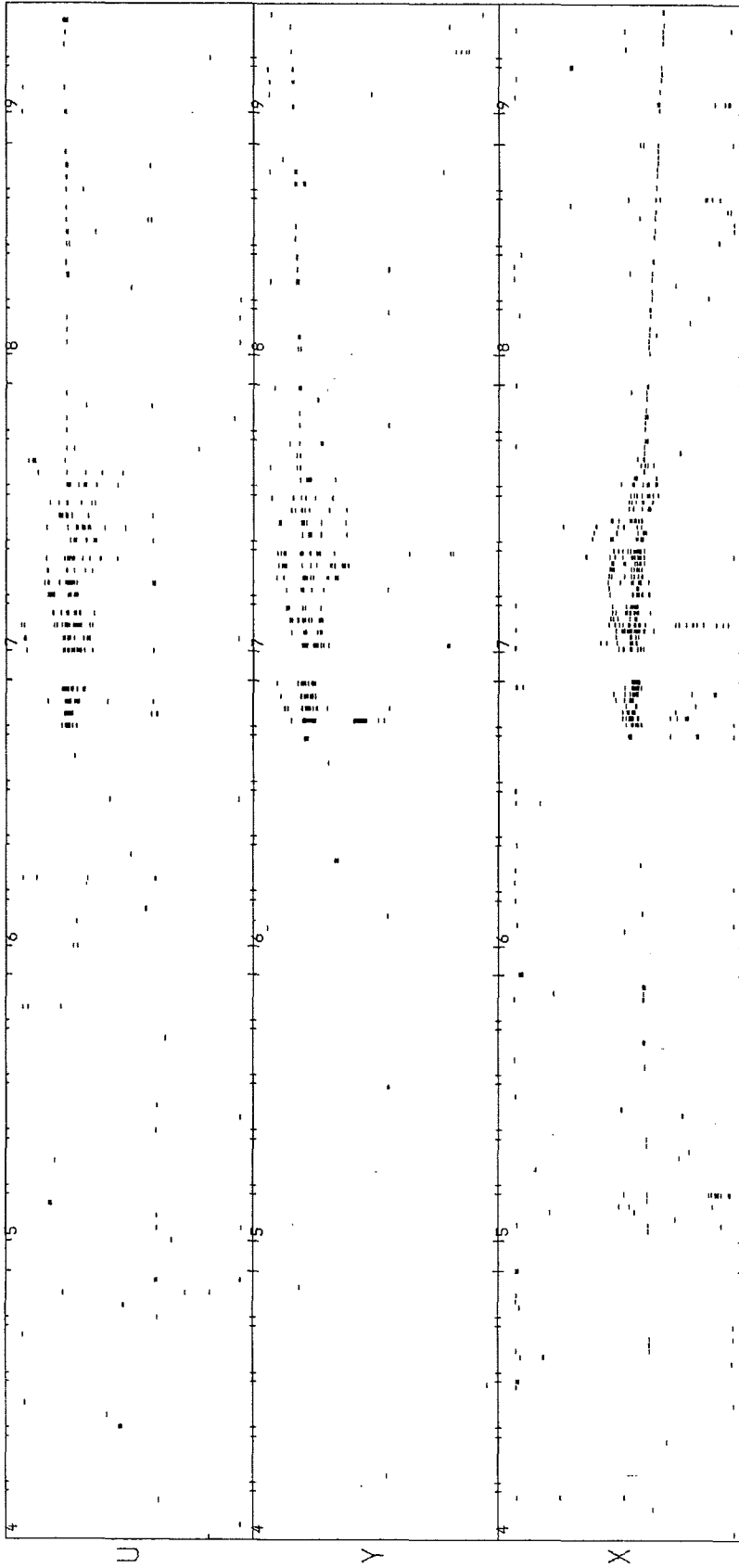


Figure 7.4. Blow-up of CC Event

The off-line software determines basic event characteristics: event vertex, hadronic shower energy and angle, event classification (NC or CC event type), shower length and density, and (in the case of an CC event) muon track angle and (if possible) muon momentum. Given basic event quantities, it is possible to determine the characteristics of the physical interactions of interest.

Vertex identification was a particularly crucial quantity since angle calculations and resolutions depend strongly upon its correct identification. The vertex finding routine initially uses the proportional plane information to localize the initial occurrence of the shower. The proportional tubes contain only information from the interaction responsible for the trigger. The flash chambers, with their long memory times, occasionally (roughly 10% of the triggers) contain information from another previous interaction within the same spill (out-of-time event). Once the vertex area has been determined both longitudinally and laterally from the proportional tubes, the flash chamber information is examined. A weighted fit is performed in a dynamic window in order to determine the vertex location.

Vertex resolution is roughly 5-7 clock counts (one clock count equals 0.23 cm) laterally and 2.2 flash chambers longitudinally. These resolutions are determined by comparing the calculated vertex to the selected vertex in the case of Monte Carlo generated showers, and by comparing calculated vertex to the vertex found by professional (human) scanners.

A separate software package was developed to look at triggers with multiple vertices. Multiple vertices have a tendency to "confuse" the hadron shower energy and angle routines, giving erroneous values. The

multiple vertex finder (MVX) locates all vertices within a given event frame, demands a good, 3-view match and then identifies a given vertex as either in- or out-of-time via the proportional tube information. The vertex algorithm is similar to the one already described. The number of good vertices (NGM) is always equal to or greater than the number of in-time, good vertices (NTM).

Hadronic energy and angle are determined by routines already discussed in the calibration section (Section 5.3). Angle is determined by calculating a center-of-gravity for hits within a given chamber, and then using the centers-of-gravity to determine shower direction. Energy is determined via enhancement of the "raw" hits. Shower length is somewhat arbitrary but usually chosen to be the point which contains 80% of the total number of hit cells. Since this procedure is applied for both CC and NC interactions, the arbitrariness is unimportant. Shower density is calculated by determining the number of hits within a triangular shaped area about the shower. Density is a useful parameter to separate hadronic and electromagnetic showers and is described in detail elsewhere.⁸⁸

In the case where the muon track penetrates through to the 12' toroid planes, the muon momentum can be determined. The algorithm requires an accurate determination of the track angle within the calorimeter, information on the position and magnetic field of the toroids, and position of the toroid proportional planes. Given the hits in the proportional planes, the tracking package can determine both the sign and momentum of the particle (muon) taking into account multiple scattering, ionization loss and curvature of the particle's path due to the magnetic field. Muon calibration data from the 1982 NBB running

period shows resolutions typically on the order of 10%. The muon angle calculation uses an algorithm similar to the hadron angle routine.

Most important, for this analysis, is the determination of an event's classification (NC or CC). Since the analysis will depend upon NC/CC ratios, misclassifying an event will contribute to larger systematic errors. Classification depends upon the ability to identify, within the calorimeter, tracks which have a high probability of being muons.

The routine created an angular histogram about the vertex of the hits from the interaction. The bin which contained the largest number of hits formed the basis for the determination of the longest track. The routine determined the angle of the track, required a 3-view constraint for the track, and calculated track length, track efficiency, and the track intercept at the vertex. Tests were performed to determine if the track left the side of the calorimeter or stopped in the calorimeter.

A matrix of criteria was used to determine if the track was a muon. The specific criteria have been listed elsewhere.⁸⁹ If a muon was not found, the event was "contrasted", that is, hits with nearest neighbors were removed, leaving only isolated tracks. A second pass was performed, and good hits in the toroid chambers were considered. After two passes, the events were classified as "CC" if a muon was found, "NC" otherwise.

Classification efficiencies were determined by comparing the algorithm's classification with either the classification from scanned data, Monte Carlo simulations, or from calibration interactions.

Average CC misclassification is $11.4 \pm 0.3\%$, determined from Monte Carlo analysis. This value has a strong kinematical dependence, especially upon y . High y events have lower muon energy, thus the muon has a greater probability of being hidden within the shower, or to travel an insufficient distance beyond the core of the shower to be considered a muon by the software.

Neutral current misclassification is $5.4 \pm 0.3\%$ and is nearly independent of kinematics. Of this 5.4%, 2-3% comes from decay muons. This number was determined from Monte Carlo, analysis of calibration data, and from analysis of CC events where the true muon track is eliminated. The rest of the misclassification is due to long, non-interacting hadron tracks, or tracks which leave the side of the detector..

7.3. DATA CUTS

Cuts are necessary to obtain a good, clean data sample. In all cases, care was taken to insure that the cuts were not biased toward either NC or CC events. As is the case with most experimental work, a compromise must be made between a very clean data sample and a sufficiently large data sample.

From an initial sample of 48,000 events (18,000 NC and 30,000 CC) the following cuts were applied in the order listed.

- 1) The low bias trigger (PTH 20% or PTH P/S) was satisfied.
- 2) Fiducial volume cuts: the vertex was required to lie within the first 320 chambers and within a radius of 130 cm from the detector center. This allowed at least 96 chambers longitudinally and at least 50 cm laterally for shower development.
- 3) Hadronic energy must be greater than or equal to 8 GeV.

- 4) The POT, muon counter and run cuts (see Chapter 6) were made to eliminate triggers with the HORN OFF condition.
- 5) Multiple vertex cuts: $NGM \geq 1$, $NTM = NGM$. This removed triggers with one or more out-of-time interactions, but kept multiple in-time interactions. Multiple in-time interactions were primarily (94%) secondary interactions of a hadron from the primary interaction.
- 6) A 3-view constraint on the primary vertex was imposed. The 3-view constraint condition is:

$$\delta = U - Y + 2 * \tan 10 (XPW - X).$$
 Data analysis revealed an rms value for δ of ± 15 clock counts. The primary vertex was required to have a $\delta \leq 45$ clock counts.

The final data sample after cuts yields:

5324 NC

11838 CC

events for an overall NC/CC ratio of 0.450 ± 0.007 . The error at this point is statistical only. The deviation of this value from theory ($R_{\nu} = 0.30$) is mainly due to CC misclassification. This problem is discussed in detail in subsequent sections.

The CC sample can be further divided into events whose muons penetrate the toroids, facilitating momentum analysis (CC), and those which have an identifiable muon in the calorimeter only (WC). (The "W" stands for "without".) The Charged Current sample breaks down as:

6923 CC

4915 WC

events. The CC events are used to determine the neutrino and antineutrino flux spectra (see Figure 6.5).

7.4. NC/CC RATIO

As stated in the preceding section, the integrated NC/CC ratio is 0.450 ± 0.007 . This ratio, as a function of $E\theta^2$ is shown in Figure 7.5. As already mentioned, theory predicts this ratio to have the value

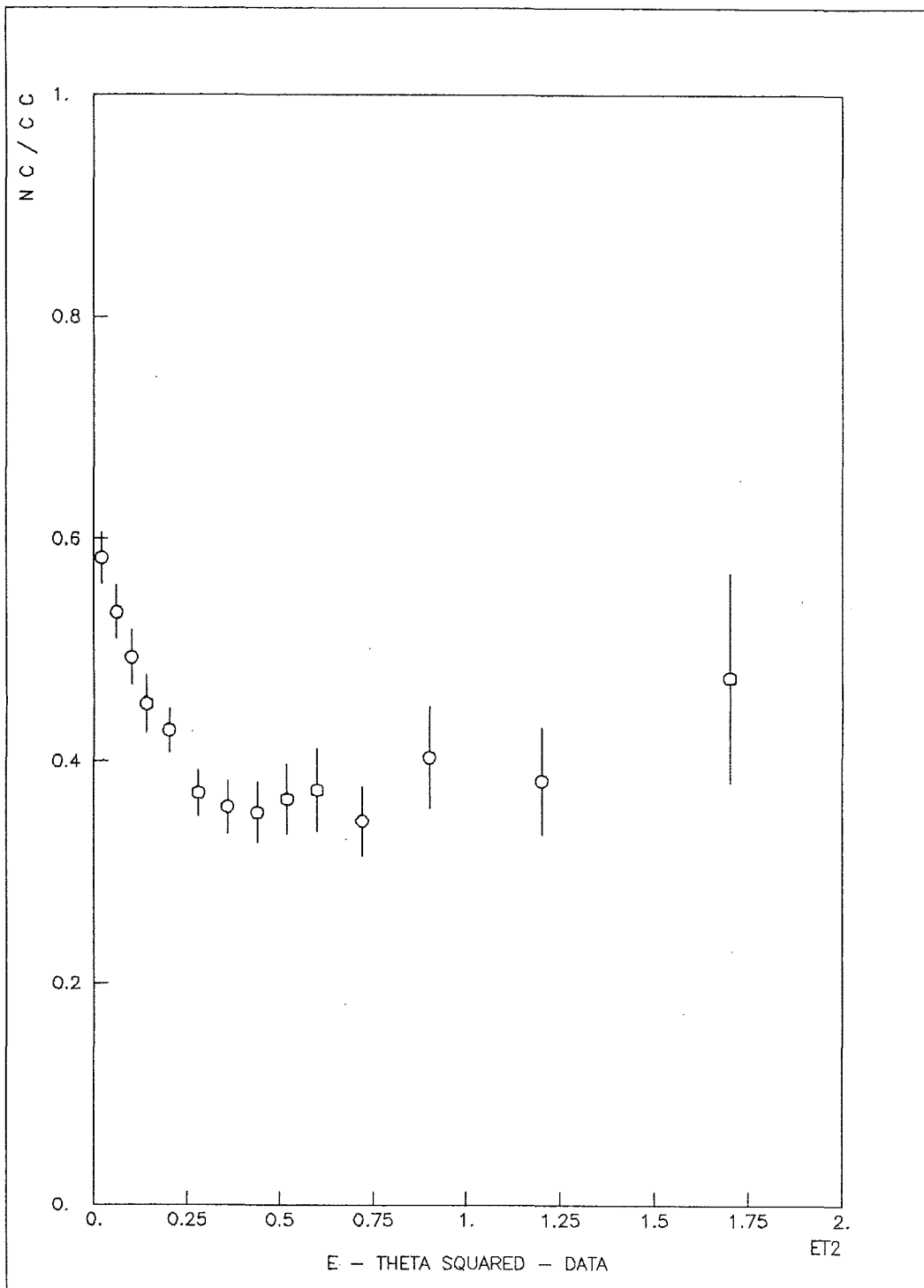


Figure 7.5. NC/CC Ratio - Data

$R_{\nu} = 0.30$, independent of x and y (and of course $E\theta^2$). In the figure, there is a hint of the ratio being flat for $E\theta^2 > 0.4$, but increases to roughly 0.6 at $E\theta^2$ near zero. This rise is primarily due to CC misclassification. Although CC misclassification is, on the average, 10%, it has a maximum at $E\theta^2$ near zero of 25% and decreases to near zero beyond $E\theta^2 = 0.75$.

Charged Current misclassification at high y is a problem. In a narrow band neutrino beam, it is possible to make a cut for both the neutral and charged current events, say $y > 0.8$, to greatly reduce or eliminate CC misclassification. Since neutrino-nucleon interactions are nearly independent of y , this reduces the sample size by approximately 20%. In a wide band neutrino beam, a y cut is not possible for the NC events. By making a low $E\theta^2$ cut, it is possible to eliminate many of the high y events, decrease the CC misclassification and achieve (hopefully) a cleaner sample. As an illustration, Figure 7.6 shows an x, y plot indicating contours of constant $E\theta^2$. The curves shown represent the "theoretical" values of $E\theta^2$ and do not include resolution smearing or geometric acceptance effects.

Cuts of $E\theta^2 < 0.2$, 0.25, and 0.3 will eliminate 87%, 91%, and 95% of the data above $y = 0.8$. Without an $E\theta^2$ cut, 18% of the events would fall above a y of 0.8. Unfortunately, the given cuts would cause the loss of 50%, 60%, and 65% of the data. Given the possibility of large data loss, an attempt was made to understand the misclassification probabilities and the effect of the antineutrino contamination via a Monte Carlo simulation, thereby regaining all or most of the data sample.

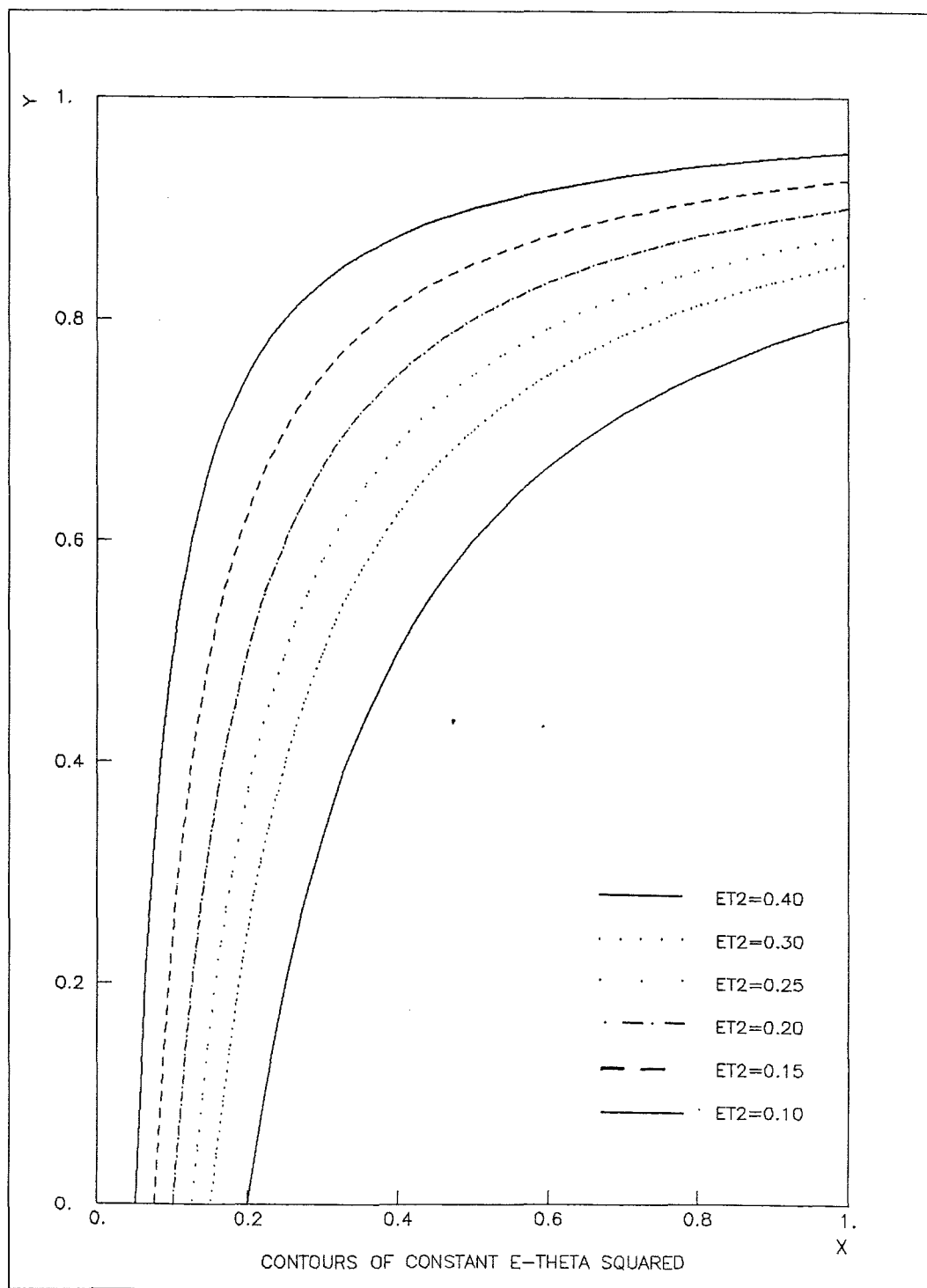


Figure 7.6. Contours of Constant $E\theta^2$

7.4.1. Monte Carlo. The experiment measures the NC/CC ratio, and this ratio can be written as:

$$\left(\frac{NC}{CC}\right)_{\text{exp}} = \frac{NC_0 + \overline{NC}_0 + \alpha CC_0 + \bar{\alpha} \overline{CC}_0 - \beta NC_0 - \bar{\beta} \overline{NC}_0}{CC_0 + \overline{CC}_0 - \alpha CC_0 - \bar{\alpha} \overline{CC}_0 + \beta NC_0 + \bar{\beta} \overline{NC}_0} \quad (1)$$

where:

$\langle \overline{CC} \rangle$: the number of true (anti) neutrino CC events

$\langle \overline{NC} \rangle$: the number of true (anti) neutrino NC events

$\langle \bar{\alpha} \rangle$: the $\langle \overline{CC} \rangle$ misclassification probability ($\langle \overline{CC} \rangle \rightarrow \langle \overline{NC} \rangle$)

$\langle \bar{\beta} \rangle$: the $\langle \overline{NC} \rangle$ misclassification probability ($\langle \overline{NC} \rangle \rightarrow \langle \overline{CC} \rangle$).

In general, all these quantities may be functions of $E\theta^2$. Since we rely only on calorimeter pattern recognition, it is not possible to differentiate between neutrino and antineutrino induced CC events.

A Monte Carlo program was used to simulate the physics and the detector. The Monte Carlo could (in principle) reproduce the experimental resolutions, acceptance loss due to geometry, and misclassification effects. If done correctly, the Monte Carlo could be used to determine the various parameters in Equation 1.

The Monte Carlo had two parts. First, the physics of the interactions had to be modeled, second, the average characteristics of the detector (density, atomic number, size, placement, and response of the flash chambers, proportional tubes and scintillators) had to be modeled.

For neutrino-nucleon kinematics, three quantities (typically E_ν , x , and y) are sufficient to completely determine the interaction. The neutrino (and antineutrino) flux spectra used the Atherton/Malensek⁹⁰ parameterization, which determined the spectrum shape as well as the

integrated flux ratio of antineutrinos to neutrinos in the wide band beam. Distributions for x and y were obtained using a parameterization by Buras and Gaemers.⁹¹

The detector Monte Carlo accepted as input, an interaction vertex, invariant mass and 3-vector momentum of the hadronic system, and 3-vector momentum of the scattered lepton. Using a "fireball" method for the hadronic system, the Monte Carlo "boils" away hadronic and electromagnetic particles and then propagates all particles through the calorimeter, taking into account the average calorimeter characteristics and chamber responses. The Monte Carlo was written so that one could use the same analysis routines used for the data. Details of the Monte Carlo and comparisons to calibration data are given in Appendix A.

A set of events was generated via the Monte Carlo. Monte Carlo showers are similar to real showers at the "macroscopic" level (i.e. angle and energy resolutions, shower width), but Monte Carlo showers tend to be narrower, denser and shorter than true showers. Single tracks (i.e. muons) have slightly lower track efficiency (by $\approx 5\%$) and hadron energy is overestimated by as much as 10-25%. Because hadron energy is overestimated, shower energy and angle are not calculated via software but derived from "smearing" the thrown (true) values. The 1980 calibration provided the resolutions as functions of energy, and so for each shower, the true energy and angle is "smeared" using a Gaussian distribution whose width was determined by the resolutions. Only the classification and geometric acceptance of the Monte Carlo data set was determined by standard software routines. Using the same fiducial volume and hadron shower energy cuts as data yields a sample of:

Monte Carlo events. This gives a NC/CC ratio of 0.451 ± 0.007 . This ratio, as a function of $E\theta^2$, is shown in Figure 7.7, superimposed upon the true data distribution. The comparison is reasonably good except at low $E\theta^2$.

With the set of Monte Carlo data, it is possible to determine the misclassification parameters ($\bar{\alpha}$ and $\bar{\beta}$) by comparing thrown event type versus software classification. Figures 7.8 and 7.9 show $\bar{\alpha}$ and $\bar{\beta}$ as functions of $E\theta^2$. For the Neutral Currents, misclassification is independent of $E\theta^2$ and is equal to $5.4 \pm 0.3\%$ for both $\bar{\beta}$ and $\bar{\alpha}$.

7.4.2. Antineutrino Distributions. Recalling Equation 1, it is necessary to deal with the \overline{CC}_0 and \overline{NC}_0 distributions. We choose to parameterize them as:

$$\overline{NC}_0(E\theta^2) = \gamma f_{nc}(E\theta^2) NC_0(E\theta^2) \quad (2)$$

$$\overline{CC}_0(E\theta^2) = \gamma f_{cc}(E\theta^2) CC_0(E\theta^2)$$

where:

$$\gamma = \frac{\int \phi_{\nu^-}(E_{\nu^-}) dE_{\nu^-}}{\int \phi_{\nu^+}(E_{\nu^+}) dE_{\nu^+}} \quad (3)$$

The f_{nc} and f_{cc} can be thought of as being the correlation functions between the neutrino and antineutrino interactions. Basically, they represent the difference in the y distributions between the two types of interactions as well as the difference in flux shapes between the two spectra. The f 's are dependent upon the particular structure function parameterization chosen. Figures 7.10 and 7.11 show $f_{cc}(E\theta^2)$ and $f_{nc}(E\theta^2)$ using the Buras and Gaemers⁹¹ parameterization.

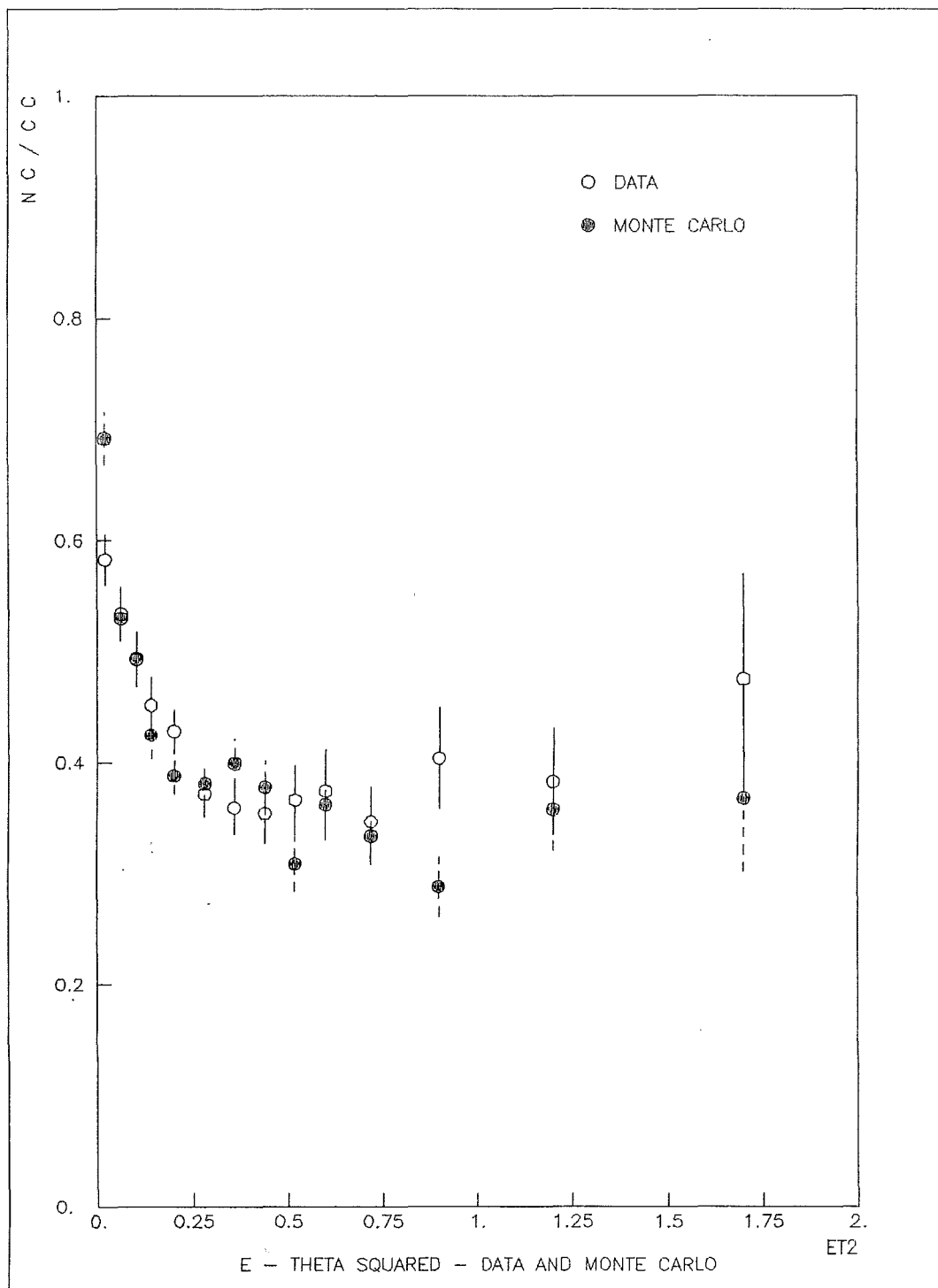


Figure 7.7. NC/CC Ratio - Data and Monte Carlo

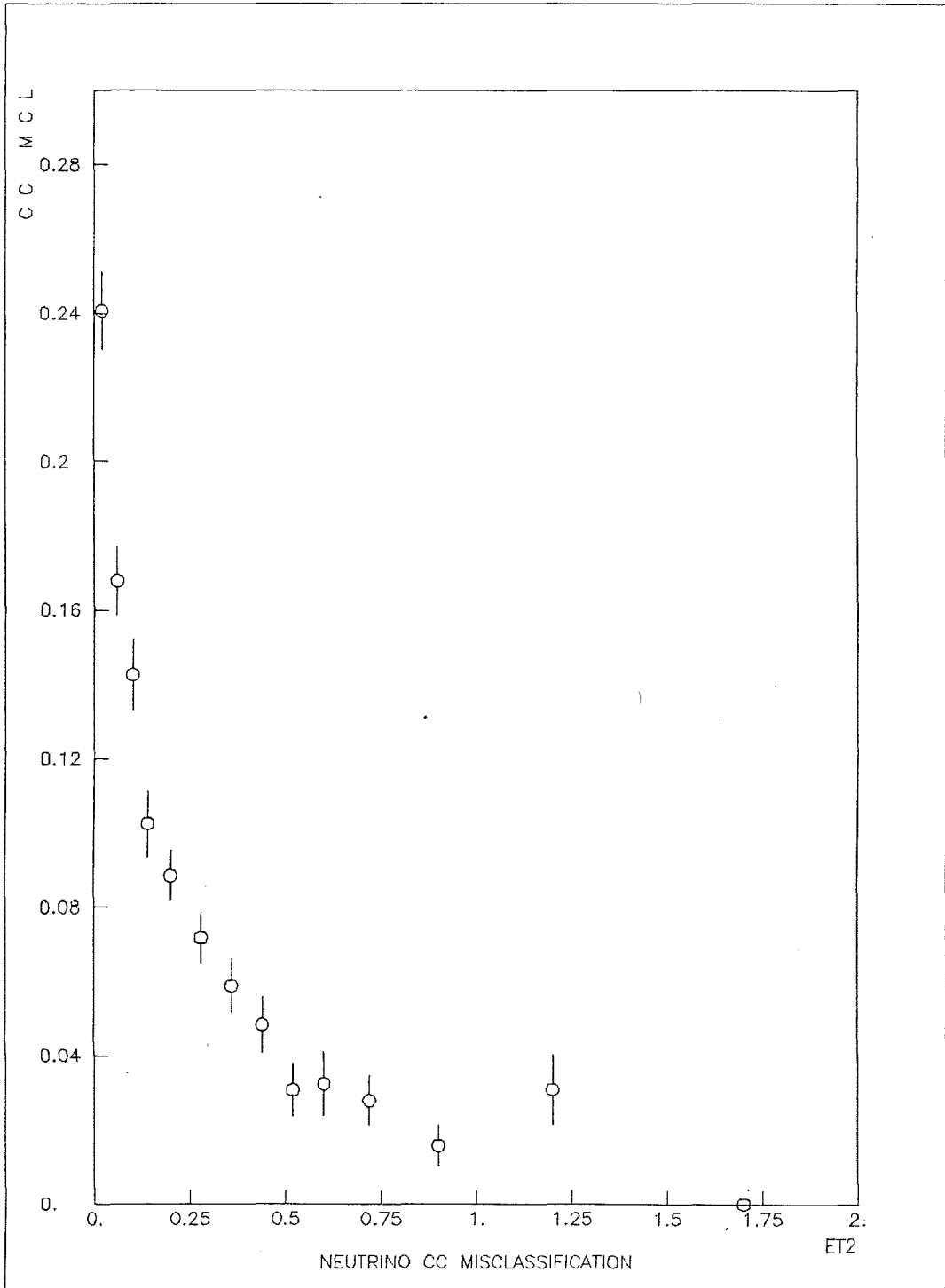


Figure 7.8. CC Misclassification as Function of $E\theta^2$

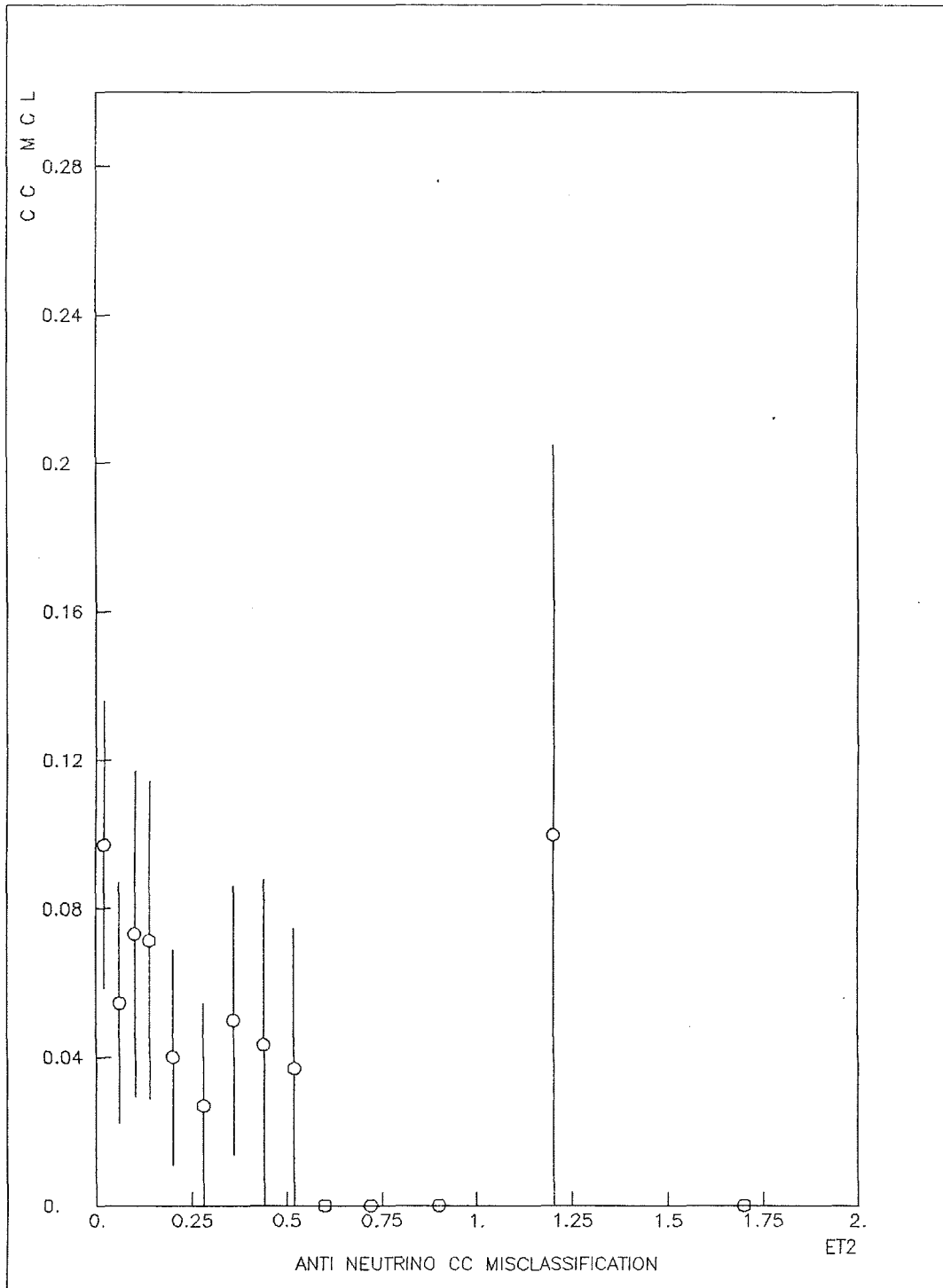


Figure 7.9. \overline{CC} Misclassification as Function of $E\theta^2$

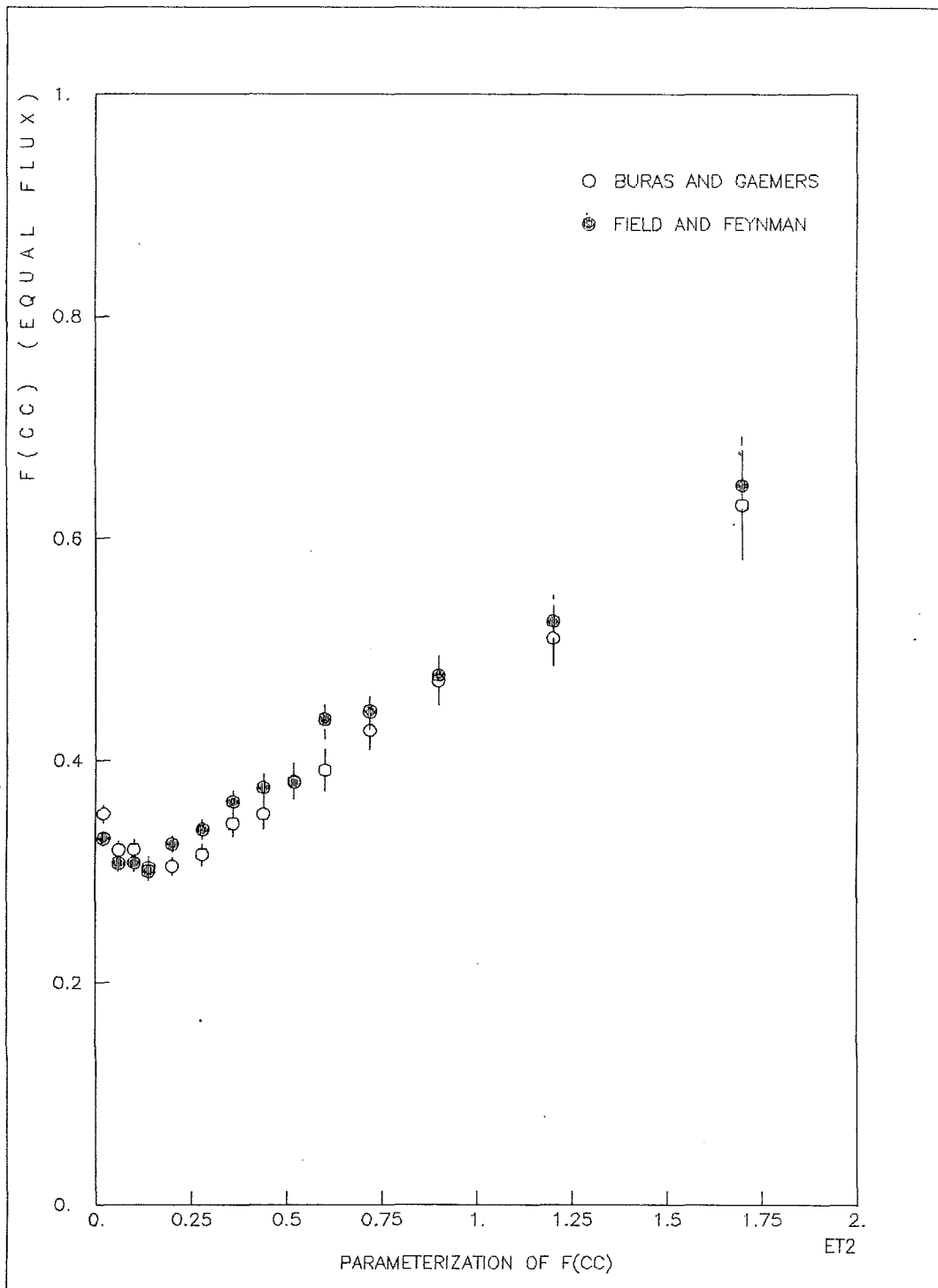


Figure 7.10. $f_{cc}(E\theta^2)$

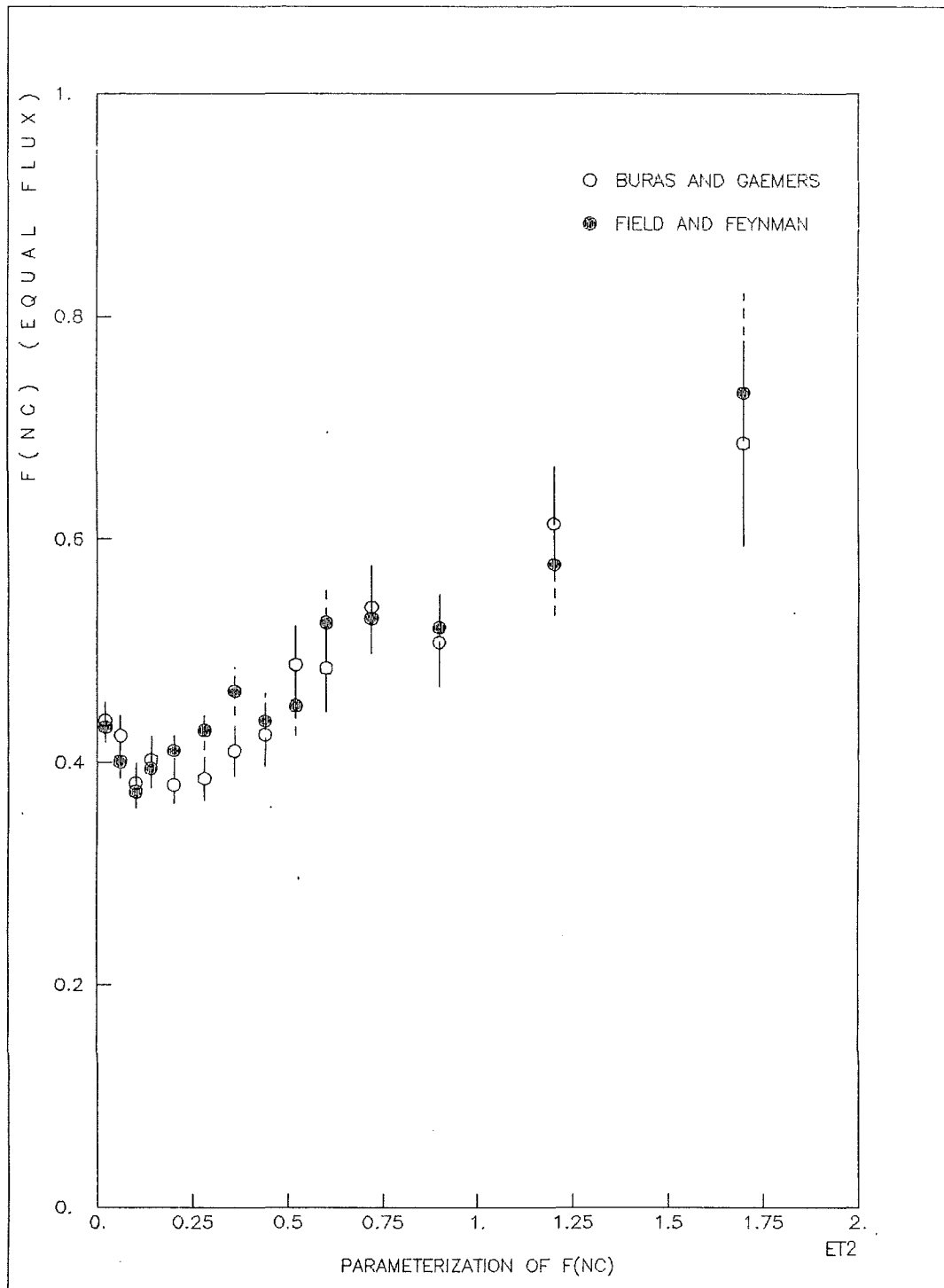


Figure 7.11. $f_{nc}(E\theta^2)$

These functions incorporate the effects of resolution smearing. Overlaid on these plots are f_{cc} and f_{nc} using a parameterization by Field and Feynman.⁹² There is very little difference between the two.

7.4.3. Correction of Data. Given reasonable understanding of the quantities in Equation 1, we can rewrite the experimentally measured distributions as:

$$\begin{aligned} NC_{\text{exp}} &= NC_0(1-\beta) + \gamma f_{nc}(1-\beta)NC_0 + CC_0(\alpha + \bar{\alpha}\gamma f_{cc}) \\ &= NC_0[(1-\beta)(1+\gamma f_{nc})] + CC_0(\alpha + \bar{\alpha}\gamma f_{cc}) \end{aligned} \quad (4a)$$

$$\begin{aligned} CC_{\text{exp}} &= CC_0(1-\alpha) + \gamma f_{cc}(1-\alpha)CC_0 + \beta NC_0(1+\gamma f_{nc}) \\ &= CC_0[(1-\alpha)(1+\gamma f_{cc})] + NC_0\beta(1+\gamma f_{nc}). \end{aligned} \quad (4b)$$

Written in matrix form, Equations 4a and 4b are:

$$\begin{pmatrix} NC \\ CC \end{pmatrix}_{\text{exp}} = \begin{pmatrix} (1-\beta)(1+\gamma f_{nc}) & \alpha + \bar{\alpha}\gamma f_{cc} \\ \beta(1+\gamma f_{nc}) & (1-\alpha)(1+\gamma f_{cc}) \end{pmatrix} \begin{pmatrix} NC_0 \\ CC_0 \end{pmatrix}. \quad (5)$$

Inverting, we obtain:

$$\begin{pmatrix} NC_0 \\ CC_0 \end{pmatrix} = \frac{1}{D} \begin{pmatrix} (1-\alpha)(1+\gamma f_{cc}) & -(\alpha + \bar{\alpha}\gamma f_{cc}) \\ -\beta(1+\gamma f_{nc}) & (1-\beta)(1+\gamma f_{nc}) \end{pmatrix} \begin{pmatrix} NC \\ CC \end{pmatrix}_{\text{exp}} \quad (6)$$

where D , the determinate of the 2 X 2 matrix in Equation 5, is:

$$D = (1-\alpha)(1-\beta)(1+\gamma f_{nc})(1+\gamma f_{cc}) - \beta(1+\gamma f_{nc})(\alpha + \bar{\alpha}\gamma f_{cc}).$$

Since all quantities are known as functions of $E\theta^2$, it is possible to correct the data bin by bin in $E\theta^2$. Figure 7.12 shows the corrected NC/CC ratio as a function of $E\theta^2$. The integrated ratio, in the range of $E\theta^2$ from 0.0 to 2.0 is $R_V = 0.302 \pm 0.007$ (stat.). For consistency, the same correction is applied to the Monte Carlo data and is shown in Figure 7.13.

As already stated, there is good agreement between data and Monte Carlo, as a function of $E\theta^2$, except at $E\theta^2$ near zero. Because Monte Carlo showers are denser and the muon track is less efficient, the Monte

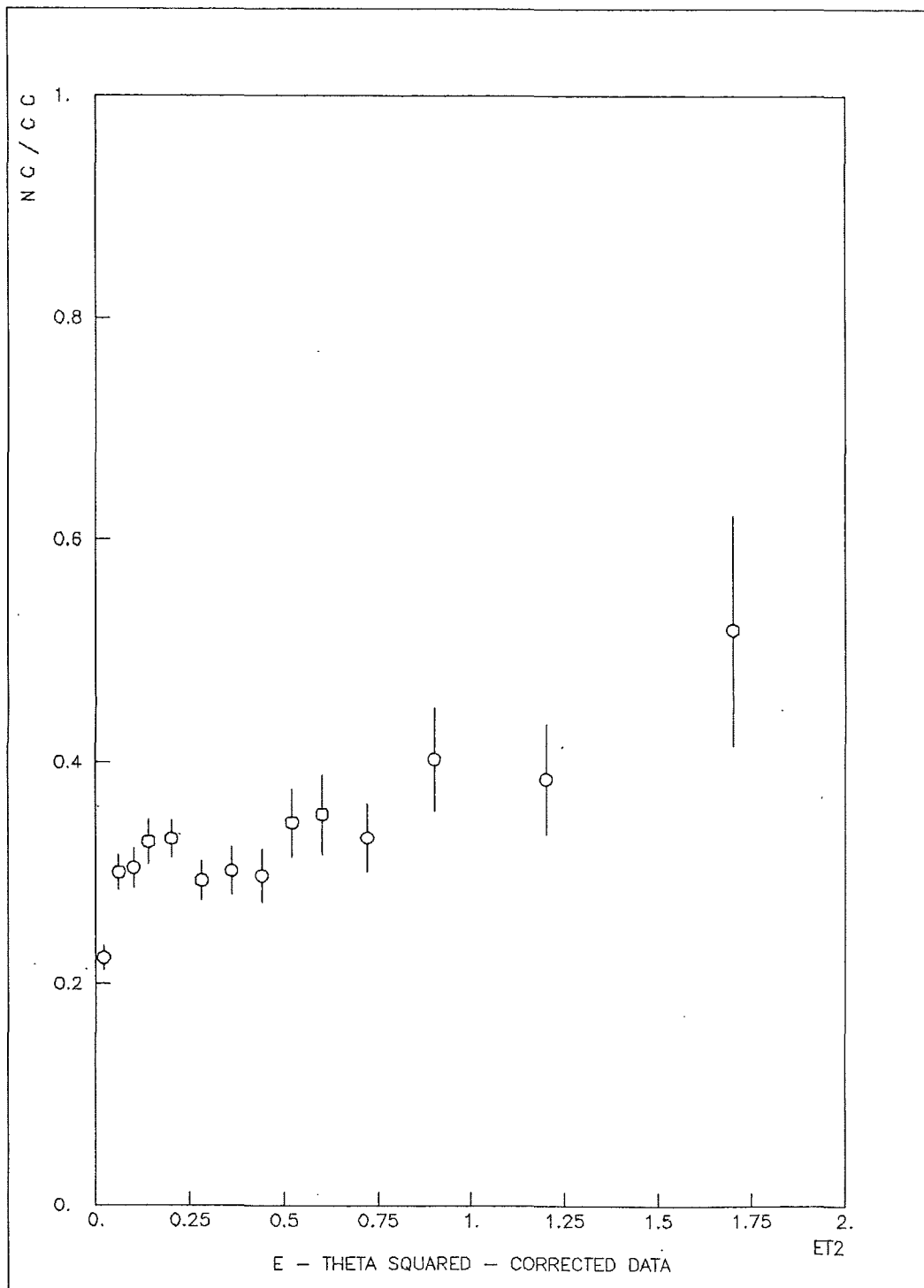


Figure 7.12. Corrected NC/CC Ratio - Data

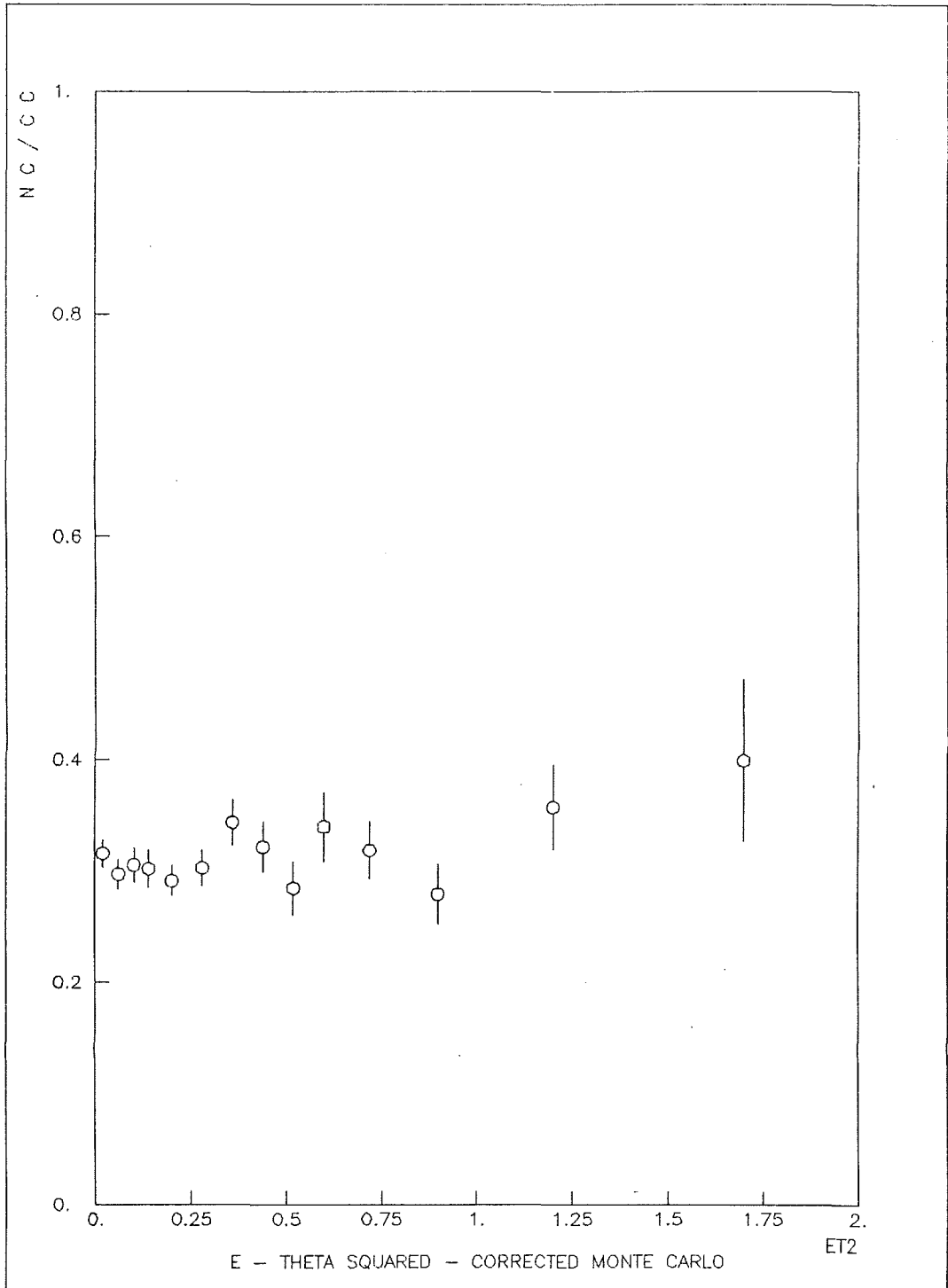


Figure 7.13. Corrected NC/CC Ratio - Monte Carlo

Carlo indicates a higher misclassification probability than data at $E\theta^2 = 0.0$. The showers in this $E\theta^2$ range have the muon track and hadronic shower nearly collinear, so given the denser shower and less efficient track, the pattern recognition routine has more difficulty identifying the event as CC. The Monte Carlo indicates a 25% misclassification for $E\theta^2 = 0.0$. Given the large correction and the "microscopic" differences between the Monte Carlo and data, we choose to avoid the full $E\theta^2$ range for the analysis.

By making a $E\theta^2$ cut of 0.1, we can maintain 75% of the data, and can apply lower corrections to the data due to CC misclassification (15% for $E\theta^2 = 0.10$, 10% for $E\theta^2 = 0.14$, and 7% or less for $E\theta^2 > 0.2$).

There is a small amount of ν_e contamination in the WBB from 3-body kaon decays. From Monte Carlo information, the energy weighted flux is estimated to be about 1.6% that of the ν_μ flux. Charged Current events from ν_e would appear as an overlapping hadronic and electromagnetic shower and would be classified as a NC event by the pattern recognition routine. Simulations indicate an overall ν_e CC/ ν_μ NC event ratio of 4%, with 50% of the events in the $E\theta^2$ range of 0.0 to 0.08. There is no direct data measurement to confirm these numbers, so corrections to the data for the ν_e induced events are uncertain. This adds an additional reason to avoid the $E\theta^2$ range below 0.1.

Given these problems, the rest of the data analysis will be confined to the $E\theta^2$ range of 0.1 to 2.0. The integrated NC/CC ratio for this region is $R_\nu = 0.323 \pm 0.007$ (stat.).

7.5. DETERMINATION OF NC STRUCTURE FUNCTION PARAMETERS

7.5.1. Parameterization. Recall that the neutrino-nucleon cross section can be written as:

$$\frac{d\sigma(\nu, \bar{\nu})}{dx dy} = \frac{G^2 ME}{\pi} \left[\left(1-y + \frac{1}{2} y^2\right) F_2(x) \pm \left(1 - \frac{1}{2} y\right) y x F_3(x) \right]. \quad (7)$$

The structure functions can be parameterized as:

$$\begin{aligned} F_2(x) &= Ax^\alpha(1-x)^\beta + C(1-x)^\gamma \\ xF_3(x) &= Ax^\alpha(1-x)^\beta \end{aligned} \quad (8)$$

which separately accounts for the sea and valence quark distributions.

For the CC case:

$$\begin{aligned} F_2^{CC}(x) &= F_2(x) \\ xF_3^{CC}(x) &= xF_3(x) \end{aligned} \quad (9a)$$

and for the NC case:

$$\begin{aligned} F_2^{NC}(x) &= \left[\delta_{uL}^2 + \delta_{dL}^2 + \delta_{uR}^2 + \delta_{dR}^2 \right] F_2(x) \\ xF_3^{NC}(x) &= \left[\delta_{uL}^2 + \delta_{dL}^2 - \delta_{uR}^2 - \delta_{dR}^2 \right] xF_3(x) \end{aligned} \quad (9b)$$

where the strange-charm asymmetry is ignored. For the analysis, the CC parameters are fixed at:

$$\begin{aligned} A_{CC} &= 3.0 / E_\beta(\alpha, 1+\beta) \\ C_{CC} &= 1.0 \\ \alpha_{CC} &= 0.5 \\ \beta_{CC} &= 3.0 \\ \gamma_{CC} &= 7.0. \end{aligned} \quad (10)$$

E_β is the standard Euler-Beta function, and the number 3 in the expression for A_{CC} is for the number of valence quarks within the nucleon. Actual measurement of the CC parameters has been done by the CHARM⁹³ collaboration, and is in good agreement with the values in

Equation 10. The analysis will focus upon determining the NC parameters relative to the CC parameters.

7.5.2. Analysis Approach. MINUIT⁹⁴ is a minimization software package written at CERN. MINUIT "steps" through an n-dimensional parameter space. At each "step" a function (which depends upon the parameters) is evaluated. MINUIT seeks to determine the parameter values which minimize the value of the function.

For this analysis, for each "step" in parameter space, 100,000 NC "events" are generated. Neutrino flux distributions are derived from the Atherton/Malensek⁹⁰ spectra. Events are weighted by the cross section given above (Equations 7, 8, and 9). For each "step" in parameter space, the cross section will have a different x distribution. Resolution smeared $E\theta^2$ values are calculated from the E_ν , x, and y distributions. Misclassification and antineutrino contamination are not incorporated.

A ratio between each set of NC events and a set of CC events (generated only once) is calculated. A chi-square value is determined between the simulated ratio and the (corrected) data ratio. The chi-square (χ^2) is defined as:

$$\chi^2 = \sum_i \left[\left(\frac{NC}{CC} \right)_{m.c.}^i - \left(\frac{NC}{CC} \right)_{c,data}^i \right]^2 / \sigma_i^2 \quad (11)$$

where i runs over the $E\theta^2$ bins, and σ_i^2 represents the statistical error of the data ratio. It is this χ^2 which MINUIT will seek to minimize. As the χ^2 minimum is reached, the parameter values at that minimum will represent the best fit to the data.

Initial analysis will concentrate on a one-parameter fit, to β_{nc} . The other NC parameters will be set to the following values:

$$A_{nc} = 3.0 / E_\beta (\alpha_{nc}, 1 + \beta_{nc}) \quad (12)$$

$$C_{nc} = C_{cc} = 1.0$$

$$\alpha_{nc} = \alpha_{cc} = 0.5$$

$$\gamma_{nc} = \gamma_{cc} = 7.0$$

$$\sin^2\theta_w = 0.23.$$

For the given $E\theta^2$ range of $[0.1, 2.0]$, MINUIT gives a value of:

$$\beta_{nc} = 2.825 \begin{array}{l} +0.292 \\ -0.254 \end{array}$$

where the errors correspond to a change of one in the chi-square per degree-of-freedom. This fitted value is quite stable with respect to the $E\theta^2$ range of the fit. Figure 7.14 indicates this stability as a function of X , where X is the lower limit of the fit range (i.e. fit range: $E\theta^2$ from X to 2.0). The points and error bars correspond to the fitted value of β_{nc} , and the crosses correspond to the fractional error, $\delta\beta/\beta$. The fractional error is seen to decrease as the fit range (hence the number of data points) decreases. This is an artifact of the one parameter fit. If both A_{nc} and β_{nc} are allowed to be free parameters, the fractional error increases as the fit range decreases. At any rate, the fitted value of β_{nc} is quite stable, even out to an X of 0.4. For reasons already discussed, we will continue to use $E\theta^2$ from 0.1 to 2.0.

7.5.3. Systematic Error Approximation. An effort was made to determine an approximation of the systematic error. Clearly, to determine the exact systematic error, a complete covariance matrix must be determined. Here we take a simpler approach. The various parameters (α , $\bar{\alpha}$, β , γ , etc.) are varied from their "nominal" value while all other correction parameters are held constant. By varying each quantity in turn, and noting its effect upon β_{nc} , an approximation to the systematic error can be determined. In Figures 7.15 and 7.16, the effect of varying α , $\bar{\alpha}$, β , and γ are shown. As in the previous plot, the points

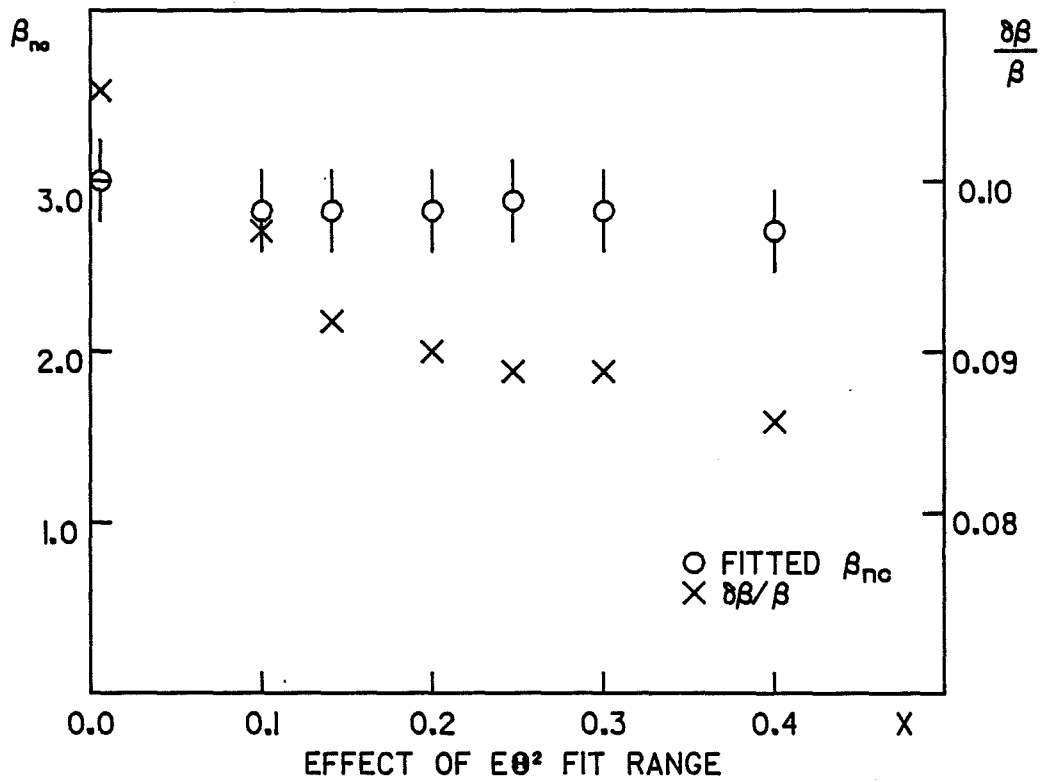


Figure 7.14. Stability of β_{nc} to $E\theta^2$ Range

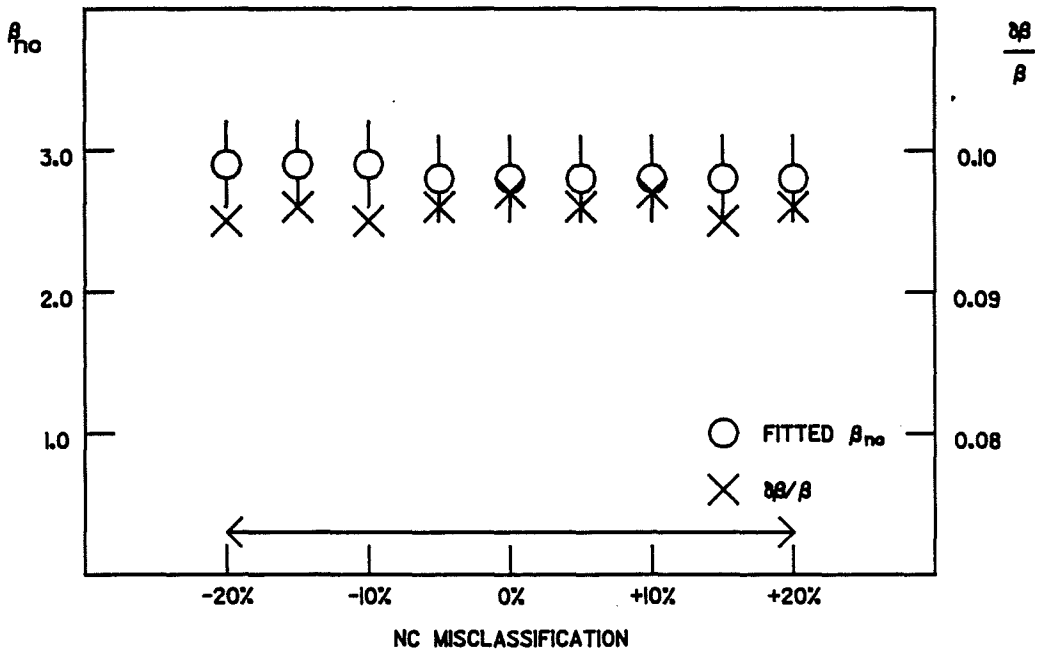
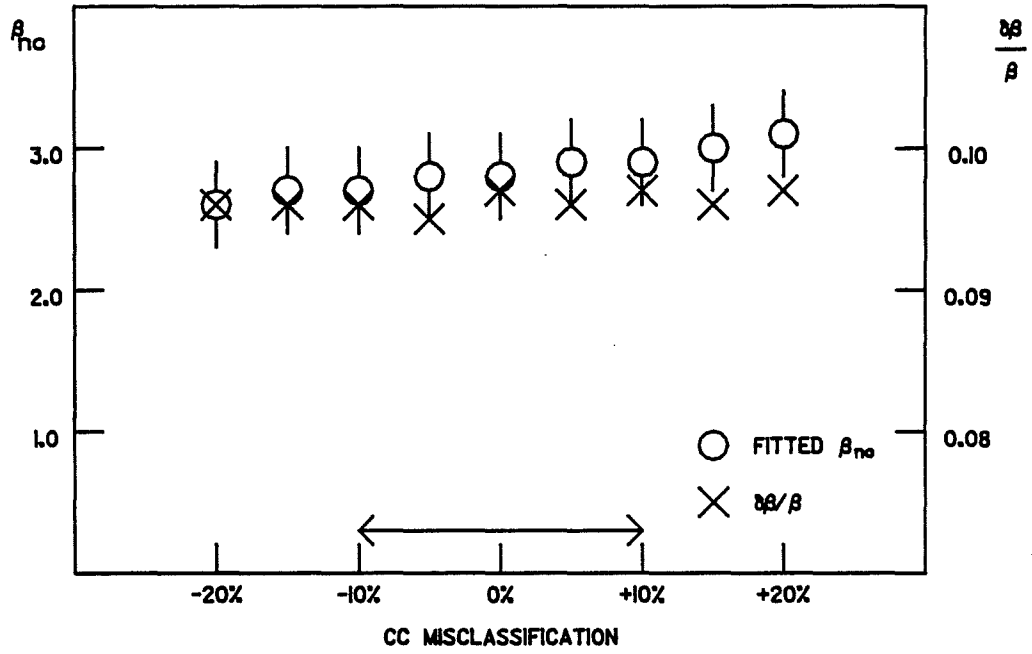


Figure 7.15. Effect Upon β_{nc} to Variations in α and β

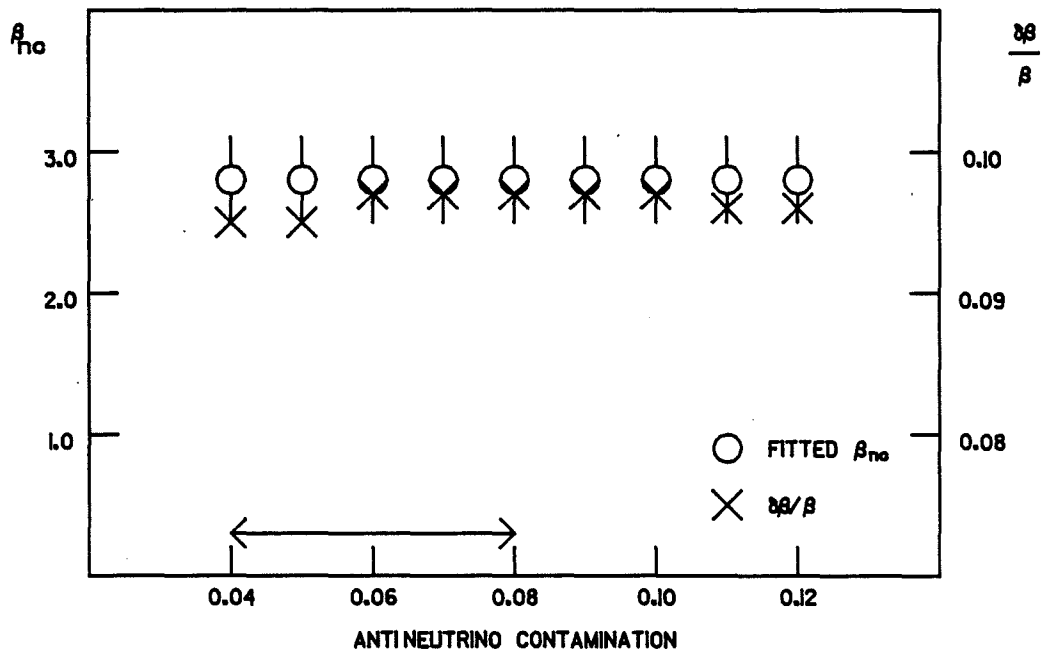
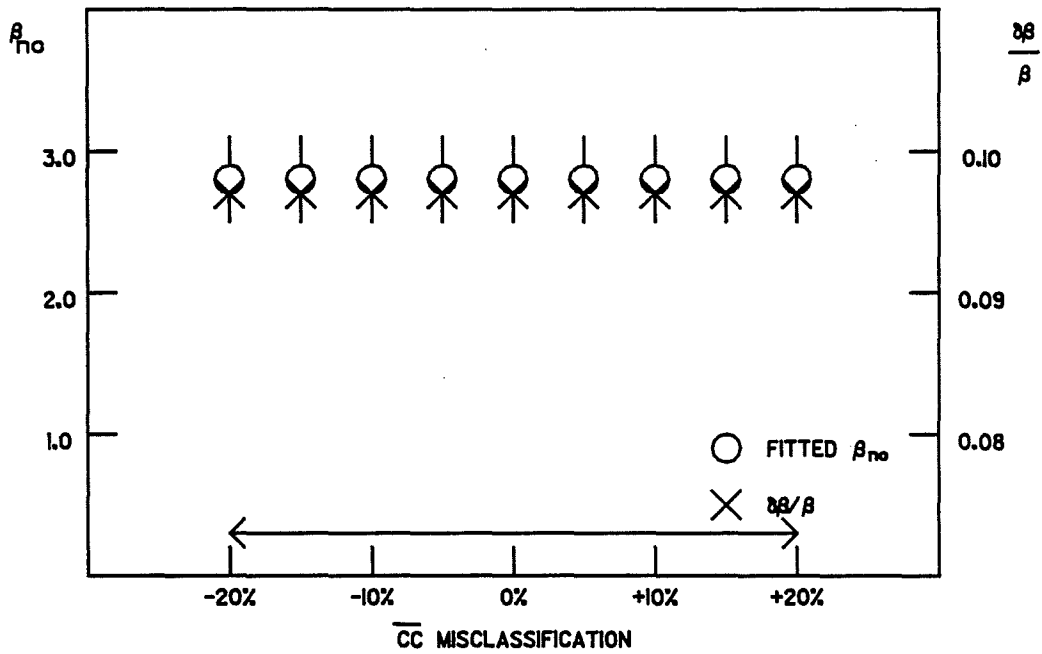


Figure 7.16. Effect Upon β_{nc} to Variations in $\bar{\alpha}$ and γ

and error bars refer to the fitted value of β_{nc} and the crosses to the fractional error. The double arrow at the bottom of each plot indicates a reasonable variation in the quantity. As seen in Figure 7.15a, changes in the value of α had the largest effect on β_{nc} .

Figure 7.17a shows the effect of changes in the magnitude of the hadronic energy resolution, and Figure 7.18 shows the effect for the hadronic angle resolution. Figure 7.17b shows the effect of a hadronic energy offset as a function of the "nominal" value. In other words, if a shower had an energy of 50 GeV, and there were a -10% systematic offset, the shower energy would be measured as 45 GeV.

Since this analysis really measures the difference in β between the NC and CC structure functions, Table 7.1 lists the effect on $\Delta\beta$ ($\Delta\beta = \beta_{cc} - \beta_{fit}$) as the initial value of β_{cc} is varied. As can be seen, a $\pm 10\%$ variation in β_{cc} results in less than a $\pm 3\%$ change in $\Delta\beta$.

Finally, "fake" sets of data were generated, and used in place of the corrected, real data. This "fake" data contained the effect of resolution smearing only. For the "fake" data, the CC parameters were set as given above (Equation 10) and the NC parameters were set to the associated CC values except for β_{nc} which was varied. This data was then fit, using MINUIT. The results of this analysis are summarized in Table 7.2. The input value of β_{nc} is given in column one, and its fitted value, via MINUIT, and error are shown in column two. In all cases, the MINUIT fits agree with the data and change as the data changes. The second entry gives the result from a set of "fake" data with a factor of four better statistics. Notice that the fitted error decreases by a factor of two, as expected.

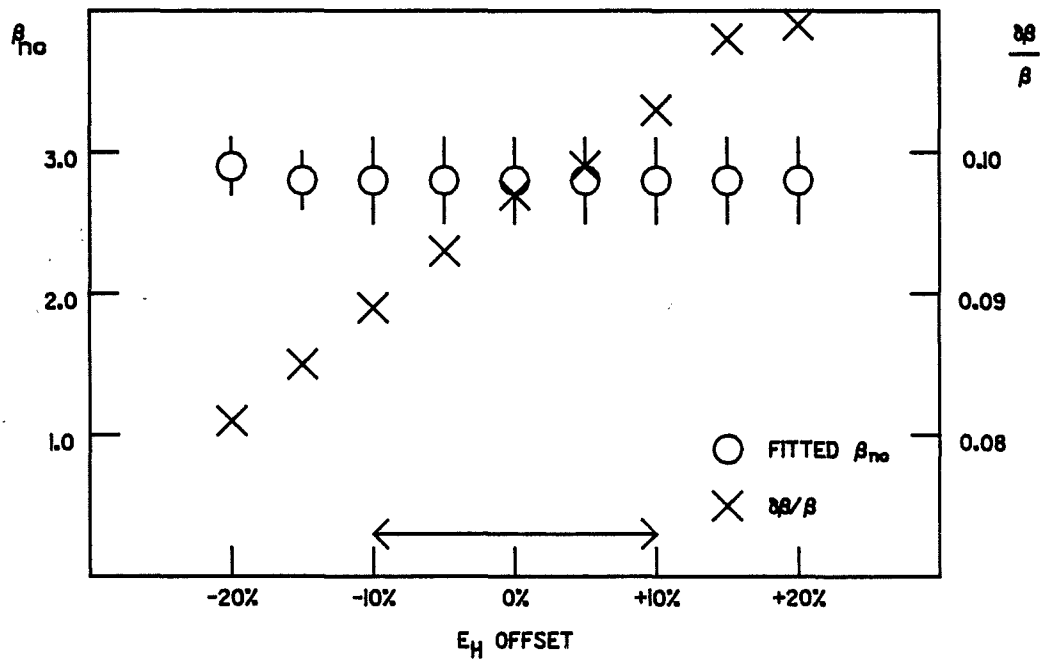
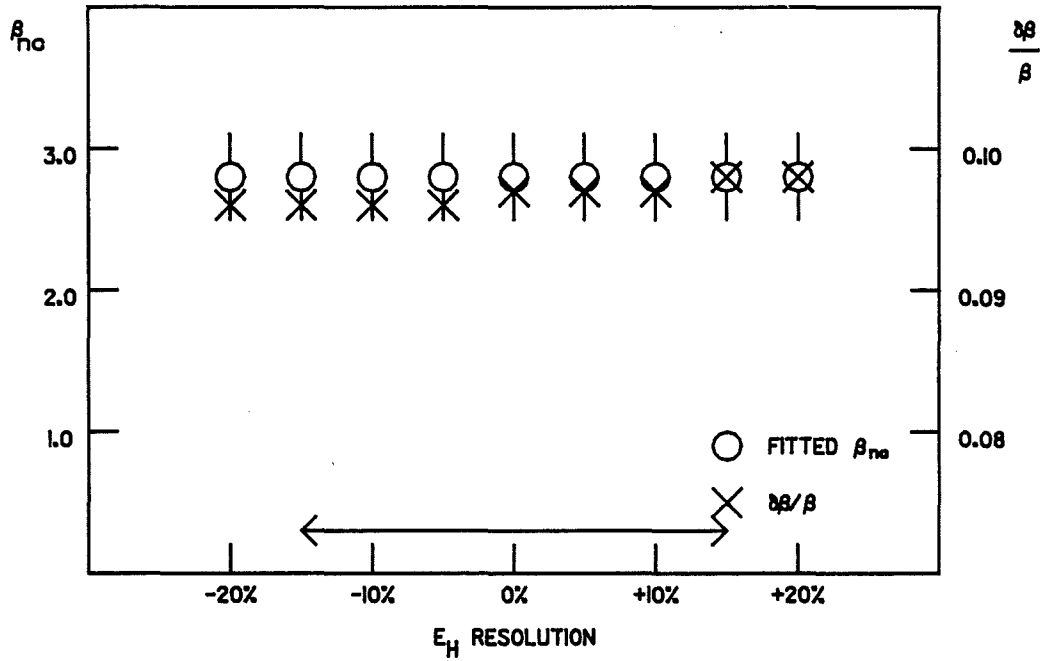


Figure 7.17. Effect of Hadronic Energy Resolution and Offset

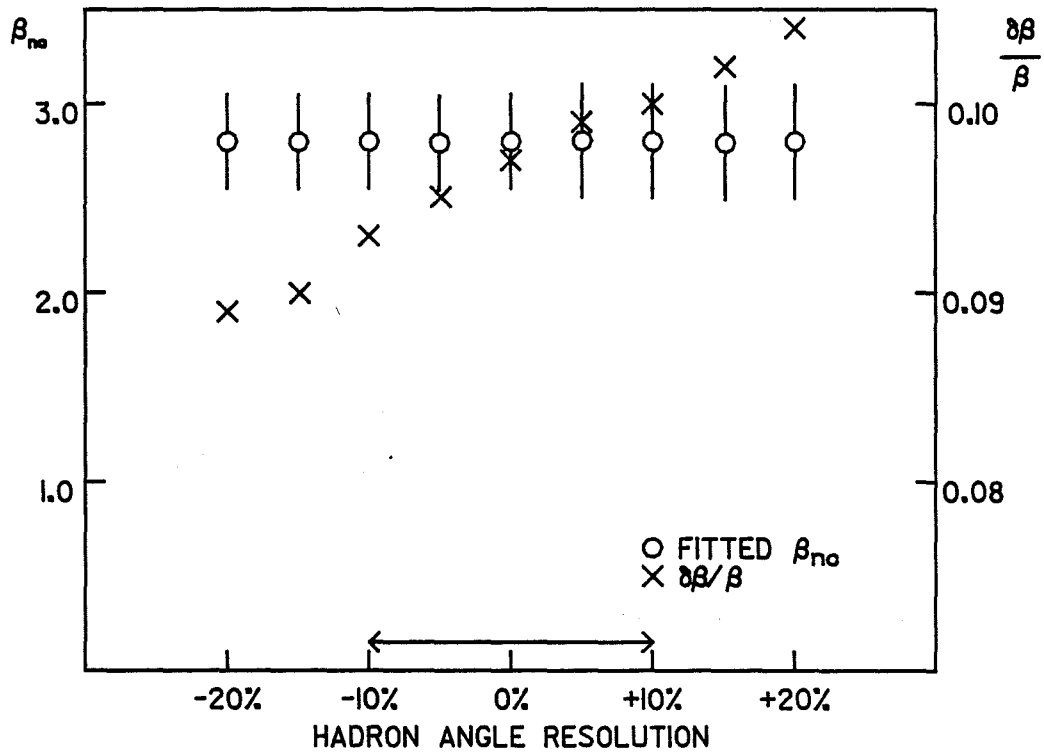


Figure 7.18. Effect of Hadronic Angle Resolution

Table 7.1. Variation of $\Delta\beta$ to β_{cc}

β_{cc}	$\Delta\beta$
2.7	0.170
2.8	0.173
2.9	0.173
3.0	0.175
3.1	0.177
3.2	0.179
3.3	0.180

Table 7.2. Fitted Values of β_{nc} for Simulated Data

INPUT β	FITTED β
3.0	2.93 ± 0.27
3.0 (4X DATA)	2.95 ± 0.14
2.7	2.67 ± 0.25
2.5	2.42 ± 0.33
2.2	2.13 ± 0.21
2.0	1.95 ± 0.20

The changes in β_{nc} associated with each of the individual variations are added in quadrature and give an indication of the approximate systematic error.

7.5.4. Results. For analysis within the $E\theta^2$ range of $[0.1, 2.0]$, we find an integrated NC/CC ratio of:

$$R_{\nu} = 0.323 \pm 0.007 \text{ (stat.)} \pm 0.025 \text{ (sys.)}.$$

With the structure function parameterization given in Equations 9a and 9b, and parameter values as given in Equations 10 and 12, a one parameter fit to β_{nc} yields:

$$\beta_{nc} = 2.825 \begin{matrix} +0.292 \\ -0.254 \end{matrix} \text{ (stat.)} \begin{matrix} +0.138 \\ -0.122 \end{matrix} \text{ (sys.)}.$$

Similar analysis was done to determine $\sin^2\theta_w$. All NC parameters were set to the corresponding CC parameter values and $\sin^2\theta_w$ was allowed to vary:

$$\sin^2\theta_w = 0.217 \pm 0.032 \text{ (stat.)} \pm 0.021 \text{ (sys.)}.$$

We then tried simultaneous two-parameter fits. Table 7.3 summarizes the results. In the case of the first entry, A_{nc} was not defined in terms of the Euler-Beta function, but was allowed to be a free parameter. Three-parameter fits were attempted, but all sensitivity to variations in the fitted parameters was lost.

7.6. COMPARISON WITH OTHER EXPERIMENTS

The E594-NBB run took data at four different beam conditions. For neutrinos, the secondary momentum was set at 165, 200, and 250 GeV, and at 165 GeV for antineutrinos. Table 7.4a lists the number of NC and CC events at each beam condition. The analysis used the same structure function parameterization⁹⁵ (see Equation 8) and performed a simultaneous fit to the x distributions of the four data sets. An

Table 7.3. Results of Two-Parameter Fits

FITTED PARAMETERS	STATISTICAL ERROR	SYSTEMATICAL ERROR
$A = 2.859$	+1.033 -0.764	+0.402 -0.387
$\beta = 2.568$	+0.756 -0.616	+0.226 -0.246
$C = 0.840$	+0.593 -0.572	+0.284 -0.286
$\beta = 2.747$	+0.432 -0.337	+0.046 -0.054
$a = 0.432$	+0.165 -0.115	+0.064 -0.060
$\beta = 2.379$	+1.113 -0.781	+0.315 -0.309

Table 7.4. Summary of NBB Analysis

SECONDARY MOMENTUM (GEV)	NC	CC
+165	873	2766
+200	590	1992
+250	548	1784
-165	597	1563

	CC	NC
α	0.5	0.53 ± 0.10
β	3.0	3.17 ± 0.58
$\bar{q}/(q+\bar{q})$	0.136	0.13 ± 0.02
A	3.28	3.33 ± 0.58
β	3.0	3.02 ± 0.34
$\bar{q}/(q+\bar{q})$	0.136	0.14 ± 0.02

initial fit to the NC/CC ratio yielded a value of the Weinberg angle of $\sin^2\theta_W = 0.243 \pm 0.014$. Subsequent analysis, to determine other parameters, set $\sin^2\theta_W = 0.24$ and the CC parameters to the values given in Equation 10. Results are summarized in Table 7.4b. In all cases, NC parameters which are not fitted are set equal to the corresponding CC parameter values.

CHARM took data for both neutrinos and antineutrinos with a secondary beam momentum of 200 GeV in each case. Event numbers are summarized in Table 7.5a. CHARM used a parameterization⁹³ similar to the parameterization used for this analysis and is defined as:

$$q_{\text{val}}(x) = \frac{3}{E_p(a,b+1)} x^a(1-x)^b$$

$$q_{\text{sea}}(x) = C(c+1)(1-x)^c.$$

where C is the integral over the sea quark content of the nucleon and is used to determine the relative antiquark content, $\bar{q}/(q+\bar{q})$. The shape of the sea quark distribution is fixed by setting $c = 6.18$. Fits are performed simultaneously to both sets of data.

Because of inherent beam momentum spread, ambiguity between neutrinos from pion and kaon decays, and limitations in the experimental resolutions, especially in the hadron shower angle, event-by-event kinematical reconstruction of the NC events was not possible. Instead, distributions of the measured quantities were unfolded to determine the x distributions. This unfolding method was also applied to the CC events to determine its validity. Fit results are shown in Table 7.5b.

Table 7.5. Summary of CHARM Analysis

SECONDARY MOMENTUM (GEV)	NC	CC
+200	1967	6549
-200	863	2516

	CC W/ MUON MEASUREMENT	CC FROM UNFOLDING	NC FROM UNFOLDING	SYS. ERROR
a	0.47 ± 0.02	0.45 ± 0.05	0.44 ± 0.05	± 0.05
b	2.71 ± 0.11	2.97 ± 0.16	2.79 ± 0.24	± 0.09
$\bar{q}/(q+\bar{q})$	0.14 ± 0.005	0.17 ± 0.03	0.13 ± 0.03	± 0.02

CHAPTER 8. CONCLUSIONS

We have shown that it is possible to make a detailed analysis of the Neutral Current interaction in a Wide Band neutrino beam. Having demonstrated a reasonable understanding of misclassification effects and of the antineutrino contamination, we are able to apply corrections to the data for these effects. With a proper choice of variable ($E\theta^2$), which can be calculated for both Neutral and Charged Current interactions, we are able to gain information about the NC structure functions. In particular, given certain assumptions about the form of the CC structure functions, differences between the Neutral and Charged Current structure functions can be determined.

For an $E\theta^2$ range of 0.1 to 2.0, the (corrected) NC/CC ratio is:

$$R_\nu = 0.323 \pm 0.007 \text{ (stat.)} \pm 0.025 \text{ (sys.)}.$$

This is compatible with a value of $\sin^2\theta_w$ of:

$$\sin^2\theta_w = 0.217 \pm 0.032 \text{ (stat.)} \pm 0.025 \text{ (sys.)}.$$

World data⁹⁶ indicate a NC/CC ratio of roughly 0.30 to 0.32 and a value of $\sin^2\theta_w = 0.23 \pm 0.01$. Both values are in good agreement with world data. Assuming a structure function parameterization of:

$$F_2(x) = [3.0/E_\beta(\alpha, 1+\beta)]x^\alpha(1-x)^\beta + C(1-x)^\gamma$$

$$xF_3(x) = [3.0/E_\beta(\alpha, 1+\beta)]x^\alpha(1-x)^\beta,$$

and assuming parameter values for the CC structure functions, a one-parameter fit to the value of β_{nc} is:

$$\beta_{nc} = 2.825 \begin{array}{l} +0.292 \\ -0.254 \end{array} \text{ (stat.)} \begin{array}{l} +0.138 \\ -0.122 \end{array} \text{ (sys.)}.$$

Two parameter fits for β_{nc} and one other parameter yield in turn (with A_{nc} replacing the quantity $[3.0/E_{\beta}(\alpha, 1+\beta)]$):

$$\begin{aligned} A_{nc} &= 2.859 \begin{array}{l} +1.033 \\ -0.764 \end{array} \text{ (stat.) } \begin{array}{l} +0.402 \\ -0.387 \end{array} \text{ (sys.)} \\ C_{nc} &= 0.840 \begin{array}{l} +0.593 \\ -0.572 \end{array} \text{ (stat.) } \begin{array}{l} +0.284 \\ -0.286 \end{array} \text{ (sys.)} \\ \alpha_{nc} &= 0.432 \begin{array}{l} +0.165 \\ -0.115 \end{array} \text{ (stat.) } \begin{array}{l} +0.064 \\ -0.060 \end{array} \text{ (sys.)} \end{aligned}$$

The value of β_{nc} in each case is compatible with the value obtained from the one parameter fit. All parameters are in good agreement with results from both the NBB data and from CHARM. On the basis of the analysis, within the errors cited, there is no difference between the NC and CC interactions. The NC interaction couples to the quarks in the same manner as does the CC interaction, and there is no evidence of coupling to neutral partons within the nucleon.

Even though the WBB offers a higher interaction rate, and thus a larger data sample, the WBB is not ideal for this type of analysis. It is not possible to determine the variables x and y for NC interactions. To minimize the CC misclassification, it is advantageous to make a high y cut. Without a similar cut in the NC sample, the data sample becomes biased. The detector, however, is well suited to analyze the NC structure functions as the NBB analysis shows.

Despite the slightly larger data sample, the errors on the fitted parameters are roughly a factor of two (or more) than the errors on the values from the NBB or CHARM. The NBB had available four separate sets of data, including a data set from the antineutrino running. Whereas we used roughly 10 data points for the fitting, the NBB analysis had roughly 40 points for analysis (10 from each run condition). Incorporating both neutrino and antineutrino data adds an additional constraint to the fitting by virtue of the sign change on the xF_3 term

in the cross section. The CHARM group also could incorporate both neutrino and antineutrino data. The antineutrino run period during the WBB was short, and the neutrino contamination in the antineutrino sample was significant, thus the sample was of too poor a quality to be incorporated into this analysis. Had comparable neutrino and antineutrino samples been available, we expect, based upon the NBB analysis, that the errors would have decreased by roughly a factor of two.⁹⁷ Analysis based upon a Monte Carlo program suggests that a factor of four more data would also reduce the errors by a factor of two.

Currently, (December 1984) the collaboration is preparing to take data in a WB neutrino beam utilizing the Fermilab Tevatron. Primary proton energy is doubled (800 GeV) and the neutrino beamline will use a quadrupole magnet focusing system for the secondary mesons. This will increase the average neutrino energy from approximately 20 GeV (for this analysis) to roughly 120 GeV, a factor of six. Average muon energy in CC interactions will also be higher by this amount, thus greatly reducing the CC misclassification problem. With the prospects of smaller corrections to the data, and if comparable neutrino and antineutrino samples can be obtained, the upcoming run period offers the opportunity for significant contributions to the study of NC structure functions. I, of course, offer this opportunity to the next generation of students.

APPENDICES

APPENDIX A

THE E594 MONTE CARLO PROGRAM

The Monte Carlo package allows the user to simulate neutrino induced electromagnetic and hadronic showers within the context of the E594 detector. A user writes a control program and selects the appropriate "physics" to be simulated. The user supplies the interaction vertex, interaction "particle" (where the "particle" can be a hadron, electron, muon, or even a hadronic "fireball") and three-vector momentum of the "particle". In the case where a hadronic "fireball" is selected, the invariant mass must also be supplied. The Monte Carlo package will then control the interaction's propagation and development through a model of the detector taking into account nuclear interactions, particle decays, multiple Coulomb scattering, ionization energy loss and bending in a magnetic field for all particles produced in the interaction. Flash chamber and proportional tube data is generated, with data organized in the same manner as the real data.

A.1. ELECTROMAGNETIC SHOWERS

Electromagnetic showers are generated by randomly generating hits according to longitudinal and lateral distribution functions. These functions have been parameterized, and the parameterization is based upon our calibration electron data. The only adjustable parameters in these functions are the critical energy and the radiation

length appropriate for the target material. One of the inherent limitations of this scheme is that there is no correlation in hits from flash chamber to flash chamber (i.e. particle tracks are impossible). Given that electromagnetic showers in our detector appear dense and narrowly collimated, the lack of hit correlation in the Monte Carlo showers is not critical at the "macroscopic" level. The Monte Carlo package does not handle large angle (with respect to the beam axis) showers very well. Since electromagnetic showers from neutrino-electron interactions occur at small angles to the beam direction, this also is not a serious problem.

A.2. HADRONIC SHOWERS

The ability of the Monte Carlo package to simulate a hadronic interaction is a more important consideration for this analysis. Hadronic showers have far more detail, (i.e. individual tracks are apparent) so hadronic interactions are treated in more detail. The original "fireball" of the hadronic system is de-excited using an isotropic cascade model.^{98,99} Particles (which may be excited) are propagated through the simulated detector. In hadron-nucleon collisions, both non-resonance and resonance collisions are considered.

Resonance collisions are handled via a crude model. The Monte Carlo utilizes information of the total cross section for production of Δ 's and N^* 's. The Monte Carlo uses only the lowest lying resonance (actually, the only large one) and assumes isospin symmetry. To decay the state, a choice is made between treating it as a resonance or as a normal cascade, with the relative probabilities given by the ratio of

the total cross section to the extrapolated cross section outside the resonance region. Only de-excitation by pion emission is considered.

Non-resonance collisions are more complex. Initially, only hadron-hadron collisions are considered, with a simple extension to hadron-nucleon collisions. Hadron-hadron collisions are handled in a two step process. First, a diffractive scattering model⁹⁸ is used to select the transverse momentum and mass of the outgoing particles (one or both of which may be excited). Second, the outgoing fireballs (if any) are de-excited, using the isotropic cascade model. This model for hadron-hadron collisions is tuned to give the correct elastic to inelastic cross section ratios, x-Feynman distributions (including leading particle effects) and particle multiplicity.

Extension to hadron-nucleon collisions is simple. The target nucleon is given a random momentum to simulate Fermi motion. The energy of the projectile-target system is reduced to remove the energy added by the Fermi motion, and to simulate nuclear excitation.

After a hadron-nucleon collision, the forward going particle (or fireball) has a probability of undergoing additional collisions. Collision probability depends upon the target material and particle type. With the hadron-nucleon extension, the model agrees with hadron-nucleon data for nuclei with atomic mass greater than that of Carbon.¹⁰⁰ The model does not consider fission or particle emission of the target nucleus. Two-body decay of hadrons is done exactly, but three-body decays are not considered. The interaction model does not produce kaons, however, if kaons are initially supplied by the user, they are propagated properly.

A.3. NON-CATASTROPHIC PROCESSES

Non-catastrophic processes involve multiple Coulomb scattering, ionization energy loss, and bending in a magnetic field. Coulomb scattering uses a Gaussian probability distribution. Ionization loss is energy dependent and does not involve any fluctuations. Energy fluctuations cause large tails in the ionization energy loss distribution. All three processes are integrated after each target plane (in the calorimeter) or at 5 cm intervals (in the toroids). Decay and interaction probabilities are evaluated at each integration point.

A.4. FLASH CHAMBER DATA

Flash chambers are considered to be infinitely thin (so that no single particle can strike two cells in the same chamber) and have cells 5 mm wide. Shifts and rotations, as determined from analysis of the real flash chambers, are applied. For response, each chamber is divided into 64 regions (along the length of the cell), with each region having its own efficiency and hit cell multiplicity value which also is determined from analysis of the real chambers. The cells "operate" at nominal efficiency along the length of the cell, and at half-nominal efficiency in the readout region. Multiplicity is modeled using a binomial distribution in number of hits, with a spatial distribution flat over about 5 cm (± 5 cells). Noise hits were scattered uniformly across all chambers, with the total number set to agree with values from pedestal runs. (These are runs where the chambers were pulsed out of synchronization with the neutrino beam spill.)

A.5. PROPORTIONAL TUBE DATA

In the calorimeter, the pulse height (energy) per traversal is thrown according to a distribution measured from calibration muons. Difference in gain is accounted for and shows up as variations in HITBIT and latch efficiencies. The AM and FSV latches are derived from the HITBIT's without an additional inefficiency, although software thresholds are variable. SUMOUT latches are generated by adding up the software pulse heights in channels which have the HITBIT latch ON. For toroid planes, the pulse height sum from a pair of channels is thrown according to distributions measured from calibration muons (efficiencies included). The fraction for each channel is set to give exact reconstruction during analysis. No toroid latch bits are generated. No noise is generated for any proportional tube planes.

A.6. COMPARISON WITH CALIBRATION DATA

The Monte Carlo package was compared with the 1982 calibration data. Three of the (nominal) calibration energies are considered: 10, 35 and 100 GeV. Figures A.1, A.2, and A.3 show the measured energy for calibration data and Monte Carlo data. In all cases, the solid line corresponds to calibration data, the broken line to Monte Carlo data. Agreement is good. This is not surprising, since the Monte Carlo package was "tuned" to the calibration data. Energy discrepancy occurs when comparing the hadronic energy for simulated neutrino induced showers. Figure A.4 shows the difference between calculated and selected hadronic energy for simulated neutrino interactions as a function of the selected hadronic energy. There is evidence that the calculated energy is overestimated with increasing selected energy.

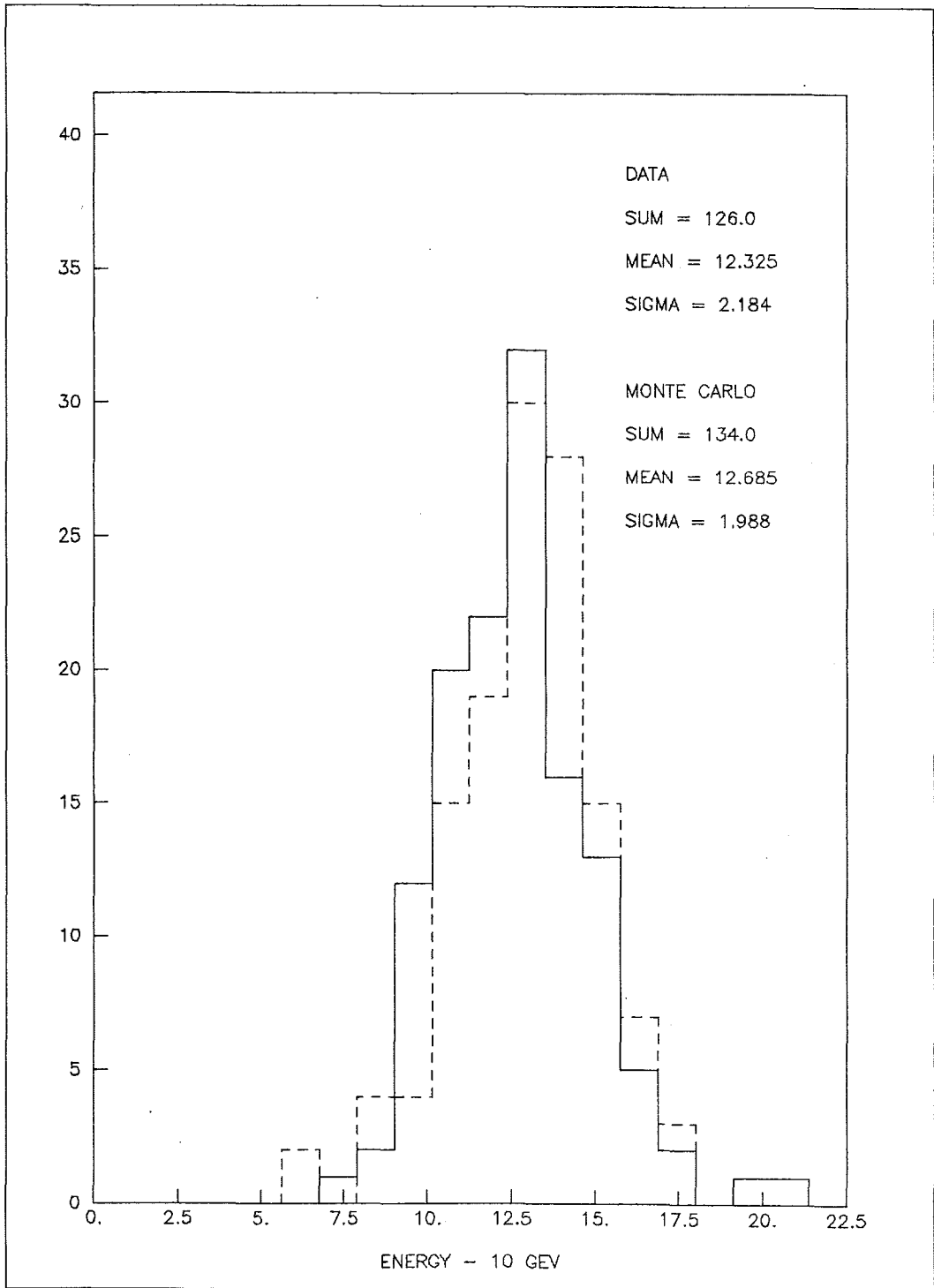


Figure A.1. Energy Comparison - 10 GeV

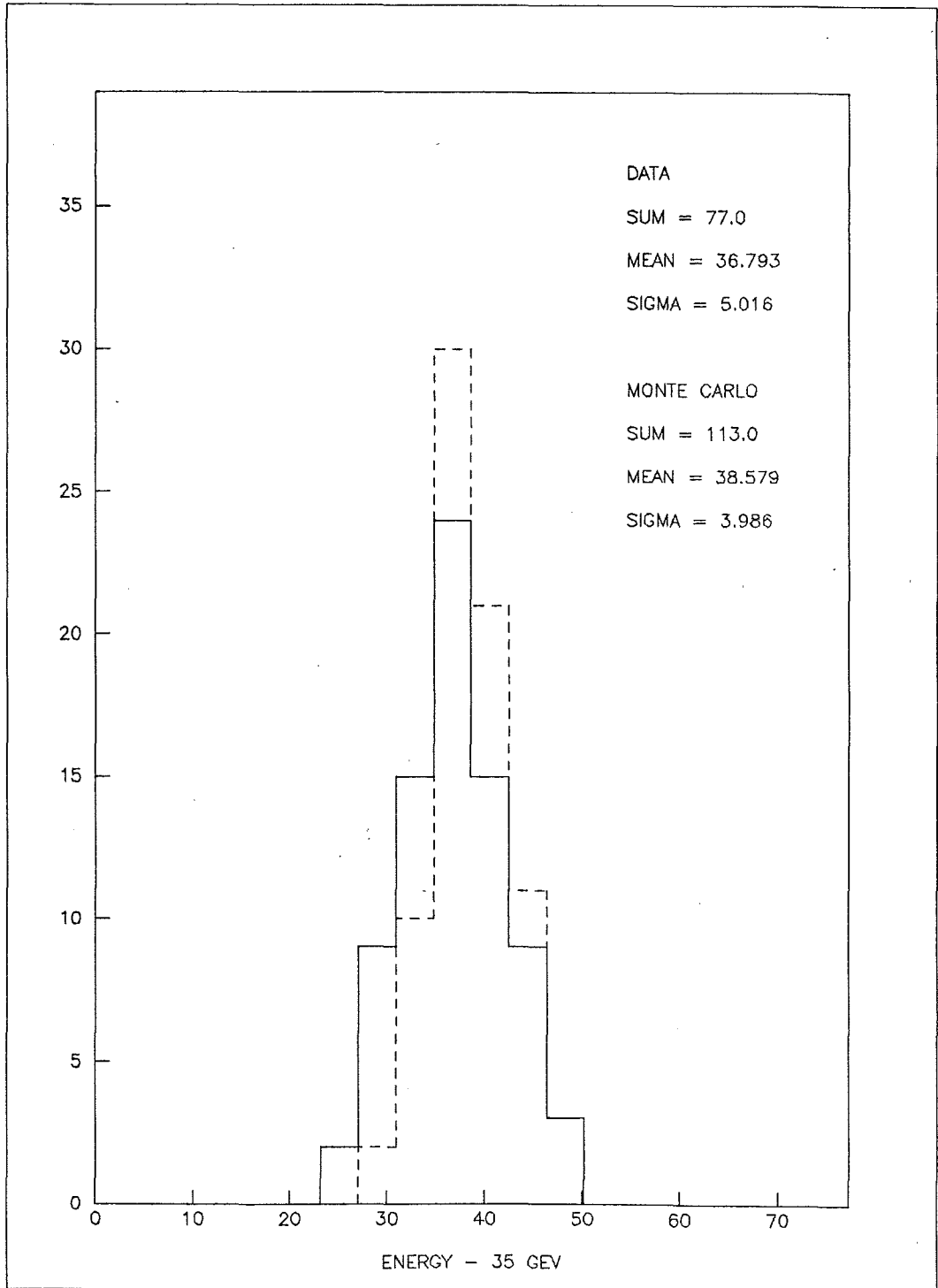


Figure A.2. Energy Comparison - 35 GeV

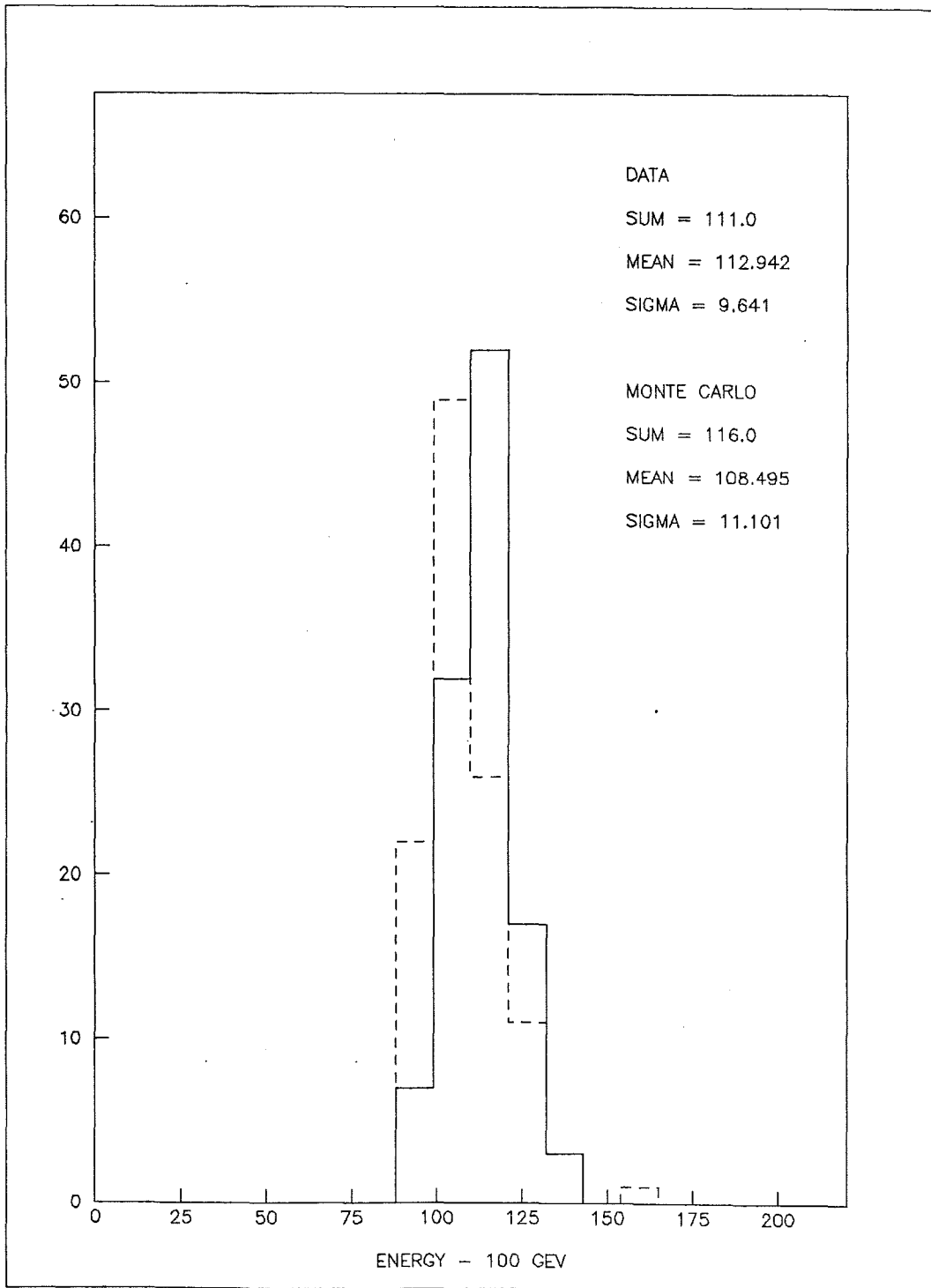


Figure A.3. Energy Comparison = 100 GeV

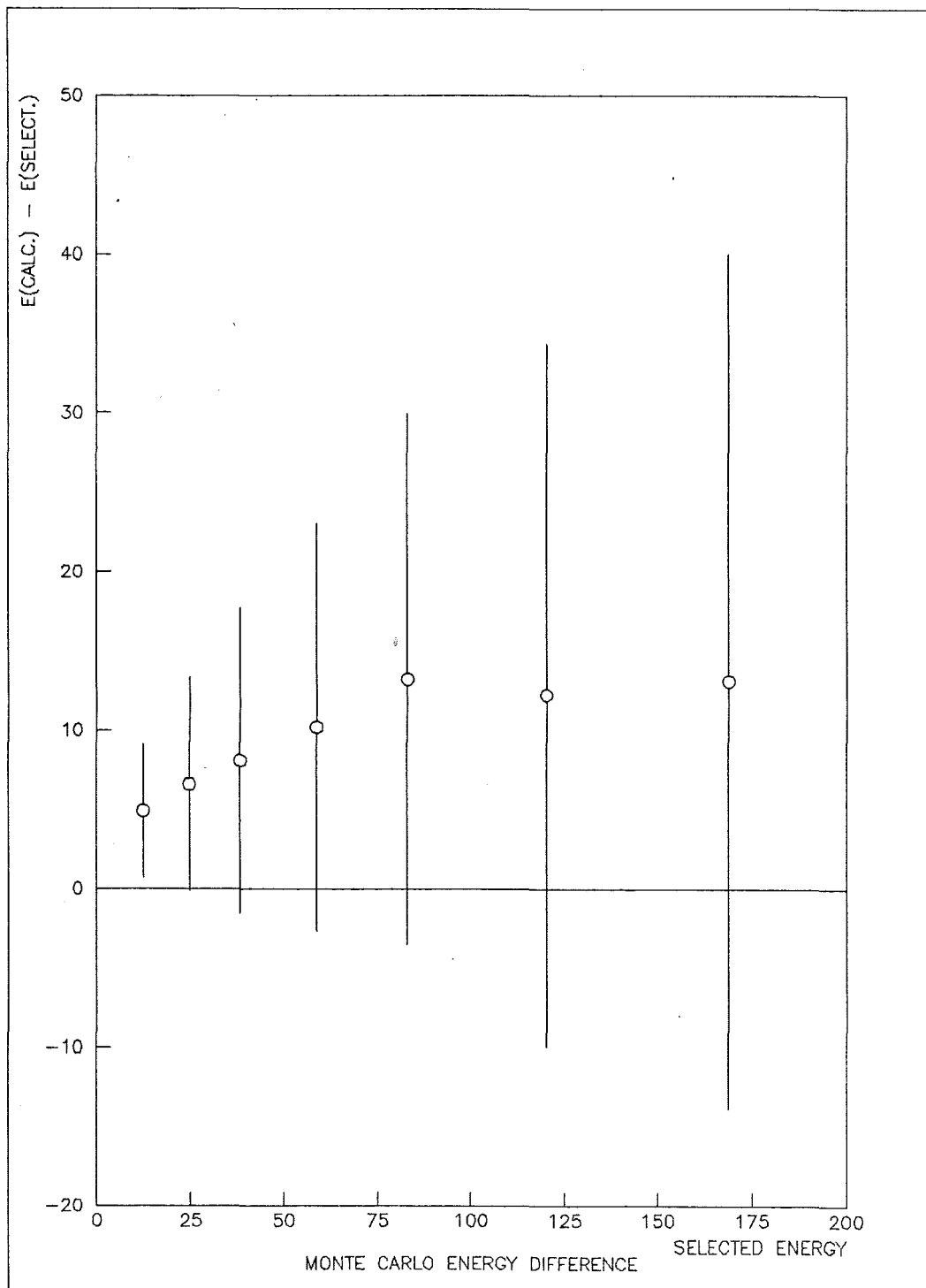


Figure A.4. Monte Carlo Energy Difference

This problem is not well understood, and may be due to the de-excitation model used for the initial fireball. (Calibration simulations use an initial pion, which then interacts.)

Figures A.5, A.6, and A.7 show the density comparisons and Figures A.8, A.9, and A.10 show the shower length comparisons for the three nominal energies. Notice that the Monte Carlo data is denser and shorter. Table A.1 compares the angular profiles of Monte Carlo and calibration data for the nominal energies. For a given shower, the angle (relative to the beam axis) of each hit is calculated and entered into a histogram. All shower hits within 5 meters of the interaction vertex are considered. When all showers, at a given energy, have been analyzed, a Gaussian curve is fitted to the resultant histogram and an rms width is calculated. Table A.1 indicates the values of the rms widths for Monte Carlo and calibration data. Comparing Monte Carlo energy and angle resolutions with calibration data show that the energy resolution is roughly comparable, whereas, angular resolution is slightly degraded.¹⁰¹

In conclusion, the Monte Carlo package can generate electromagnetic and hadronic showers which agree, at the "macroscopic" level, reasonably well with the real data. At the "microscopic" level, some differences exist, as seen by the density, shower length, and angular profile comparisons, as well as the hadronic energy discrepancy in simulated neutrino induced showers.

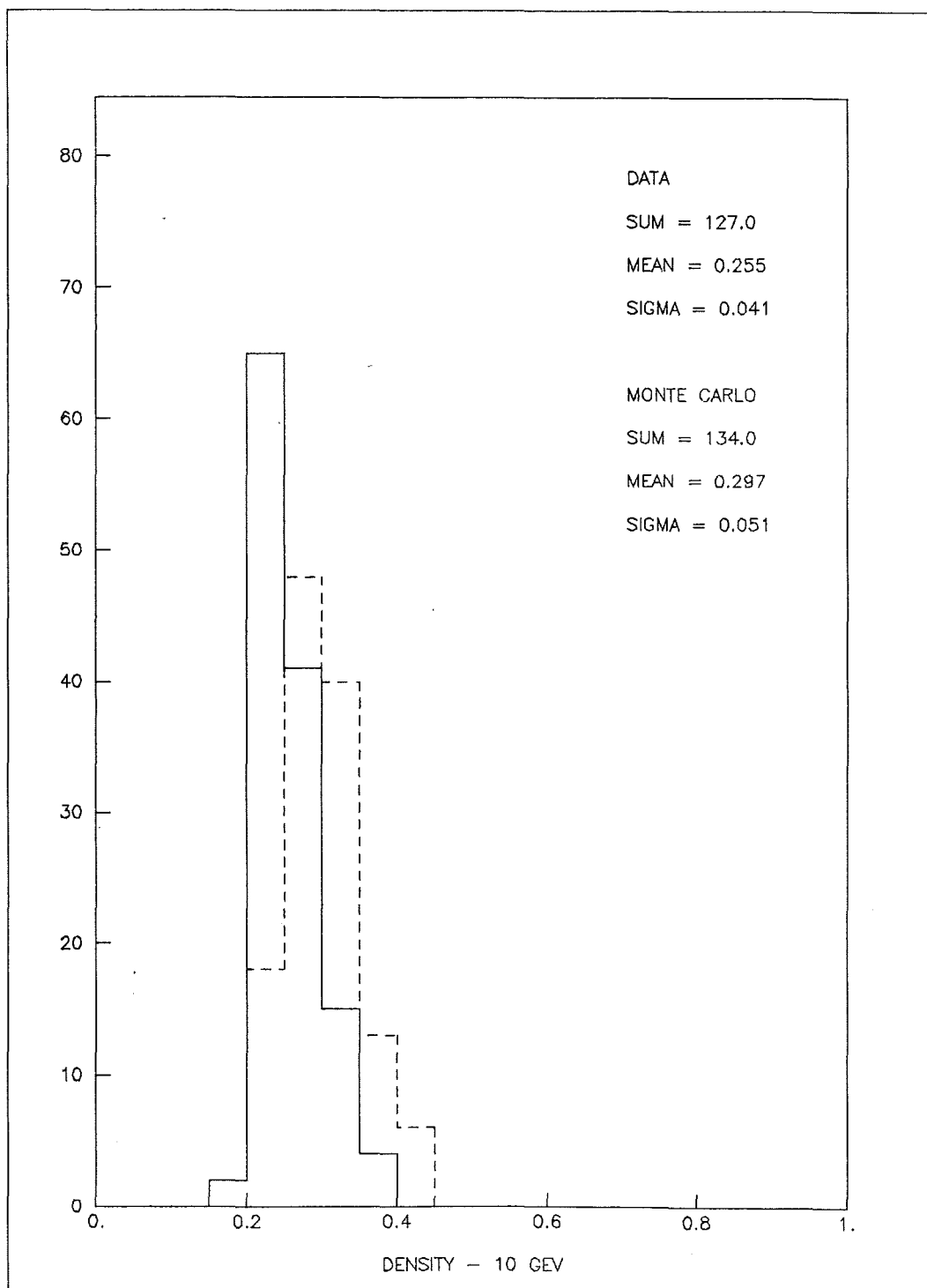


Figure A.5. Density Comparison - 10 GeV

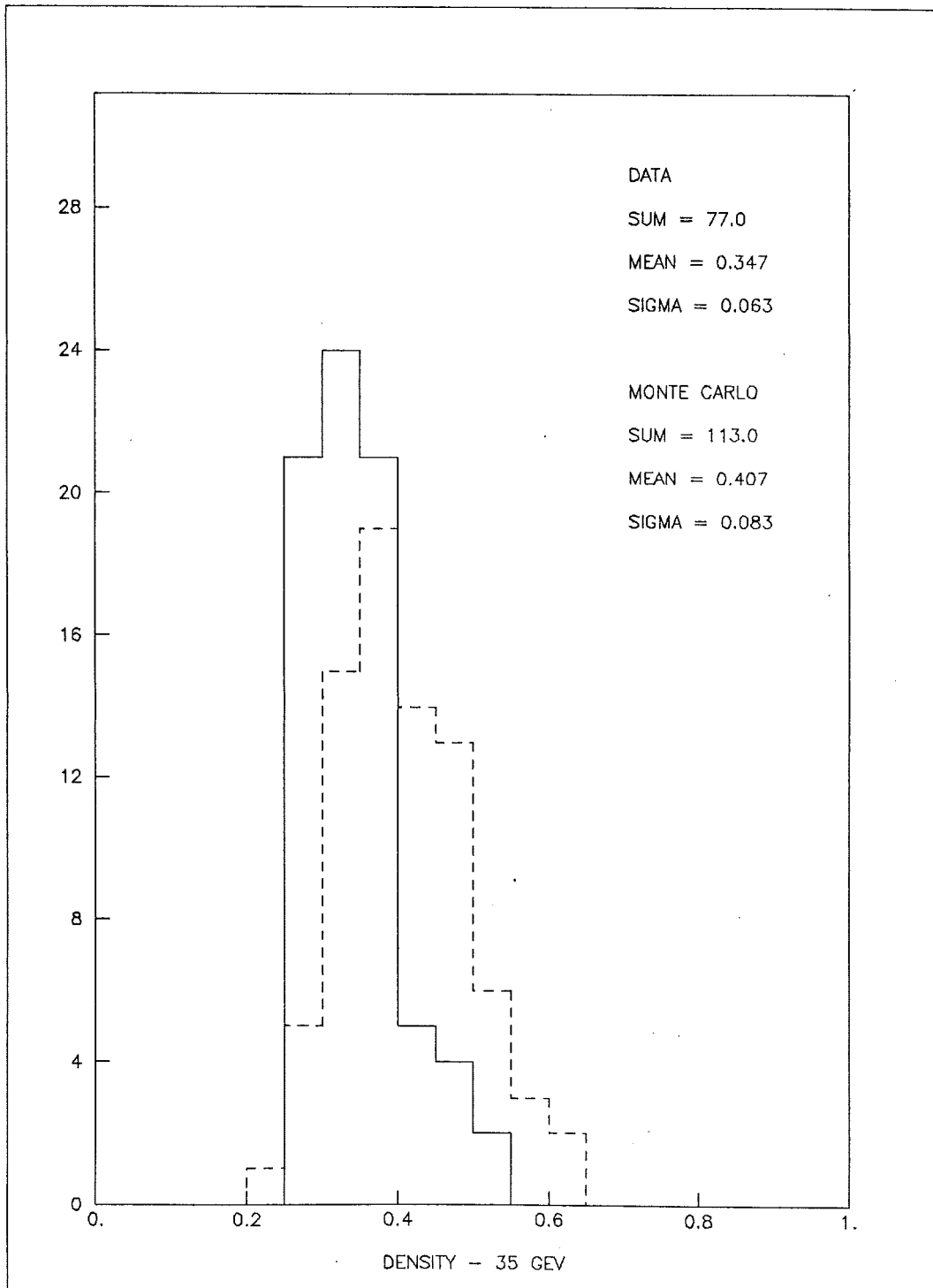


Figure A.6. Density Comparison - 35 GeV

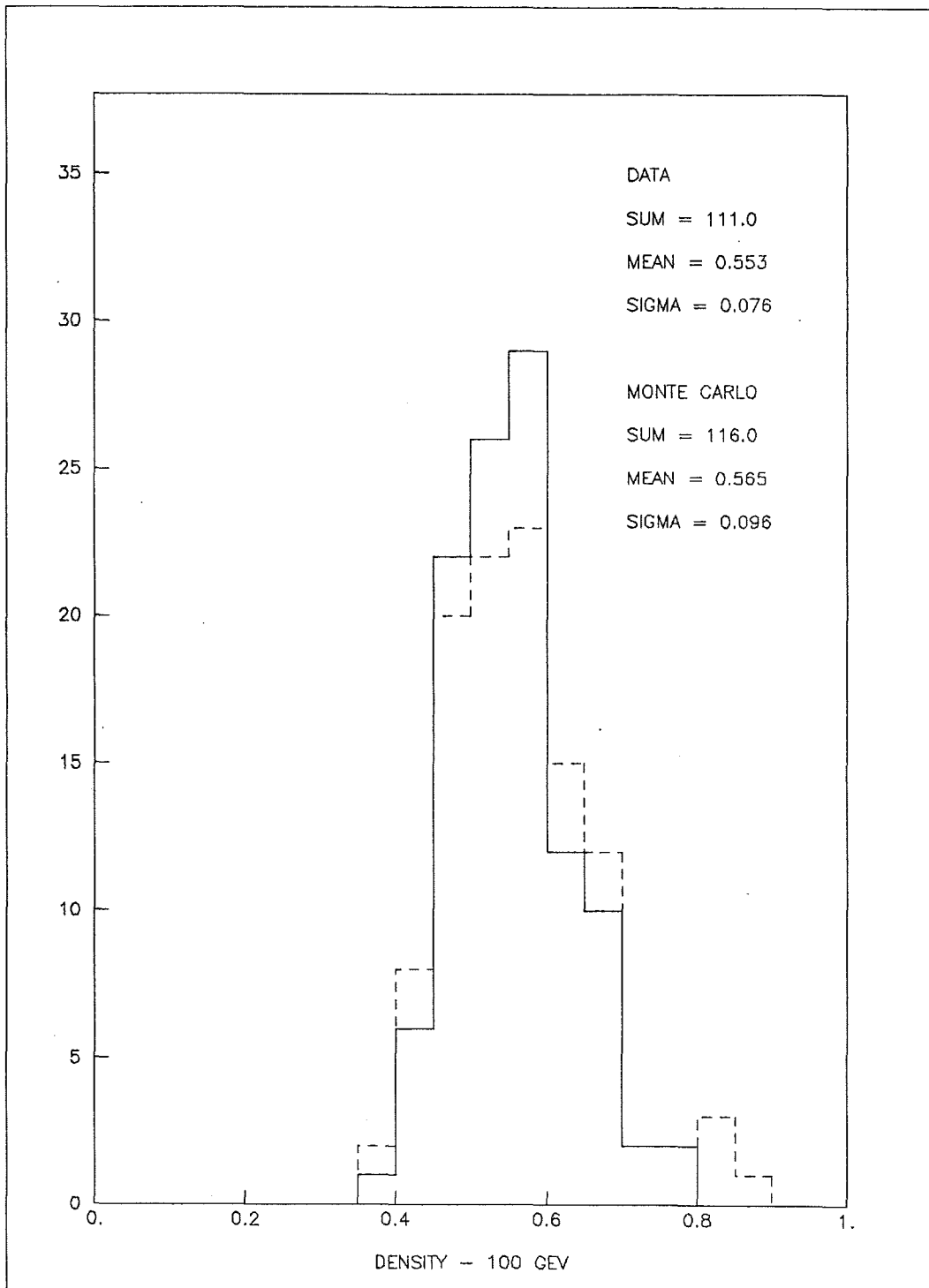


Figure A.7. Density Comparison - 100 GeV

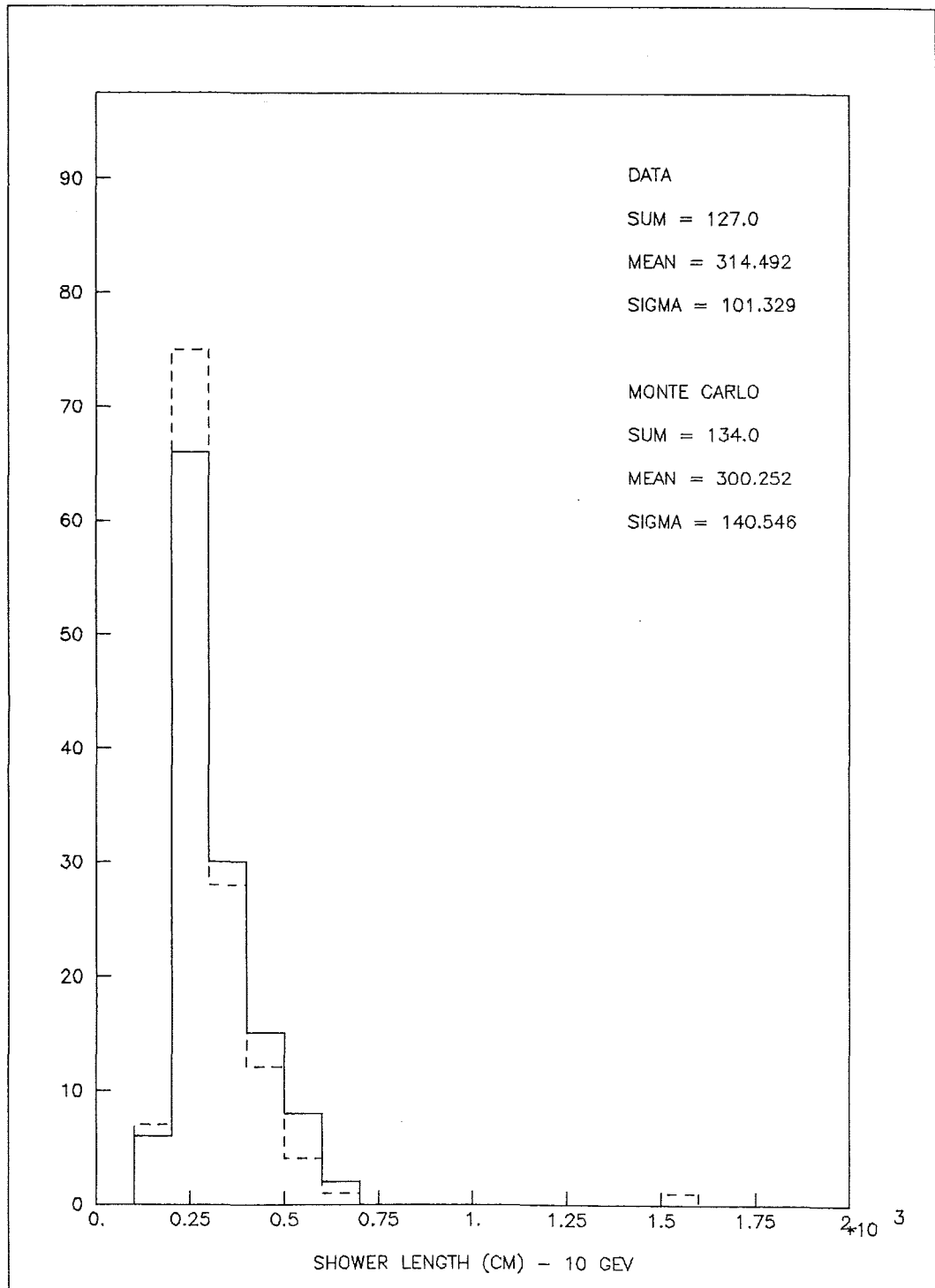


Figure A.8. Shower Length Comparison - 10 GeV

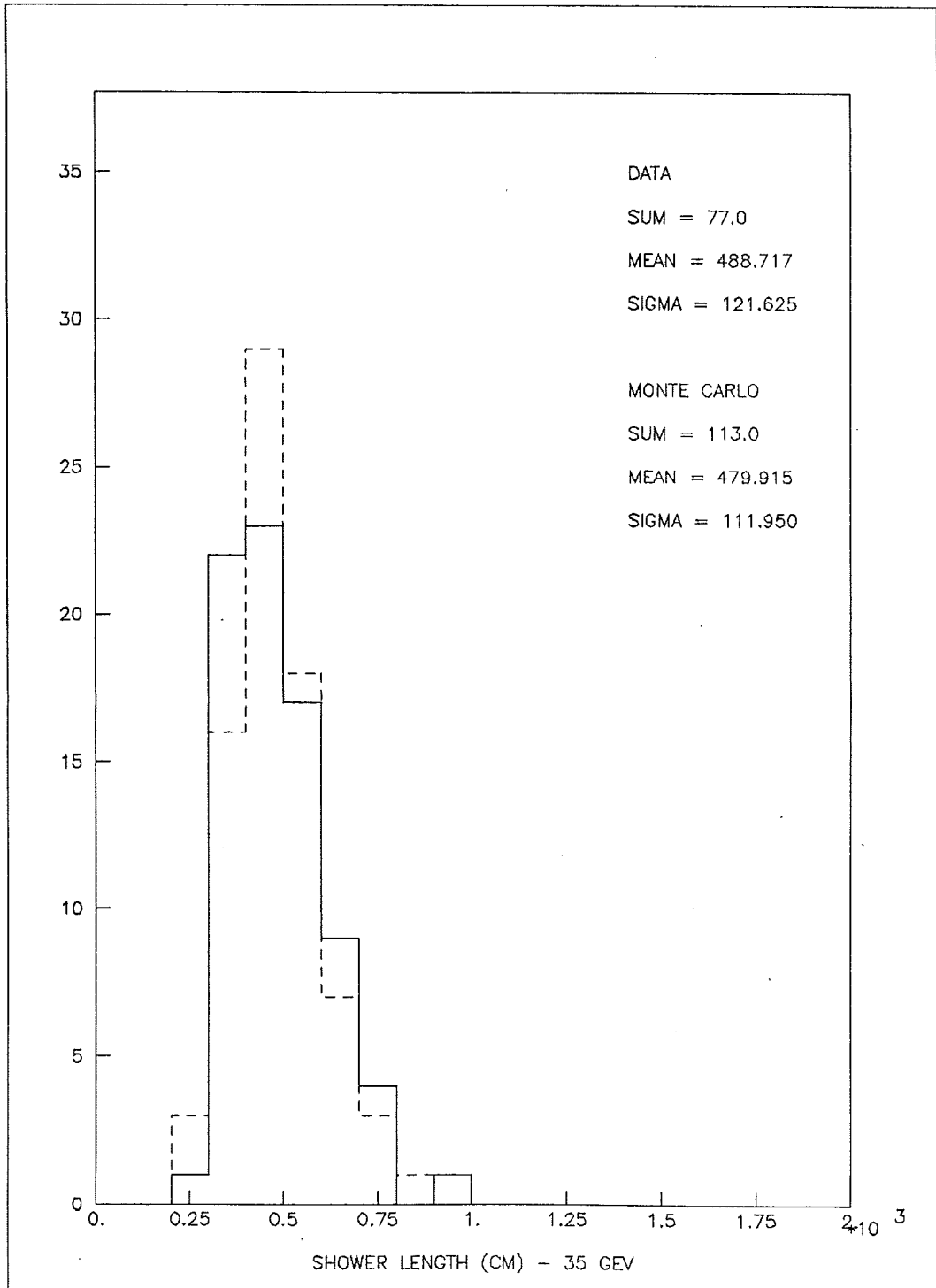


Figure A.9. Shower Length Comparison - 35 GeV

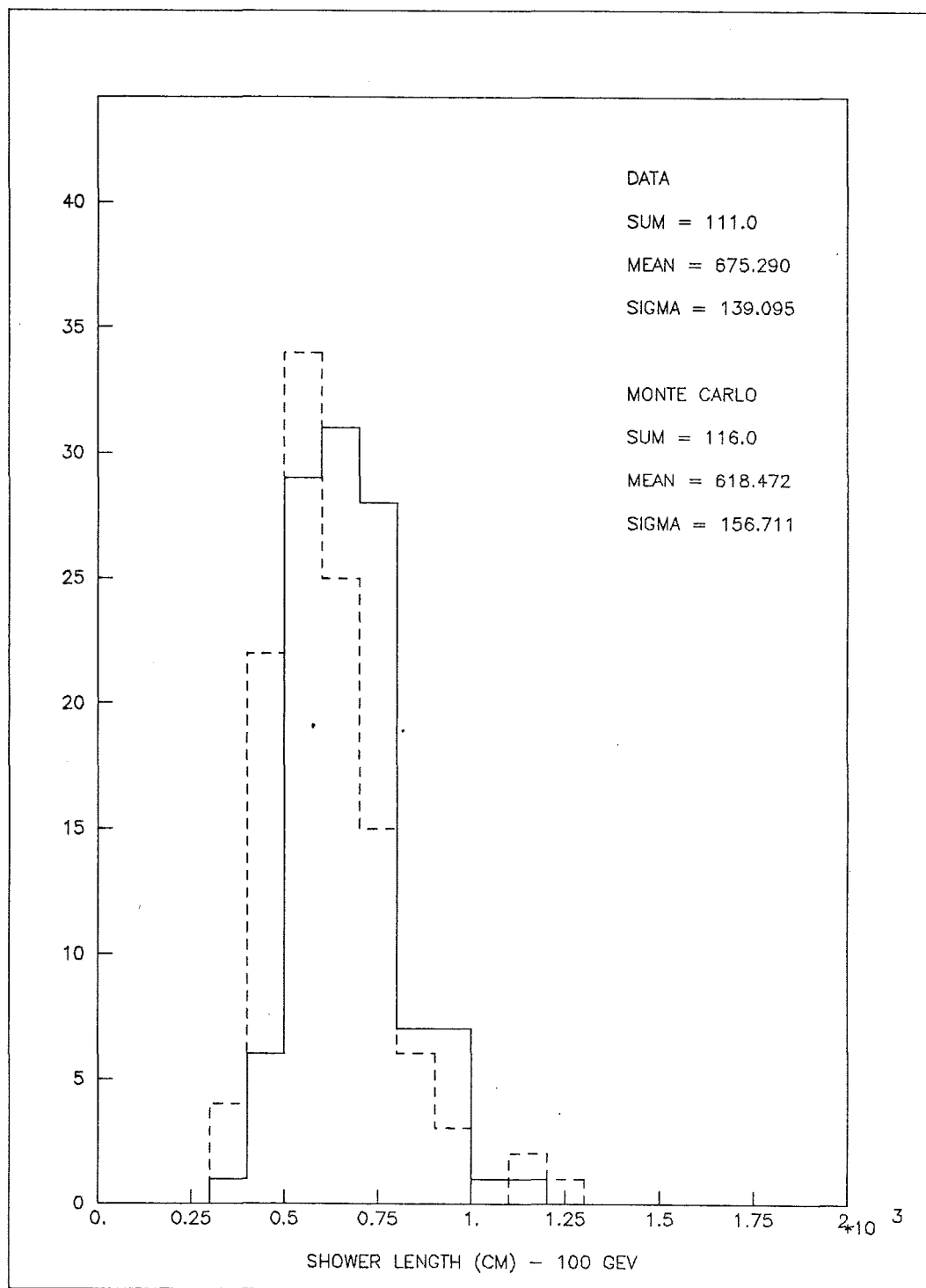


Figure A.10. Shower Length Comparison - 100 GeV

Table A.1. Angular Profile Comparison

ENERGY (GEV)	CALIBRATION	MONTE CARLO
10	0.330	0.311
35	0.240	0.210
100	0.200	0.173

APPENDIX B

DERIVATION OF $E\theta^2$

We wish to present a brief derivation of the quantity $E\theta^2$ from basic kinematical identities. Remember that the value of Q^2 , defined at the lepton vertex is:

$$Q^2 = 2E_{\ell}E_{\ell'}(1 - \cos \theta_{\ell\ell'}).$$

For small angles, it is possible to expand the quantity $\cos \theta$ as a Taylor series:

$$\cos \theta \approx 1 - \frac{\theta^2}{2!} + \frac{\theta^4}{4!} - \dots.$$

Keeping terms up to and including θ^2 , and inserting into the expression for Q^2 , we obtain:

$$\begin{aligned} Q^2 &\approx E_{\ell}E_{\ell'}\theta_{\ell\ell'}^2, \\ &\approx \frac{E_{\ell}}{E_{\ell'}}(E_{\ell'}\theta_{\ell\ell'})^2. \end{aligned}$$

The transverse momentum, P_T , of the outgoing lepton is just $P_{\ell} \sin \theta_{\ell\ell'}$, which in the limit of small scattering angles and negligible lepton mass is:

$$\begin{aligned} P_T' &= P_{\ell'} \sin \theta_{\ell\ell'}, \\ &\approx P_{\ell'}\theta_{\ell\ell'} \approx E_{\ell'}\theta_{\ell\ell'}. \end{aligned}$$

This gives an expression for Q^2 of:

$$Q^2 \approx \frac{E_{\ell}}{E_{\ell'}}(E_{\ell'}\theta_{\ell\ell'})^2 \approx \frac{E_{\ell}}{E_{\ell'}}P_T'^2.$$

Also recall that:

$$Q^2 = 2m\nu \approx 2mxE_h,$$

and that:

$$y = 1 - \frac{E_{\ell'}}{E_{\ell}},$$

so by substitution, we obtain:

$$\begin{aligned} Q^2 &\approx \frac{E_{\ell'}}{E_{\ell}} P_T'^2 \approx \frac{P_T'^2}{1-y}, \\ &\approx 2mx E_h. \end{aligned}$$

Equating these two expressions for Q^2 , we obtain:

$$2mx E_h \approx \frac{P_T'^2}{1-y}.$$

Since transverse momentum is balanced:

$$P_T = P_{\ell'} \sin \theta_{\ell\ell'} = P_h \sin \theta_h,$$

and can be written (in the small angle approximation) as:

$$P_{\ell'} \theta_{\ell\ell'} \approx P_h \theta_h = P_T.$$

which yields (after substitution):

$$2mx E_h \approx \frac{(P_h \theta_h)^2}{1-y}.$$

Rewriting, we obtain:

$$P_h^2 \theta_h^2 \approx 2m E_h x (1-y).$$

The relativistic kinematical relationship between a particle's energy, momentum and mass is (setting $c=1$):

$$E^2 = P^2 + m^2.$$

For the hadron system:

$$E_h^2 = P_h^2 + W^2,$$

where W^2 is the square of the invariant mass. This equation can be written as:

$$\begin{aligned} P_h^2 &= E_h^2 - W^2 \\ &= E_h^2 \left(1 - \frac{W^2}{E_h^2}\right). \end{aligned}$$

Given this relationship, we can write:

$$P_h^2 \theta_h^2 = E_h^2 \theta_h^2 \left(1 - \frac{W^2}{E_h^2}\right) \approx 2mE_h x(1-y).$$

Solving this equation for the quantity $E_h \theta_h^2$, we obtain:

$$E_h \theta_h^2 \approx \frac{2mx(1-y)}{1 - (W^2/E_h^2)} \approx 2mx(1-y).$$

Where the quantity W^2/E_h^2 is assumed to be small. Table B.1 lists the value of W^2/E_h^2 for various values of E_h and x . Only for low E_h and/or low x is W^2/E_h^2 greater than 5-10%. Thus, with the given approximations, we can write $E_h \theta_h^2$ as:

$$E_h \theta_h^2 \approx 2mx(1-y).$$

Table B.1. Magnitude of $(W/E_h)^2$

E_h (GeV)	X=0.1	X=0.3	X=0.5	X=0.7
10.0	0.18	0.14	0.10	0.06
20.0	0.09	0.07	0.05	0.03
30.0	0.06	0.05	0.03	0.02
50.0	0.04	0.03	0.02	0.01
70.0	0.03	0.02	0.01	0.01

LIST OF REFERENCES

LIST OF REFERENCES

1. F. Reines and C. Cowan, Phys. Rev. 113, 273 (1959).
2. E. Fermi, Z. Physik 88, 161 (1934).
3. C. S. Wu et al., Phys. Rev. 105, 1413 (1957).
4. M. L. Goldhaber et al., Phys. Rev. 109, 1015 (1958).
5. H. Anderson et al., Phys. Rev. 119, 2050 (1960).
6. G. Danby et al., Phys. Rev. Lett. 9, 36 (1962).
7. F. J. Hasert et al., Phys. Lett. 46B, 121 (1973).
8. S. Weinberg, Phys. Rev. Lett. 19, 1264 (1967).
9. A. Salam, "Elementary Particle Theory", Proceedings of the 8th Nobel Symposium, edited by N. Svartholm (Almqvist and Wiksel, Stockholm, 1968).
10. S. L. Glashow, J. Iliopoulos and L. Maiani, Phys. Rev. D 2, 1285 (1970).
11. J. E. Kim et al., Rev. Mod. Phys. 53, 211 (1981).
12. UA1: G. Arnison et al., Phys. Lett. 122B, 103 (1983); 129B, 273 (1983); 134B, 469 (1984).
UA2: M. Banner et al., Phys. Lett. 122B, 476 (1983).
13. UA1: G. Arnison et al., Phys. Lett. 126B, 398 (1983).
UA2: M. Banner et al., Phys. Lett. 129B, 130 (1983).
14. CERN Courier 24 (4), 139 (1984).
15. F. J. Hasert et al., Phys. Lett. 46B, 138 (1973).
16. Ibid., Phys. Lett. 46B, 121 (1973).
17. Ibid., Phys. Lett. 46B, 138 (1973); 84B, 281 (1979).
18. A. Benvenuti et al., Phys. Rev. Lett. 32, 800 (1974).
19. Ibid., Phys. Rev. Lett. 30, 1084 (1973); 32, 125 (1974); 33, 984 (1974).

20. Ibid., Phys. Rev. Lett. 33, 984 (1974).
21. Ibid., Phys. Rev. Lett. 34, 419 (1975); 34, 597 (1975); 35, 1199 (1975); 35, 1203 (1975); 36, 1478 (1976).
22. Ibid., Phys. Rev. Lett. 38, 1110 (1977); 40, 488 (1978).
23. Ibid., Phys. Rev. Lett. 42, 149 (1979); 42, 1317 (1975).
24. Ibid., Phys. Rev. Lett. 41, 725 (1978).
25. B. C. Barish et al., Phys. Rev. Lett. 35, 1316 (1977); 39, 1595 (1977).
26. F. S. Merritt et al., Phys. Rev. D 17, 2199 (1978).
27. B. C. Barish et al., Phys. Rev. Lett. 39, 741 (1977); 40, 1414 (1978).
28. R. E. Blair, Ph. D. Thesis, California Institute of Technology (1982).
29. B. Barish et al., Proceedings of the Summer Institute on Particle Physics, Stanford University, edited by Anne Mosher (Stanford, 1981).
30. R. Blair et al., "Recent Results from CFRR Experiments at Fermilab", contributed to Neutrino 81 International Conference on ν Physics and Astronomy, Wailea (1981).
31. R. Blair et al., Phys. Rev. Lett. 51, 343 (1983).
32. C. Baltay et al., Phys. Rev. Lett. 44, 916 (1980).
33. Ibid., Phys. Rev. Lett. 52, 1948 (1984).
34. H. Abramowicz et al., Z. Phys. C - Particles and Fields 12, 289 (1982); 17, 199 (1983); 17, 283 (1983); J. G. H. deGroot et al., ibid. 1, 143 (1979); Phys. Lett. 82B, 456 (1979).
35. M. Holder et al., Phys. Lett. 71B, 222 (1977); 72B, 254 (1977).
36. M. Holder et al., Phys. Lett. 69B, 377 (1977); 70B, 377 (1977); J. G. H. deGroot et al., ibid. 86B, 103 (1979).
37. M. Jonker et al., Phys. Lett. 86B, 229 (1979).
38. Ibid., Phys. Lett. 99B, 265 (1981); 102B, 67 (1981); 109B, 133 (1982); 123B, 269 (1983).
39. Ibid., Phys. Lett. 128B, 117 (1983).
40. W. Panofsky, Proceedings of International Symposium on High Energy Physics, Vienna (1968).

41. J. D. Bjorken, Proceedings of the 3rd International Symposium of Electron and Photon Interactions, Stanford University (Stanford, 1967).
42. R. P. Feynman, *Phys. Rev. Lett.* 23, 1415 (1969).
43. J. D. Bjorken and E. A. Paschos, *Phys. Rev.* 185, 1975 (1969).
44. J. D. Bjorken and S. D. Drell, Relativistic Quantum Mechanics (McGraw-Hill, New York, 1964); Relativistic Quantum Fields (McGraw-Hill, New York, 1965).
45. C. Callen and D. Gross, *Phys. Rev. Lett.* 22, 156 (1969).
46. M. Gell-Mann, *Phys. Lett.* 8, 214 (1964).
47. G. Zweig, CERN Report Number 8182/Th401, 1964 (unpublished).
48. D. J. Gross and C. H. Llewellyn-Smith, *Nucl. Phys. B* 14, 337 (1969).
49. S. L. Adler, *Phys. Rev.* 143, 1144 (1966).
50. R. Feynman and M. Gell-Mann, *Phys. Rev.* 109, 193 (1958).
51. S. Weinberg, *Phys. Rev. Lett.* 19, 1264 (1967).
52. A. Salam, "Elementary Particle Physics", Proceedings of the 8th Nobel Symposium, edited by N. Svartholm (Almqvist and Wiksel, Stockholm, 1968).
53. G. t'Hooft, *Nucl. Phys. B* 33, 173 (1971); 35, 167 (1971).
54. R. Brout and F. Englert, *Phys. Rev. Lett.* 13, 321 (1964); G. Guralnik et al., *ibid.* 13, 585 (1964); P. W. Higgs, *Phys. Lett.* 12, 232 (1964); *Phys. Rev. Lett.* 13, 508 (1964).
55. A. Benvenuti et al., Proceedings of the International Neutrino Conference, Aachen (Braunschweig, 1976); F. J. Hasert et al., *Phys. Lett.* 46B, 138 (1973).
56. UA1: G. Arnison et al., *Phys Lett.* 122B, 103 (1983); 129B, 273 (1983); 134B, 469 (1984).
UA2: M. Banner et al., *Phys. Lett.* 122B, 476 (1983).
57. UA1: G. Arnison et al., *Phys. Lett.* 126B, 398 (1983).
UA2: M. Banner et al., *ibid.* 129B, 130 (1983).
58. J. Goldstone, *Nuovo Cimento* 19, 154 (1961).
59. N. Cabibbo, *Phys. Rev. Lett.* 10, 531 (1963).
60. S. L. Glashow, J. Iliopoulos and L. Maiani, *Phys. Rev. D* 2, 1285 (1970).

61. C. Baltay, Proceedings of the XIX International Conference on High Energy Physics, Tokyo (Japan, 1978).
62. F. E. Taylor et al., IEEE Trans. Nucl. Sci. NS-25, 312 (1978).
63. J. Ernwein, E594 Internal Memo 81-15.
64. Designed by John Mark, Stanford Linear Accelerator Center. Blueprint numbers: SA-410-045-50-R1-E, SA-410-045-25-R0-E, GP-410-045-01-R6-E, and SA-410-045-01-R0-E.
65. M-D Pneumatics Inc., 4840 West Kearney Street, Springfield, MO 65803.
66. R. A. Smythe et al., Nucl. Instrum. and Methods 193, 457 (1982).
67. Gow-Mac Instrument Co., P. O. Box 32, Bound Brook, NJ 08805.
68. D. L. Edmunds et al., Nucl. Instrum. and Methods 192, 325 (1982).
69. J. F. Bartlett et al., IEEE Trans. Nucl. Sci. NS-26, 4427 (1979).
70. Micheal A. Tartaglia, Ph. D. Thesis, Massachusetts Institute of Technology, 1984.
71. R. Pitt (private communication).
72. A. Malensek, "N-5 Hadron Calibration Beam to Lab C", Fermilab Report Number FNAL-TM-717, 1977.
73. M. A. Tartaglia, Ph. D. Thesis, Massachusetts Institute of Technology, 1984.
74. F. E. Taylor, "The E594 Calibration Data, Pass I", E594 Internal Memo.
75. C. W. Fabjan et al., Nucl. Instrum. and Methods 141, 61 (1977).
76. F. Nezirick, Fermilab Report Number FNAL-TM-555, 1973; S. Mori, "Wide Band Single Horn System", Fermilab Report Number FNAL-TM-663, 1976; "Wide Band Single Horn System II", Fermilab Report Number FNAL-TM-720, 1977; J. Grimson and S. Mori, "New Single Horn System", Fermilab Report Number FNAL-TM-824, 1978.
77. C. R. Kerns, "Radiation Hardened Proton Meter for Fermilab External Beam Lines", Fermilab Report Number FNAL-TM-551, 1975.
78. R. Brock (private communication).
79. M. A. Tartaglia, Ph. D. Thesis, Massachusetts Institute of Technology, 1984.
80. C. L. Wang, Phys. Rev. D 7, 2609 (1973); 10, 3846 (1974).

81. R. Stefanski and H. White, Fermilab Report Number FNAL-FN-292, 1976.
82. S. Mori, "Relative Neutrino and Antineutrino Event Rates of the Single Horn System", Fermilab Report Number FNAL-TM-837, 1978.
83. Atherton et al., "Precise Measurements of Particle Production by 400 GeV Protons on Beryllium", CERN Report Number CERN-80-07, 1980.
84. A. Malensek, "Empirical Formula for Thick Target Particle Production", Fermilab Report Number FNAL-FN-341, 1981.
85. A. J. Cohen (private communication).
86. ABCLOS: P. C. Bosetti et al., Nucl. Phys. B 142, 1 (1978).
CDHS: J. G. H. deGroot et al., Z. Phys. C - Particles and Fields 1, 143 (1979); Phys. Lett. 82B, 456 (1979).
CHARM: F. Bergsma et al., Phys. Lett. 123B, 269 (1983).
HPWFRO: A. Benvenuti et al., Phys. Rev. Lett. 42, 1317 (1979).
87. CDHS: J. G. H. deGroot et al., Z. Phys. C - Particles and Fields 1, 143 (1979).
CHARM: M. Jonker et al., Phys. Lett. 128B, 117 (1983).
E594: G. P. Yeh, Ph. D. Thesis, Massachusetts Institute of Technology, 1984.
88. M. A. Tartaglia, Ph. D. Thesis, Massachusetts Institute of Technology, 1984.
89. M. Goodman, E594 Internal Memo 84-6.
90. Atherton et al., "Precise Measurements of Particle Production by 400 GeV Protons on Beryllium", CERN Report Number CERN-80-07, 1980.; A. Malensek, "Empirical Formula for Thick Target Particle Production", Fermilab Report Number FNAL-FN-341, 1981.
91. A. J. Buras, Nucl. Phys. B 125, 125 (1977); A. J. Buras and K. J. F. Gaemers, Nucl. Phys. B 132, 249 (1977).
92. R. D. Field and R. P. Feynman, Phys. Rev D 15, 2590 (1977).
93. F. Bergsma et al., Phys. Lett. 123B, 269 (1983).
94. F. James and M. Roos, CERN Computer 7600 Interim Program Library, D506/D516, 1971.
95. G. P. Yeh, Ph. D. Thesis, Massachusetts Institute of Technology, 1984.

96. CDHS: M. Holder et al., Phys. Lett. 71B, 222 (1977); 72B, 254 (1977).
CITFR: F. S. Merritt et al., Phys. Rev. D 17, 2199 (1978).
CFRR: B. Barish et al., Proceedings of the Summer Institute on Particle Physics, Stanford University, edited by Anne Mosher (Stanford, 1981).
CHARM: M. Jonker et al., Phys. Lett. 99B, 265 (1981); 102B, 67 (1981).
E594: G. P. Yeh, Ph. D. Thesis, Massachusetts Institute of Technology, 1984.
97. G. P. Yeh (private communication).
98. Martin L. Perl, High Energy Hadron Physics (Wiley, New York, 1979).
99. L. S. Osborne, Phys. Lett. 63B, 456 (1976).
100. J. E. Elias et al., Phys. Rev. D 22, 13 (1980).
101. A. Mukherjee, E594 Internal Memo 84-7.